Energy of the Quasi-free Electron in Atomic and Molecular Fluids

by

Xianbo Shi

A dissertation submitted to the Graduate Faculty in Chemistry
in partial fulfillment of the requirements
for the degree of Doctor of Philosophy,
The City University of New York.

2010

This manuscript has been read and accepted for the
Graduate Faculty in Chemistry in satisfaction of the
dissertation requirements for the degree of Doctor of Philosophy.

Date	Dr. Cherice M. Evans, Chair of Examining Committee
Date	Dr. Mahesh K. Lakshman, Executive Officer

Dr. Gary L. Findley

Dr. Seogjoo Jang

Dr. Lawrence W. Johnson
Supervisory Committee

THE CITY UNIVERSITY OF NEW YORK

Abstract

Energy of the Quasi-free Electron in
Atomic and Molecular Fluids

by

Xianbo Shi

Advisor: Dr. Cherice M. Evans

The ability to predict accurately the density dependent evolution of the conduction band energy of insulators has applications in the optimization of solvent choice and thermodynamic conditions for chemical reactions. However, directly investigating density dependent changes in the conduction band is experimentally difficult. Therefore, we have used field ionization of high-n dopant Rydberg states to determine the perturber induced shift of the dopant ionization energy $\Delta(\rho_{\text{P}})$, where ρ_{P} is the perturber number density. Appropriate modeling allows the minimum of the conduction band energy $V_0(\rho_{\text{P}})$ to be extracted from $\Delta(\rho_{\text{P}})$. Field ionization requires the measurement of photoionization spectra of a dopant at two different electric field strengths. Thus, in this study, photoionization spectra of various dopants (i.e., CH_3I, C_2H_5I, N,N-dimethylanaline, trimethylamine and triethylamine) were obtained under different electric field strengths in atomic (i.e., Ar, Kr, and Xe) and molecular (i.e., CH_4 and C_2H_6) perturbers from low density to the density of the triple point liquid, at non-critical temperatures and on an isotherm near the perturber critical isotherm.

At low perturber number density, a temperature dependence was observed in $\Delta(\rho_{\mathrm{P}})$, with $|\Delta(\rho_{\mathrm{P}})|$ increasing as the temperature decreases. This observation contradicts the prediction of the Fermi-Alekseev-Sobel'man model. Within the local Wigner-Seitz model developed by our group, the temperature behavior at low density arises from the ensemble average ion/perturber polarization energy $P_{+}(\rho_{\mathrm{P}})$ and is caused by variations in the dopant/perturber radial distribution function. Moreover, a striking critical point effect in $V_0(\rho_{\mathrm{P}})$ was observed in all of the perturbers investigated. This critical point effect is explained by the dramatic increase in the local density around a perturber particle near the critical point of the perturber. This local density increase, caused by an increase in the correlation length of the perturber, acts to confine the quasi-free electron, thereby increasing its kinetic energy. Various intermolecular potentials and integral methods necessary to calculate the radial distribution functions were studied and tested in order to achieve the best fit to the experimental $\Delta(\rho_{\mathrm{P}})$ in molecular perturbers.

Acknowledgments

I would first like to thank Dr. Cherice M. Evans, my Major Professor, for her supervision, guidance and support throughout this work. I am also indebted to Dr. Gary L. Findley for his advisement, many valuable suggestions and expertise. Special thanks to both Dr. Evans and Dr. Findley for revising this dissertation and other papers. I wish to express my appreciation to Ms. Luxi Li and Ms. Gina M. Moriarty for their help on the experimental work. I also want to thank Dr. Seogjoo Jang and Dr. Lawrence W. Johnson for many helpful discussions and for serving on my dissertation committee. Finally, I would like to thank the staff of the University of Wisconsin Synchrotron Radiation Center for their many kindnesses. We would especially like to thank Ms. Mary Severson, Dr. Mark Bisson, and Dr. Bob Julian for maintaining the Al-Seya beamline that was used in this work. We would also like to thank Mr. Troy Humphrey for helping us repair some of the electronic equipment needed for our investigations.

All of the measurements presented here were performed at the University of Wisconsin Synchrotron Radiation Center (NSF DMR-0537588) in Stoughton, WI. This work was supported by grants to Dr. Cherice M. Evans from the Petroleum Research Fund (41378-G6) and the Professional Staff Congress of the City University of New York (PSC 60074-34 35, PSCREG-36-233, PSCREG-37-593, PSCREG-38-146,

PSCREG-39-249), as well as by grants to Dr. Gary L. Findley from the Petroleum Research Fund (45728-B6) and the Louisiana Board of Regents (LEQSF(2006-09)-RD-A33). Special thanks are also extended to the Graduate Center of the City University of New York for providing numerous travel grants and small research grants to support this work. Finally, I would like to thank the Queens College Department of Chemistry and Biochemistry for their support throughout the duration of this project.

Contents

List of Tables

List of Figures

Chapter 1

Introduction

The electronic properties of atomic and molecular fluids have been extensively studied both experimentally and theoretically. The evolution of these properties with fluid density and temperature is important in investigating solute/solvent (i.e., dopant/ perturber) interactions and electron/solvent interactions in uncorrelated and highly correlated systems. Another motivation of this work is to improve the understanding of these interactions in supercritical fluids near the critical point, since supercritical fluids have become increasingly important in environmental and industrial chemistry applications. Supercritical fluids are widely used to improve rates and modify product ratios of chemical reactions [1], to vary chemical shifts in NMR [1, 2], and to alter lifetimes and energies of molecular vibrational and electronic states [2].

Due to their large orbital nature, Rydberg states are extremely sensitive to the environment (where enviroment implies an external electric or magnetic field, or perturber atoms or molecules) and, therefore, make an excellent probe for our studies [3–8]. In this dissertation, we use field ionization of high-n dopant Rydberg states to investigate the perturber induced shift of the dopant ionization energy $\Delta(\rho_{\rm P})$, where $\rho_{\rm P}$ is the perturber number density. Once $\Delta(\rho_{\rm P})$ is obtained, the energy of the quasi-free electron $V_0(\rho_{\rm P})$, or the minimum of the conduction band energy of

the perturber medium, can be extracted with appropriate modeling. This quantity is related to the electron mobility in a solvent [9–12] and is therefore often used to study the effects of perturber parameters (e.g., molecular shape, interaction strength, etc.) on electron mobility. Electron mobility, in turn, can influence the kinetics of chemical reactions, especially electrochemical reactions [13, 14]. Thus, the ability to model $V_0(\rho_P)$ accurately has applications in the optimization of the choice of solvents and thermodynamic conditions for chemical reactions.

In Chapter 2 a review of theoretical and experimental approaches to $\Delta(\rho_P)$ and $V_0(\rho_P)$ is presented. At low perturber number densities ($\rho_P < 2.5 \times 10^{21}$ cm^{-3}), the Fermi model [15], the Alekseev-Sobel'man model [6, 22], and the Al-Omari-Reininger-Huber model [27] are often used to explain perturber effects on $\Delta(\rho_P)$. However, none of these models fits the experimental results obtained at higher perturber number densities using photoinjection [48, 80–85, 89–91] or field ionization measurements [4, 7, 27, 50–54, 97–99], nor can any of these models fit the temperature dependence of the experimental data presented in this work. The first model for $V_0(\rho_P)$ at high perturber densities was developed by Springett, Jortner, and Cohen [56] by modifying the Wigner-Seitz model [20, 21] in solid state physics and is presented in Chapter 2. The simplicity of this model has led to a myriad of theoretical modifications of the basic SJC model, which are also discussed here and compared to previous experimental results. The problems and strengths of these various theoretical models are then assessed.

A detailed description of the experimental apparatus employed throughout this work and the sample preparation method is given in Chapter 3. Chapter 3 also

provides purity and product information for the dopants and perturbers involved. Finally, this chapter includes a discussion of the procedures used in acquiring and analyzing field ionization data.

Chapter 4 presents our investigations of $\Delta(\rho_P)$ and $V_0(\rho_P)$ in atomic fluids. This chapter begins with a temperature study of the perturber induced shift $\Delta(\rho_P)$ for CH_3I in low density Ar and Kr [26]. We find a temperature dependence of $\Delta(\rho_P)$ that contradicts the standard low density models presented in Chapter 2. We then report the field ionization of various dopants (i.e., CH_3I, C_2H_5I, N,N-dimethylanaline and trimethylamine) in the atomic perturbers (i.e., Ar, Kr and Xe) at perturber densities ranging from low density to the density of the triple point liquid, at non-critical temperatures and on an isotherm near the critical isotherm [42–47]. These data show a decrease in the perturber induced shift of the dopant ionization energy near the critical point, which contrasts with the increase in the density dependent solvatochromic shift of vibrational and UVvisible absorption bands reported by numerous groups [2] in various perturbers. Chapter 4 next introduces the local Wigner-Seitz model developed by our group. The contradictory temperature behavior observed at low perturber densities and the critical point effect are then explained within this model.

In Chapter 5 we present our investigation of $\Delta(\rho_P)$ and $V_0(\rho_P)$ in molecular fluids. The experimental studies include the field ionization measurements of trimethylamine in methane and triethylamine in ethane at non-critical temperatures and on an isotherm near the perturber critical isotherm. Critical point effects similar to those observed in atomic fluids are presented. In order to extend the local Wigner-Seitz model to molecular fluids, various perturber/perturber intermolecular potentials and

methods used to calculate radial distribution functions were investigated. Finally, we discuss our studies of the fluorinated fluid carbon tetrafluoride and use our knowledge of $V_0(\rho_{\text{P}})$ in CH_4 and C_2H_6 to help predict the energy of the quasi-free electron in CF_4. We conclude this dissertation with an explanation of the differences between atomic and molecular supercritical fluids and with a discussion of the changes that will need to be made to the local Wigner-Seitz model to extend this model to polar fluids and to repulsive (i.e., positive zero-kinetic-energy electron scattering length) fluids.

Chapter 2

Perturber effects on dopant ionization energies

When a dopant atom or molecule is ionized in a perturber medium, a quasi-free electron and a cationic core are generated. The shift $\Delta(\rho_{\mathrm{P}})$ of the dopant ionization energy resulting from the interaction of the dopant with the perturber medium arises from two effects: (i) the optical electron/perturber interaction, and (ii) the dopant core/perturber interaction. These two interactions can be considered to be independent of each other. At low perturber densities, the interaction of the optical electron with the perturber is normally treated by invoking either elastic or inelastic electron scattering from the perturber. At higher perturber number densities, however, this approach is no longer valid. Instead, the quasi-free electron energy $V_0(\rho_{\mathrm{P}})$, also known as the minimum of the conduction band energy, is generally studied. For the dopant core/perturber interaction, on the other hand, a statistical treatment is required to calculate the average polarization energy. In this chapter, we will review the different theoretical approaches employed in modeling $\Delta(\rho_{\mathrm{P}})$ for systems at low and at high perturber number densities.

2.1 $\Delta(\rho_{\rm P})$ in low density perturbers

2.1.1 The Fermi model

At low perturber number densities, a dopant Rydberg state shifts in energy and the transition line shape broadens as a result of collisional interactions. In the 1930s, Fermi [15] presented a simple model to explain the shift of the high-n Rydberg states of alkali metals by perturbing particles that had been observed by Amaldi and Segrè [16]. Fermi assumed that, due to the large size of the high-n Rydberg states, the perturber particles interact separately with the electron and with the dopant core. Since high-n Rydberg electrons can be regarded as quasi-free, this model also applies to the shift of the dopant ionization energy. As a result, the perturber induced shift $\Delta(\rho_{\rm P})$ of the dopant ionization energy is then given by [15]

$$\Delta(\rho_{\rm P}) \;=\; \Delta_{sc}(\rho_{\rm P}) \;+\; \Delta_{pol}(\rho_{\rm P})\;, \tag{2.1}$$

where $\Delta_{sc}(\rho_{\rm P})$ is the shift resulting from scattering of the optical electron off of the perturber, and $\Delta_{pol}(\rho_{\rm P})$ is the shift due to the polarization of the perturber by the dopant core.

To obtain $\Delta_{sc}(\rho_{\rm P})$, the long-ranged Schrödinger equation for the electron must be solved [15, 17]. A formal treatment of this scattering problem is to perform a partial wave expansion, in which the radial wave function R(r) of the electron is decomposed into partial waves $\mathrm{R}_l(\mathrm{r})$ corresponding to the radial wave functions for different angular momenta l. Since the high-n electron velocity (which scales as n^{-1}) is quite small, the de Broglie wavelength (λ) of the election is relatively long. Thus, when this slow quasi-free electron scatters off of a perturber particle through

a short-ranged interaction potential, the electron does not see the detailed structure of the perturber. Therefore, only the spherically symmetric s-wave scattering (i.e., low-energy scattering) needs to be considered in the partial wave expansion.

Fermi [15] presented the Schrödinger equation as

$$\nabla^2 \psi \; + \; \frac{2m_e}{\hbar^2} \left(E - U - \sum_i V_i \right) \psi \; = \; 0 \; , \tag{2.2}$$

where m_e is the electron mass, $\hbar$ is the reduced Planck constant, and E is the eigenenergy. The potential energy operator in eq. (2.2) consists of the dopant core/electron potential U and the sum of the potentials V_i of the optical electron interacting with the ith perturber. By defining $\overline{\psi}$ as the spatial average of the wavefunction ψ over a dopant/perturber system having dimensions that are much smaller than the de Broglie wavelength λ, a spatial integration of the above Schrödinger equation gives [15, 17]

$$\nabla^2 \overline{\psi} \; + \; \frac{2m_e}{\hbar^2} \; (E - U) \; \overline{\psi} \; - \; \frac{2m_e}{\hbar^2} \; \overline{\sum_i V_i \, \psi} \; = \; 0 \; . \tag{2.3}$$

If the origin of the coordinate system is moved to the center of one perturber particle, $E - U$ is negligible in comparison with V_i, and $V_i = V(r)$ due to spherical symmetry around the origin. Together with the substitution $\psi \; = \; u(r)/r$, we find from eq. (2.2) that [15, 17]

$$\frac{d^2 u}{dr^2} \; - \; \frac{2m_e}{\hbar^2} \; V(r) \; u(r) \; = \; 0 \; . \tag{2.4}$$

$V(r)$ is nonzero only within the finite range R_0. Thus, at $r > R_0$ where $V(r)$ vanishes, $u(r)$ in eq. (2.4) is simply a linear function of r. In this range, ψ can be considered to equal $\overline{\psi}$ since the optical electron is far away from the perturber. Therefore, $u(r)$

can then be written as [15, 17]

$$u(r) \;=\; (r - A)\,\overline{\psi}\,, \tag{2.5}$$

where A is the electron scattering length, which is illustrated in Fig. 2.1. In the absence of perturbers, $u(r)$ should be a straight line (i.e., dotted line in Fig. 2.1) that goes through origin. The interaction of the electron with the perturbing medium, however, changes the asymptotic nature of the electron wave function. The scattering length A is then the distance through which the electron wave function is displaced with respect to the origin due to the presence of perturbers [17]. The phase shift δ_0 (the subscript "0" indicates $l = 0$) induced by the electron/perturber interaction potential $V(r)$ is related to A by [15, 17]

$$\delta_0 \;=\; 2\pi\,\frac{A}{\lambda} \;=\; \frac{p\,A}{\hbar} \;=\; q\,A\,, \tag{2.6}$$

where $p = \hbar\,q$ is the momentum of the scattered electron. We should note here that A can be either negative or positive depending upon the nature of the electron/perturber potential. In this dissertation, perturbers with negative scattering length are referred to as attractive gases (e.g., Ar, Kr and Xe), while positive A values indicate repulsive perturbers (e.g., He, Ne, H_2 and N_2).

Using eqs. (2.4) and (2.5), we can evaluate the spatial average [i.e., the last term in eq. (2.3)] as [15, 17]

$$\begin{aligned}
\frac{2m_e}{\hbar^2}\,\overline{\sum_i V_i\,\psi} \;&=\; \rho_{\rm P}\,\frac{2m_e}{\hbar^2}\int V(r)\,\psi\;d\tau \;=\; 4\,\pi\,\rho_{\rm P}\,\frac{2m_e}{\hbar^2}\int V(r)\,u(r)\,r\;dr \\
&=\; 4\,\pi\,\rho_{\rm P}\int u''(r)\,r\;dr \;=\; 4\,\pi\,\rho_{\rm P}\;\left|\,[u'(r)\,r\;-\;u(r)]\,\right|_0^{r'} \\
&=\; 4\,\pi\,A\,\rho_{\rm P}\,\overline{\psi}\,.
\end{aligned} \tag{2.7}$$

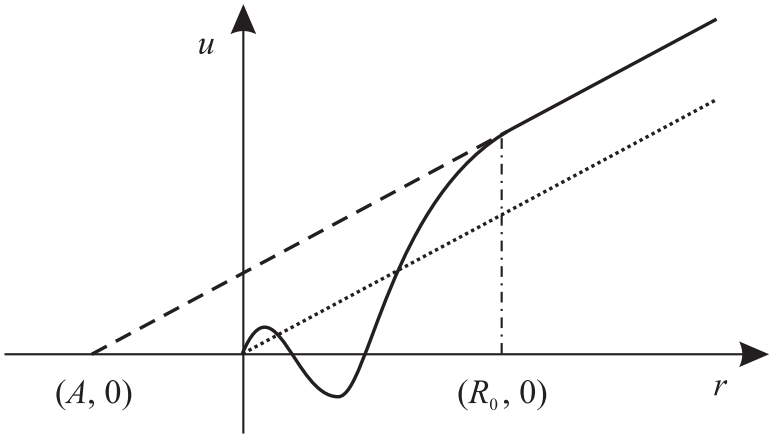

Figure 2.1: $u(r)$ from eq. (2.4) plotted as a function of r under different conditions: $(\cdot\ \cdot\ \cdot)$ solution in the absence of additional perturbers (i.e. $u(r) = r\,\overline{\psi}$), (—) real solution in the perturber medium, and (- - -) extension of the asymptotic solution (i.e. $u(r) = (r - A)\,\overline{\psi}$). A is the electron scattering length, and R_0 gives the range of the electron/perturber interaction potential.

Substitution of eq. (2.7) into eq. (2.3) gives [17]

$$\nabla^2\,\overline{\psi}\ +\ \frac{2m_e}{\hbar^2}\left(E - \frac{2\pi\hbar^2}{m_e}\,A\,\rho_{\rm P} - U\right)\overline{\psi}\ =\ 0\ . \tag{2.8}$$

When eq. (2.8) is compared with the Schrödinger equation for the electron in the potential of the cationic core without a perturber medium, or

$$\nabla^2\,\overline{\psi}\ +\ \frac{2m_e}{\hbar^2}\,(E_0 - U)\,\overline{\psi}\ =\ 0\ , \tag{2.9}$$

one can easily obtain the perturber-induced energy shift of the electron energy as

$$\Delta_{sc}(\rho_{\rm P})\ =\ \Delta E\ =\ E - E_0\ =\ \frac{2\pi\hbar^2}{m_e}\,A\,\rho_{\rm P}\ . \tag{2.10}$$

From the form of eq. (2.10), we see that (i) the electron energy decreases in the presence of attractive perturbers and increases in the presence of repulsive perturbers, and (ii) the scattering shift $\Delta_{sc}(\rho_{\rm P})$ is a linear function of the bulk perturber density $\rho_{\rm P}$.

Fermi's calculation of the polarization shift $\Delta_{pol}(\rho_{\rm P})$ assumed that the dopant core polarizes all of the perturber atoms within the orbit of the Rydberg electron, or [15,17]

$$\Delta_{pol}(\rho_{\rm P}) \;=\; -\,\frac{\alpha_{\rm P}}{2}\,\sum_{i}^{N} F_i(R_i)^2\;, \tag{2.11}$$

where $\alpha_{\rm P}$ is the polarizability of the perturber, $F_i(R_i)$ is the field at the position of the ith perturber due to the dopant core, R_i is the distance between the ith perturber and the dopant core, and N is the number of perturbers within the orbit of the Rydberg electron. For non-interacting perturbers, $F_i(R_i) = e/R_i^2$, and since F_i is a short-ranged interaction, the sum in eq. (2.11) can be converted to an integral over all perturbers [3–5, 15, 17–19]:

$$\Delta_{pol}(\rho_{\rm P}) \;=\; -\,\frac{\alpha_{\rm P}\,e^2}{2}\,(4\,\pi\,\rho_{\rm P})\,\int_{R_1}^{\infty}\frac{R^2}{R^4}\,dR \;=\; -\,2\,\pi\,\alpha_{\rm P}\,e^2\,\rho_{\rm P}\,\frac{1}{R_1}\;, \tag{2.12}$$

where R_1 is a cut-off radius indicating the minimum distance between the perturber and the dopant core. Fermi assumed that all of the perturbers are uniformly distributed in the container volume. Therefore, the Wigner-Seitz radius [20, 21],

$$r_{_s} \;=\; \sqrt[3]{\frac{3}{4\,\pi\,\rho_{\rm P}}}\;, \tag{2.13}$$

could be used as a cut-off for the integral. Substituting r_s for R_1 in eq. (2.12) gives a polarization shift of [3–5, 15, 17–19]

$$\Delta_{pol}(\rho_{\rm P}) \;=\; -\,\left(\frac{32}{3}\pi^4\right)^{1/3}\,\alpha_{\rm P}\,e^2\,\rho_{\rm P}^{4/3} \;\approx\; -\,10\,\alpha_{\rm P}\,e^2\,\rho_{\rm P}^{4/3}\;. \tag{2.14}$$

Within Fermi's original model, therefore, the total perturber-induced energy shift becomes

$$\Delta(\rho_{\rm P}) \;=\; \frac{2\pi\hbar^2}{m_e}\,A\,\rho_{\rm P} \;-\; 10\,\alpha_{\rm P}\,e^2\,\rho_{\rm P}^{4/3}\;. \tag{2.15}$$

The Fermi model predicts that the perturber-induced energy shift of a high-n Rydberg state is independent of n for any principal quantum number that is large enough to give a sufficiently long de Broglie wavelength. This prediction has been experimentally verified in [18, 19]. Since the perturber-induced energy shift is independent of n, the assumption that the Fermi model can also be used to explain the shift $\Delta(\rho_{\mathrm{P}})$ of the dopant ionization energy is valid. However, eq. (2.15) predicts that $\Delta(\rho_{\mathrm{P}})$ is a non-linear function of ρ_{P}, which is not experimentally observed at low perturber number density (cf. Section 2.1.4 for details).

2.1.2 The Alekseev-Sobel'man model

Alekseev and Sobel'man [6, 22] provided a formal treatment of $\Delta(\rho_{\mathrm{P}})$ within the impact approximation of line broadening theory, which assumes that the time between collisions is long in comparison to the time of the collision. Moreover, only two body interactions were considered. These approximations limit the applicability of the results to the low perturber number density regime. Alekseev and Sobel'man [6, 22] again assume the independence of $\Delta_{sc}(\rho_{\mathrm{P}})$ and $\Delta_{pol}(\rho_{\mathrm{P}})$. Their model includes the contribution of various angular momenta states on the scattering of a quasi-free electron from a perturber, but disregards the spin dependence of each electron. Within this approach, one obtains the generalized expression [6, 22]

$$\Delta_{sc}(\rho_{\mathrm{P}}) \;=\; \frac{\hbar^2}{m_e}\,\rho_{\mathrm{P}} \int \left[\frac{\pi}{q}\,\sum_{l}(2\,l\;+\;1)\,\sin 2\delta_l\right] W(q)\,dq\;, \tag{2.16}$$

where δ_l is the l-wave phase shift of the scattered electron, and $W(q)$ is the excited-state momentum distribution (i.e., $\hbar\,q$ is the momentum). The momentum distribu-

tion must satisfy the normalization relation [6, 22]

$$\int W(q)\, dq \;=\; 1\;. \tag{2.17}$$

This expression for $\Delta_{sc}(\rho_{\rm P})$ is valid for low-energy and high-energy electron scattering, since eq. (2.16) accounts for different angular momentum states. Although Alekseev and Sobel'man [6, 22] felt that different angular momentum states could exist in even low-energy electron scattering events, the scattering is predominately s-wave for the systems considered here. For s-wave scattering, the bracketed content in eq. (2.16) is close to the limiting value of [6, 22]

$$\lim_{q\to 0}\left(\frac{\pi}{q}\,\sin 2\delta_0\right) \;=\; \frac{2\,\pi\,\delta_0}{q} \;=\; 2\,\pi\,A\;. \tag{2.18}$$

Substitution of eq. (2.18) into eq. (2.16) gives, after simplification, the original Fermi result of eq. (2.10) for $\Delta_{sc}(\rho_{\rm P})$.

To calculate $\Delta_{pol}(\rho_{\rm P})$, Alekseev and Sobel'man [6, 22] also used the same form for the dopant core/perturber polarization potential as did Fermi [15], namely

$$V(R) \;=\; -\,\frac{\alpha_{\rm P}\,e^2}{2\,R^4}\;. \tag{2.19}$$

Within the Aleekseev and Sobel'man model, the dopant core is regarded as a classical oscillator. Therefore, when the dopant core collides with the perturber particle, the oscillation frequency changes. Under the assumption that the motions of the dopant core and the perturber are quasiclassical, the distance between the cationic core and the perturber at any time t can be written as [3, 5, 6, 22]

$$R(b,v,t) = \sqrt{b^2 \;+\; v^2\,(t-t_0)^2}\;. \tag{2.20}$$

where b is the impact parameter at the time of nearest approach t_0 (or the perpendicular distance from the core center to the path of the perturber), and v is the thermal velocity of the perturbers. The total frequency shift $\chi(R)$ generated by the effective collisions of all perturbers with different impact parameters can, therefore, be computed by summing over all of the perturbers. Thus, [3, 5, 6, 22]

$$\chi(R) \;=\; \frac{\Delta_{pol}}{\hbar} \;=\; -\,\frac{\alpha_{\rm P}\,e^2}{2\,\hbar}\;\sum_i \frac{1}{R_i^4} \;=\; -\,\frac{\alpha_{\rm P}\,e^2}{2\,\hbar}\;\sum_i \left[b_i^2 \;+\; v^2\,(t-t_{0,i})^2\,\right]^{-2}\;. \quad (2.21)$$

However, during the collisional perturbation the phase of the oscillation is also modified. This phase shift $\eta(b, v)$, which is determined by the passage of one perturber having the impact parameter b and the velocity v, can be written as [3, 5, 6, 22]

$$\eta(b,v) \;=\; -\,\frac{\alpha_{\rm P}\,e^2}{2\,\hbar}\;\int_{-\infty}^{\infty}\left[b^2 \;+\; v^2\,(t-t_0)^2\,\right]^{-2}\;dt \;=\; -\,\frac{\pi\,\alpha_{\rm P}\,e^2}{4\,\hbar\,v\,b^3}\;. \quad (2.22)$$

The cut-off radius b of the collision is not yet specified in eq. (2.22).

Weisskopf [23, 24] assumed that a collision between a dopant core and a perturber occurs when the phase of the oscillation changes, or $\eta(b) \geq \eta_0 = 1$. Substituting η_0 into eq. (2.22) and solving for b gives the effective interaction radius [3, 5, 6, 22–24]

$$r_w \;=\; |b_0| \;=\; \left(\frac{\pi\,\alpha_{\rm P}\,e^2}{4\,\hbar\,v}\right)^{1/3}\;, \quad (2.23)$$

which is also known as the Weisskopf radius. However, there are two possible deficiencies in the impact approximation. First, the choice of the limiting value η_0 is arbitrary and yields no physical insight. Secondly, there are no grounds to ignore the contributions from small but more frequent phase shifts. These deficiencies were

eliminated by expressing the polarization shift $\Delta_{pol}(\rho_{\rm P})$ as [6, 22]

$$\Delta_{pol}(\rho_{\rm P}) \;=\; 2\,\pi\,\hbar\,\rho_{\rm P}\,v\int_0^\infty b\,\sin\eta(b,v)\,db\;. \tag{2.24}$$

By substituting eq. (2.22) into eq. (2.24), we obtain

$$\begin{aligned}\Delta_{pol}(\rho_{\rm P}) \;&=\; 2\,\pi\,\hbar\,\rho_{\rm P}\,v\int_0^\infty b\,\sin\left(-\,\frac{\pi\,\alpha_{\rm P}\,e^2}{4\,\hbar\,v\,b^3}\right)\,db \\ &=\; -\,2^{-7/3}\,\sqrt{3}\,\pi^{5/3}\,\Gamma(1/3)\,(\alpha_{\rm P}\,e^2)^{2/3}\,(\hbar\,v)^{1/3}\,\rho_{\rm P} \\ &\approx\; -\,6.22\,(\alpha_{\rm P}\,e^2)^{2/3}\,(\hbar\,v)^{1/3}\,\rho_{\rm P}\;,\end{aligned} \tag{2.25}$$

where $\Gamma(1/3) \approx 2.679$ is the Gamma function. Therefore, the total energy shift in the Alekseev-Sobel'man model is given by

$$\Delta(\rho_{\rm P}) \;=\; \frac{2\,\pi\,\hbar^2}{m_e}\,A\,\rho_{\rm P} \;-\; 6.22\,(\alpha_{\rm P}\,e^2)^{2/3}\,(\hbar\,v)^{1/3}\,\rho_{\rm P}\;. \tag{2.26}$$

If one separates the integral in eq. (2.24) into two parts having integration limits from 0 to r_w and from r_w to ∞, one notices that [6, 22]

$$\int_0^{r_w} b\,\sin\eta(b,v)\,db \;\ll\; \int_{r_w}^\infty b\,\sin\eta(b,v)\,db\;. \tag{2.27}$$

Thus, the collisions with perturber particles outside the Weisskopf radius r_w (small frequency shifts) dominate the energy shift. On the other hand, strong collisions with large frequency shifts determine the spectral line broadening [6, 22]. This result also implies the possibility of using r_w [i.e., eq. (2.23)] as the cut-off radius R_1 [i.e., the lower integration limit in eq. (2.12)] in the original Fermi model. Substitution of eq. (2.23) into eq. (2.12) yields [25]

$$\begin{aligned}\Delta_{pol}(\rho_{\rm P}) \;&=\; -\,(32\,\pi^2)^{1/3}\,(\alpha_{\rm P}\,e^2)^{2/3}\,(\hbar\,v)^{1/3}\,\rho_{\rm P} \\ &\approx\; -\,6.81\,(\alpha_{\rm P}\,e^2)^{2/3}\,(\hbar\,v)^{1/3}\,\rho_{\rm P}\;,\end{aligned} \tag{2.28}$$

which is almost identical to eq. (2.25). Therefore, the choice of cut-off radius is crucial in determining the cationic core/perturber polarization energy.

The Alekseev-Sobel'man model in eq. (2.26) [or eq. (2.28)] shows that the total energy shift $\Delta(\rho_{\rm P})$ should be linearly dependent on the perturber number density $\rho_{\rm P}$. This model also has an implicit temperature dependence through the thermal velocity v, with a lower temperature indicating a smaller v which leads to a smaller red shift in attractive perturbers. Since eq. (2.28) has only a single adjustable parameter, namely the zero-kinetic-energy electron scattering length A, this model has been used to evaluate A for systems with perturber number densities of up to 2×10^{21} cm^{-3} [5,19]. In the present work, we will show that the temperature dependence predicted by the Alekseev-Sobel'man model is wrong (cf. Chapter 4). Thus, the scattering lengths determined within this model should always be verified with scattering lengths obtained from another method.

2.1.3 The Al-Omari-Reininger-Huber model

Al-Omari, Reininger and Huber [27] assumed that the Fermi-Alekseev-Sobel'man approach to the electron/perturber interaction was valid, but that the dopant cationic core/perturber interaction could be modeled more accurately within a general statistical method. Using a canonical distribution, the probability of sampling a particular polarization energy W in the static limit is given by [27]

$$P(W) = \frac{\int \cdots \int \delta\left(W - w_+(r_1, \ldots, r_N)\right) \times e^{-\beta U(r_1,\ldots,r_N)} \prod_i dr_i}{\int \cdots \int e^{-\beta U(r_1,\ldots,r_N)} \prod_i dr_i} \,, \tag{2.29}$$

where $\beta = 1/(k_B T)$ [$k_B \equiv$ Boltzmann constant], $U(r_1, \ldots, r_N)$ is the multidimensional potential energy of the system prior to ionization, and $w_+(r_1, \ldots, r_N)$ is the cationic

core/medium polarization energy. At low density, the effects of the ground-state interaction potential $U(r_1, \ldots, r_N)$ can be ignored. Thus, $P(W)$ simplifies to [27]

$$P(W) = \langle\, \delta(W - w_+(r_1, \ldots, r_N)) \,\rangle \;, \tag{2.30}$$

where $\langle \cdots \rangle$ indicates an average over all perturber positions. Al-Omari, Reininger and Huber [27] then considered a general inverse power interaction having the form $-\sum_k C_k\, r^{-k}$ $(k > 3)$. By using the method of steepest descent (or the saddle-point approximation), they determined that the most probable polarization energy W_M is [27]

$$W_M = -\left(\frac{(3J_k/k)^{k/(k-3)}\ (2k-6)}{2k-3} \right)^{(k-3)/3} \;, \tag{2.31}$$

where

$$J_k \;=\; \frac{4\,\pi}{3}\,\Gamma(1-3/k)\;\rho_{\rm P}\;C_k^{3/k} \;, \quad k > 3 \;. \tag{2.32}$$

Since the most probable polarization energy represents the maximum of the canonical distribution $P(W)$, the polarization energy for the dopant cationic core will also be at W_M. Assuming a dipole/induced dipole interaction, the necessary inverse power law is $C_4 \;=\; \alpha_{\rm P}\, e^2/2$ and, therefore, $k = 4$. Since $\Gamma(1/4) \approx 3.6256$, eq. (2.31) becomes

$$W_M \;\approx\; -\,9.45\;\alpha_{\rm P}\, e^2\, \rho_{\rm P}^{4/3} \;, \tag{2.33}$$

which is similar to the original Fermi model both in size and in the non-linear dependence on $\rho_{\rm P}$. Since $W_M = \Delta_{pol}(\rho_{\rm P})$, the total perturber-induced energy shift is given by

$$\Delta(\rho_{\rm P}) = \frac{2\pi\hbar^2}{m_e}\; A\;\rho_{\rm P} - 9.45\;\alpha_{\rm P} e^2 \rho_{\rm P}^{4/3} \;. \tag{2.34}$$

2.1.4 Previous experimental results

In the 1930s, Amaldi and Segrè [16] observed for the first time a perturber induced shift of high-n Rydberg states of sodium and of potassium. To explain this phenomenon, Fermi developed the model detailed in Section 2.1.1, which, as we have shown, became the starting point for more elaborate models. Following these pioneering studies, later researchers measured the shifts of high-n Rydberg states for various alkali metal/perturber systems at low perturber densities ($\rho_{\rm P} \leq 5 \times 10^{20}$ cm^{-3}) [28–35]. (Alkali metals were used as dopants in nearly all of the early experiments due to their hydrogen like structure, high vapor pressures in comparison to other metals, and low ionization energies.) The shift of Rb high-n Rydberg states in He, Ne and Ar at densities up to 1.6×10^{20} cm^{-3} [28], and the shift of Na, Rb and Cs high-n Rydberg states in H_2 and N_2 at densities up to 1.4×10^{20} cm^{-3} [29] were reported by Ny and Ch'en in 1937 and 1938, respectively. Füchtbauer, *et al.* studied the high-n Rydberg states of K in He at densities up to 5.4×10^{20} cm^{-3} [30], and that of Pb in Ne at densities up to 4.3×10^{20} cm^{-3} [31]. Füchtbauer and Schulz were the first to notice that the dopant high-n Rydberg states shifted to lower energies for the perturbers Ar, Kr, Xe, methane, ethane and propane in contrast to the perturber-induced blue shift of these same states in He and Ne [32]. In all of these studies, the observed perturber-induced shifts did not show the expected $\rho_{\rm P}^{4/3}$ dependence [cf. eq. (2.15)], but instead were all linearly dependent on $\rho_{\rm P}$. As new light sources became available, work resumed on this problem in the 1970s when Tan and Ch'en extended the measurements of Cs in all of the rare gases to perturber densities up to 1.4×10^{20} cm^{-3} [33]. A few years later, Weber and Niemax [34, 35] measured

Rb and Sr in rare gases at really low densities ($\leq 10^{16}$ cm^{-3}) using a doppler-free two-photon absorption technique. These studies showed that the perturber induced shift of high-n Rydberg states was linearly dependent on ρ_{P} even at the lowest of perturber densities [34, 35]. The early experimental measurements [28–35] discussed above indicated that the Fermi model was invalid even at the lowest densities; however, they did show that the general perturber induced shift of high-n Rydberg states was not only independent of n but was also independent of the nature of the dopant.

The development of laser spectroscopy and synchrotron radiation light sources enabled studies over a much wider energy range with higher resolution in the 1980s. By choosing organic dopants with decent vapor pressures at low temperatures, researchers were able to perform experiments at larger perturber densities under cleaner conditions [3, 18, 19, 25, 36–41]. One of the most commonly used dopants in this research is CH_3I because [3]: (i) it has quasi-atomic Rydberg states that are similar to those of Xe, (ii) it has a high vapor pressure, (iii) it is chemically stable, and (iv) its Rydberg series and first two ionization energies are located at energies lower than the cut-off of the commonly used windows (e.g., LiF and MgF_2), enabling higher density gas phase experiments. Köhler, *et al.* [19] presented a systematic strategy to determine the ionization energy by fitting the experimental excitation energies of high-n Rydberg states to the Rydberg equation. Using this method [19], they obtained the perturber induced shift $\Delta(\rho_{\mathrm{P}})$ of the CH_3I ionization energy in He, Ne, Ar and Kr (at densities up to 23.0, 24.0, 11.3, and 6.6 $\times 10^{20}$ cm^{-3}, respectively). Evans, *et al.* presented the ionization energy shift of C_2H_5I in Ar at densities up to 4.9 $\times 10^{20}$ cm^{-3} [5]. In addition, Steinberger, *et al.* studied the shift of high-n CH_3I Rydberg

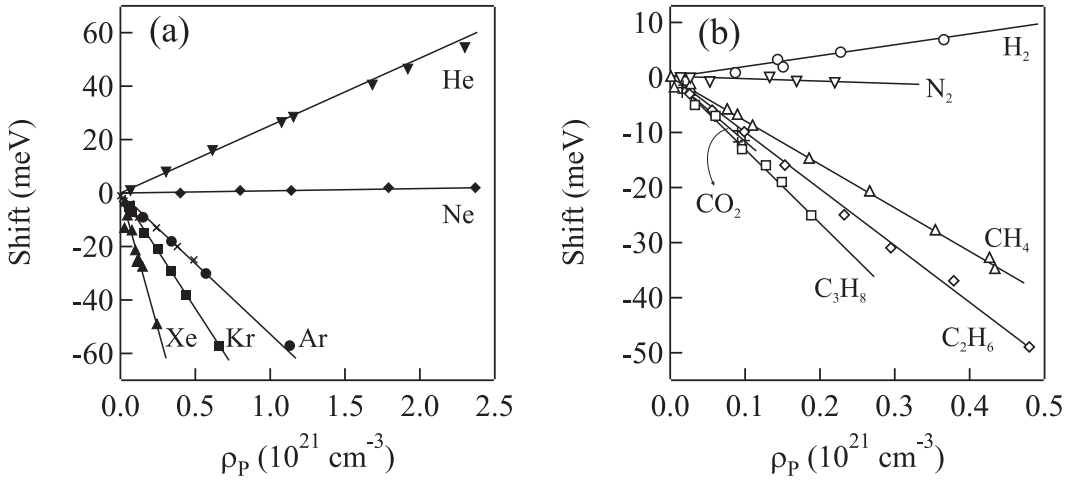

Figure 2.2: (a) The perturber induced shift $\Delta(\rho_P)$ of the first ionization energy of CH_3I in (▼) He [19]; (♦) Ne [19]; (●) Ar [19]; and (■) Kr [19] as a function of the perturber number density ρ_P. Also included in this graph are (×) $\Delta(\rho_P)$ of the C_2H_5I first ionization energy in Ar [5] and ▲ the average Xe-induced shift of the nd ($^2E_{3/2}$) series ($10 \leq n \leq 14$) of CH_3I [36] plotted as a function of ρ_P (b) Average perturber induced shifts of the CH_3I nd ($^2E_{3/2}$) series in H_2 (○, $10 \leq n \leq 16$, [37]) and CO_2 (+, $11 \leq n \leq 14$, [40]) plotted as a function of ρ_P. also included on this graph is the average perturber-induced shifts of the CH_3I nd' ($^2E_{1/2}$) series in N_2 (▽, $9 \leq n \leq 15$, [38]), methane (△, $10 \leq n \leq 14$, [39]), ethane (◇, $10 \leq n \leq 14$, [39]), and propane (□, $10 \leq n \leq 14$, [39]). The solid lines in (a) and (b) are provided as a visual aid.

states in Xe [36]. The experimental results measured in rare gases are summarized in Fig 2.2a. Similarly, Fig 2.2b summarizes experimental data for the shift of CH_3I high-n Rydberg states in molecular perturbers. All the referenced results in Fig 2.2 clearly show that the energy shift is linear in perturber density.

In order to test the accuracy of different theoretical models, Köhler, *et al.* [19] and Evans, *et al.* [5] compared the Fermi model, the Alekseev-Sobel'man model and the Al-Omari-Reininger-Huber model to selected experimental data in the rare gases. For example, Fig.2.3 presents the calculation of the perturber induced shift $\Delta(\rho_P)$ from the original Fermi model [i.e., eq. (2.15)], the Alekseev-Sobel'man model [i.e., eq. (2.26)], and the Al-Omari-Reininger-Huber model [i.e., eq. (2.34)] in comparison

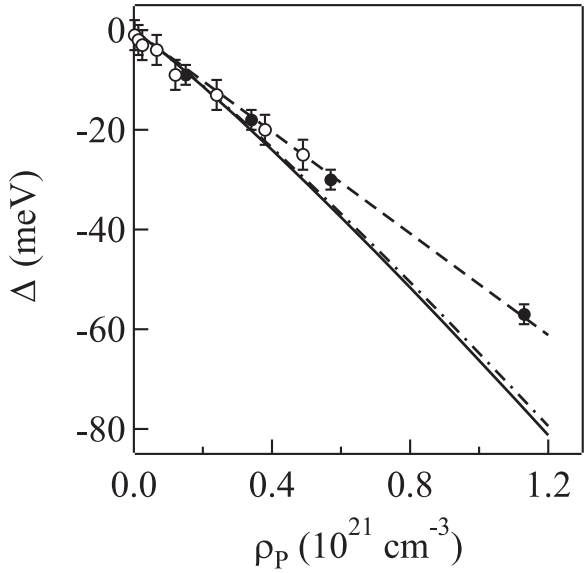

Figure 2.3: Shift $\Delta(\rho_{\rm P})$ of the first ionization energy of (•) CH_3I [19] and of (∘) C_2H_5I [5] plotted as a function of Ar number density. (—) represents the original Fermi model [i.e., eq. (2.15)]; (- - -) is the Alekseev-Sobel'man model [i.e., eq. (2.26)]; while (- · -) is the Al-Omari-Reininger-Huber model [i.e., eq. (2.34)]. The parameters [18] for all of the calculations are $A = 0.89$ Å, $\alpha_{\rm P} = 1.63$ Å^3, and $v = 430$ m/s. See text for discussion.

to experimental data [5, 19]. The agreement between the Alekseev-Sobel'man model and the experimental data is obvious in this low density regime when the zero-kinetic-energy electron scattering length was supplied from electron swarm methods [18]. Therefore, eq. (2.26) was often applied to the experimental $\Delta(\rho_{\rm P})$ in order to evaluate the zero-kinetic-energy electron scattering lengths of various atoms and molecules. A summary of the zero-kinetic-energy scattering lengths and scattering cross-sections (i.e., $\sigma = 4\pi A^2$ [15]) determined from eq. (2.26) is given in Table 2.1 [5].

Table 2.1: Experimental total shift rates $\Delta/\rho_{\rm P}$, zero-kinetic-energy electron scattering lengths A and cross-sections σ determined from eq. (2.26) [5]. All experimental data were obtained at ambient temperature (approximately 25°C).

	(10^{-23} eV cm^3)	(Å)	(Å^2)	
Perturber	$\Delta/\rho_{\rm P}$	A	σ	Ref.
He	2.44	0.57	4.1	[25]
H_2	1.62	0.49	3.0	[37]
N_2	0.00	0.19	0.45	[38]
Ne	0.09	0.090	0.10	[25]
Ar	-4.75	-0.82	8.4	[41]
CH_4	-7.86	-1.38	23.8	[39]
Kr	-8.60	-1.60	32.2	[25]
C_2H_6	-10.1	-1.76	38.9	[39]
CF_4	-8.65	-1.80	41	[5]
CO_2	-11.8	-2.24	63.1	[40]
C_3H_8	-12.9	-2.28	65.3	[39]
Xe	-16.8	-3.24	132	[36]
SF_6	-24.7	-4.84	290	[5]
c-C_4F_8	-29.6	-6.18	480	[5]

2.2 $\Delta(\rho_{\rm P})$ in high density perturbers

2.2.1 Theoretical approach

At high perturber number densities, the separability of the electron/perturber and dopant core/perturber interactions remains valid. Therefore, the perturber-induced energy shift $\Delta(\rho_{\rm P})$ can still be written as a sum of interactions, namely [3, 26, 42–47]

$$\Delta(\rho_{\rm P}) \;=\; P_+(\rho_{\rm P}) \;+\; V_0(\rho_{\rm P})\;, \tag{2.35}$$

where $P_+(\rho_{\rm P})$ is the (adiabatic) ensemble average dopant core/perturber polarization energy arising from the perturber distribution about the neutral dopant [48], and $V_0(\rho_{\rm P})$ is the quasi-free electron energy in the perturber medium. The calculation of the polarization energy $P_+(\rho_{\rm P})$ at high perturber number density is an extension of

the approach used to determine $\Delta_{pol}(\rho_{\rm P})$. To extend the basic statistical model used for $\Delta_{pol}(\rho_{\rm P})$, one must first determine the transport properties of the polarization potential in the perturbing fluid. Lekner [49] investigated the electron motion in liquid argon and concluded that the long-ranged polarization force between a charged particle and a polarizable perturber was screened by the other perturber particles. Therefore, the transport properties depended on the fluid structure that, in turn, can be described through the radial distribution function $g(r)$.

Following Lekner, later researchers [42, 48, 50–54] provided the formalism to calculate $P_+(\rho_{\rm P})$ using a statistical mechanical model. Within this model, the dopant core/perturber polarization energy $w_+(r_1, \ldots, r_N)$ in the canonical distribution function [i.e., eq. (2.29)] can be written as a sum of pairwise potentials, or [27,42,48,50–54]

$$w_+(r_1, \ldots, r_N) \;=\; -\,\frac{1}{2}\,\alpha_{\rm P}\,e^2\,\sum_i^N r_i^{-4}\,f_+(r_i)\;, \tag{2.36}$$

with $f_+(r)$ being a screening function [49] that incorporates the repulsive interactions between the induced dipoles in the perturbing medium. The screening function is calculated from [48, 49]

$$f_+(r) \;=\; 1 \;-\; \pi\alpha_{\rm P}\rho_{\rm P}\int_0^\infty s^{-2}\,ds\int_{|r-s|}^{r+s} t^{-2}f_+(t)\left[\frac{g^{(3)}(r,s,t)}{g_{\rm PD}(r)}\right]\theta(r,s,t)\,dt\;, \tag{2.37}$$

where

$$\theta(r,s,t) \;=\; \frac{3}{2\,s^2}\,(s^2+t^2-r^2)(s^2-t^2+r^2) \;+\; (r^2+t^2-s^2)\;, \tag{2.38}$$

and where the integration variables s and t represent the distance between the atom of interest and all other perturber atoms. In eq. (2.37), $g^{(3)}(r,s,t)$ is the three-body correlation function and $g_{\rm PD}(r)$ is the dopant/perturber radial distribution function.

Based upon the Kirkwood superposition approximation [55],

$$g^{(3)}(r,s,t) \;=\; g_{\rm PD}(r)\, g_{\rm PP}(s)\, g_{\rm PD}(t)\;, \tag{2.39}$$

where $g_{\rm PP}(s)$ is the perturber/perturber radial distribution function. Thus, eq. (2.39) allows eq. (2.37) to be written as [48]

$$f_+(r) \;=\; 1 \;-\; \pi\,\alpha_{\rm P}\,\rho_{\rm P} \int_0^\infty s^{-2}\, g_{\rm PP}(s)\, ds \int_{|r-s|}^{r+s} t^{-2}\, f_+(t)\, g_{\rm PD}(t)\, \theta(r,s,t)\, dt\;. \tag{2.40}$$

The first moment of the Fourier transform of eq. (2.29) with eqs. (2.37) and (2.38) yields the (adiabatic) ensemble average dopant core/perturber polarization energy $P_+(\rho_{\rm P})$ as [42, 48, 50–54]

$$P_+(\rho_{\rm P}) \;\equiv\; m_1(\rho_{\rm P}) \;=\; -\,4\,\pi\,\rho_{\rm P} \int_0^\infty g_{\rm PD}(r)\; w_+(r)\; r^2\, dr\;. \tag{2.41}$$

On the other hand, the modeling of the quasi-free electron energy $V_0(\rho_{\rm P})$ in dense perturber fluids is a knotty problem and, therefore, is less understood in comparison to that in low density gases or in crystalline solids. In low density gases (cf. Section 2.1), the problem reduces to the scattering of a free electron from a single perturber. While in crystalline solids, the symmetry and fixed position of perturbing particles again reduces the complexity of modeling the quasi-free electron energy. Although the problem in fluids is difficult, researchers have developed various theoretical models for $V_0(\rho_{\rm P})$ that cover the perturber density range from low density up to the density of the triple-point liquid. Some of these models are presented below.

a. The Wigner-Seitz (WS) theory

A myriad of theoretical models for $V_0(\rho_{\rm P})$ in dense gases and fluids arose from variations in the Wigner-Seitz model [20,21], which was originally developed for solid state physics. In a symmetric homogeneous crystal, the symmetry of the problem allows one to solve the one-electron Schrödinger equation in the Wigner-Seitz cell, instead of the entire crystalline lattice, in order to determine the energy of the system. The Wigner-Seitz cell around one lattice point (e.g., the center of one atom for crystals that have only one atom in the primitive unit cell) contains all space points that are closer to this center lattice point than to other lattice points. In another words, if we draw lines between a central atom and all its closest neighbor atoms, the planes bisecting and perpendicular to these lines will form a polyhedral cell. Wigner and Seitz [20, 21] replaced these polyhedral cells with spheres that had the same volume as the cell. This boundary condition required that the radius of the spheres be dependent on the density of the atoms in the crystal. Thus, the Wigner-Seitz radius is calculated from eq. (2.13).

Within the Wigner-Seitz model, the one-electron potential V in each Wigner-Seitz cell is now a spherically symmetric potential $V(r)$, which has the translational symmetry [20, 21]

$$V(r) \;=\; V(r + 2r_s)\;. \tag{2.42}$$

Because of this periodic symmetry, the derivative of the wave function vanishes at the boundary of the Wigner-Seitz cell sphere. Therefore, one can obtain the wave function ψ in each sphere and the ground-state energy of the quasi-free electron $V_0(\rho_{\rm P})$

by solving [20, 21]

$$\nabla^2\psi \;+\; \frac{2\,m_e}{\hbar^2}\;[V_0 - V(r)]\;\psi \;=\; 0\;, \tag{2.43}$$

with the boundary condition

$$\left(\frac{\partial\psi}{\partial r}\right)\Bigg|_{r=r_s} \;=\; 0\;. \tag{2.44}$$

Since $V(r)$ has not yet been specified, the differences in the various Wigner-Seitz based theoretical models for $V_0(\rho_{\rm P})$ lie in the choice of $V(r)$. Additionally, the exact periodicity of the Wigner-Seitz model no longer holds in dense gases. Therefore, eq. (2.42) becomes an average translational symmetry.

b. The Springett-Jortner-Cohen (SJC) model

Springett, Jortner and Cohen [56] considered the potential $V(r)$ in eq. (2.43) as being a sum of two parts: V_{in}, the potential inside the Wigner-Seitz sphere, and V_{out}, the mean interaction potential due to all atoms outside the sphere. In general, both parts should contain a polarization potential and a Hartree-Fock potential incorporating the Coulomb and exchange interaction. However, in V_{out}, the short-ranged Hartree-Fock potential can be neglected.

To solve V_{out}, Springett, Jortner and Cohen [56] assumed that the dense fluid was structureless. This assumption implies that the lattice for the fluid, which is determined by the perturber/perturber radial distribution function $g_{\rm PP}(r)$, simplifies to

$$g_{\rm PP}(r) = \begin{cases} 0\;, & r < r_s\;, \\ 1\;, & r > r_s\;. \end{cases} \tag{2.45}$$

Moreover, since the fluid is structureless, the screening function $f_{-}(r)$ (which represents the screening of the interaction between the quasi-free electron and a single

perturber by all remaining perturber atoms in the fluid) can be approximated as the Lorentz local-field screening function, or [49]

$$f_{-}(r) \;=\; \begin{cases} 1\,, & r < r_s\,, \\ \left(1 \;+\; \frac{8}{3}\,\pi\,\alpha_{\rm P}\,\rho_{\rm P}\right)^{-1}\,, & r > r_s\,. \end{cases} \tag{2.46}$$

Within the structureless fluid approximation, V_{out} is given by [56]

$$\begin{aligned} V_{out} \;&=\; -\,\frac{\alpha_{\rm P}\,e^2\,\rho_{\rm P}}{2}\int_{r_s}^{\infty}\frac{g(r')\,f_{-}(|r-r'|)}{|r-r'|^4}\,d^3r' \\ &=\; -\,\frac{3\,\alpha_{\rm P}\,e^2}{2\,r_s^4}\left(1 \;+\; \frac{8}{3}\,\pi\,\alpha_{\rm P}\,\rho_{\rm P}\right)^{-1}\,. \end{aligned} \tag{2.47}$$

On the other hand, V_{in} was given as the sum of a Hartree-Fock potential $V_{HF}(r)$ and a polarization potential $V_P(r)$. By assuming that the electron charge is distributed uniformly in the arbitrarily chosen range $r_s/2 \le r \le r_s$, Springett, Jortner, and Cohen presented the polarization part as [56]

$$V_P(r) \;\approx\; -\,\frac{\alpha_{\rm P}\,e^2}{2}\int_{r_s/2}^{r_s}\frac{d^3r}{r^4}\;\Big/\;\int_{r_s/2}^{r_s}d^3r \;\approx\; -\,\frac{12\,\alpha_{\rm P}\,e^2}{7\,r_s^4}\,. \tag{2.48}$$

As a further simplification, these authors replaced the Hartree-Fock potential $V_{HF}(r)$ by a hard-core pseudopotential $V_a(r)$,

$$V_a(r) \;=\; \begin{cases} \infty\,, & r < r_h\,, \\ 0\,, & r > r_h\,, \end{cases} \tag{2.49}$$

where r_h is the hard-sphere radius obtained from the effective scattering cross-section of the Hartree-Fock field. Within these approximations, the total potential $V(r)$ in eq. (2.43) becomes

$$\begin{aligned} V(r) \;&=\; V_a(r) \;+\; V_P(r) \;+\; V_{out}(r) \\ &=\; V_a(r) \;-\; \frac{3\,\alpha_{\rm P}\,e^2}{2\,r_s^4}\left[\frac{8}{7} \;+\; \left(1 \;+\; \frac{8}{3}\,\pi\,\alpha_{\rm P}\,\rho_{\rm P}\right)^{-1}\right] \\ &=\; V_a(r) \;+\; U_P\,, \end{aligned} \tag{2.50}$$

where U_P is the total polarization energy and is constant for a given perturber number density.

With the potential defined by eq. (2.50), eq. (2.43), given the boundary conditions of eq. (2.44) and $\psi(r_h) = 0$, has a simple analytical solution, namely

$$\psi(r) \;=\; \frac{1}{r}\,\sin\left[k_0\,(r\,-\,r_h)\right]\,, \tag{2.51}$$

where

$$\tan\left[k_0\,(r_s\,-\,r_h)\right] \;=\; k_0\,r_s\,. \tag{2.52}$$

Thus, $V_0(\rho_{\rm P})$ is given by

$$V_0(\rho_{\rm P}) \;=\; U_P \;+\; E_k(\rho_{\rm P}) \;=\; U_P \;+\; \frac{\hbar^2\,k_0^2}{2\,m_e}\,. \tag{2.53}$$

c. Other methods and simulations

Several additional Wigner-Seitz type models for $V_0(\rho_{\rm P})$ have been developed. All of these models generally use the Wigner-Seitz radius as the boundary condition for the wavefunction, but differ in the choice of $V(r)$. Plenkiewicz, *et al.* [57–65] use the potential form [57]

$$V(r) \;=\; V_{out}(r) + V_{in}(r) \;=\; V_{out}(r) + V_l^{ion}(r) + V_{Coul}(r) + V_x(r) + V_c(r)\,, \tag{2.54}$$

which contains five parts:

1. $V_{out}(r)$ is calculated using the same expression [i.e., eq. (2.47)] as in the SJC model with the same choice of screening function $f_-(|r - r'|)$ [i.e., eq. (2.46)]. However, to account for the fluid structure, they calculated the radial distribu-

tion function $g_{\mathrm{PP}}(r')$ by solving the Percus-Yevick equation for a hard-sphere fluid instead of using the step function [eq. (2.45)] of the SJC model.

2. $V_l^{ion}(r)$ is a non-local (l-dependent) bare-ion pseudopotential used to simulate the ion-electron interaction. The authors employed a parametrized potential form developed by Bachelet, *et al.* [66], which can fit atomic potentials for the entire periodic table.

3. $V_{Coul}(r)$ is the Coulomb potential denoting the interelectronic interaction and is given by [57]

$$V_{Coul}(r) \;=\; \int \frac{\sum_{i=1}^{N} |\psi_i(r')|^2}{|r - r'|}\, d^3r' \;, \tag{2.55}$$

where $\psi_i(r)$ is the wavefunction of the ith occupied state and N is the number of valence electrons.

4. $V_x(r)$ is a parameterized exchange potential, where two adjustable parameters were chosen to reproduce the best available gas-phase, low-energy electron scattering cross-section data.

5. $V_c(r)$ is a correlation potential that ensures that the short-ranged potential joins smoothly with the long-ranged polarization potential $-\alpha_{\mathrm{P}}\, e^2/(2\, r^4)$ at a certain crossing point.

Using the above interaction potential, Plenkiewicz, *et al.* calculated $V_0(\rho_{\mathrm{P}})$ for the rare gases [57–63] as well as for the molecular fluids methane [64] and silane [65]. These calculations tend to underestimate $V_0(\rho_{\mathrm{P}})$, with the calculated values differing from the experimental values by a minimum of 0.05 eV.

Iakubov, *et al.* [67–70] also modified the SJC model by changing the interaction potential. Their interaction potential was based on known atomic parameters and the radial distribution function in the liquid. These calculations tend to overestimate $V_0(\rho_{\rm P})$ by 0.1-0.5 eV, which represents an error of around 30%. Stampfli and Bennemann [71] improved the SJC model by avoiding the approximation used to calculate the polarization potential within the Wigner-Seitz sphere $V_P(r)$ [i.e., eq. (2.48)]. They used the full long-ranged polarization potential, $V_P(r) = -\alpha_{\rm P}\, e^2/(2\, r^4)$, and allowed the hard core radius r_h of the repulsive pseudopotential $V_a(r)$ [i.e., eq. (2.49)] to be an adjustable parameter. However, since $V_P(r)$ is no longer a constant, the Schrödinger equation can only be solved numerically. Moreover, they criticized the application of the WS model to fluids, since it assumes a rigid, primitive lattice structure for liquids. (All fluid density effects in the Wigner-Seitz model are incorporated by the simple contraction of the lattice at increasing density and decreasing Wigner-Seitz radius r_s.) Instead, Stampfli and Bennemann [71] proposed an alternative model that fixes the basic lattice in terms of the density and spatial arrangement of the solid perturber. Therefore, the reduced density in a dense fluid is handled by increasing the number of empty lattice sites within the crystalline structure of the solid. The quasi-free electron energy $V_0(\rho_{\rm P})$ is obtained as a weighted average of the energy of the electron interacting with occupied cells and unoccupied cells. This model underestimates $V_0(\rho_{\rm P})$ by a minimum of 0.01 eV (or 3%) for most of the density range.

Simon, *et al.* [72, 73] approached modeling $V_0(\rho_{\rm P})$ by considering the electron interaction in a dense perturber as a classical continuum percolation problem. The effective potential energy V_{eff} is defined as the sum of the potential energy V_p due

to the surrounding particles and the ground state kinetic energy K_g of the electron in the region of confinement. Since there is a distribution of occupied and vacant volume in a disordered fluid, all of these quantities are position dependent. For a given fluid density, one can construct the effective potential surface, or $V_{eff}(r)$, as a function of the spatial coordinates. Considering an electron with arbitrary energy E, the conducting (or allowed) spatial regions will be all points that satisfy $E > V_{eff}(r) \equiv V_p(r) + K_g(r)$. At lower energy E, electrons are confined in separated and impenetrable energy valleys in the potential energy surface. As the electron energy increases and reaches some threshold energy E_T, the allowed regions begin to percolate (forming macroscopic conduction paths). Thus, $E_T = V_0(\rho_{\mathrm{P}})$ for any given density in this model. To find E_T, the authors assumed that the minimum ratio of allowed volume to total volume for percolation was 0.032. These model calculations provide $V_0(\rho_{\mathrm{P}})$ with a density dependence similar to that measured experimentally. However, the minimum of $V_0(\rho_{\mathrm{P}})$ appears at higher densities for Ar, Kr and Xe. Moreover, $V_0(\rho_{\mathrm{P}})$ is underestimated by a minimum of 0.08 eV. One weak point of this model is the neglect of the perturber screening effect, as was pointed out by Lopez-Castillo, *et al.* [74].

Finally, more complex Monte Carlo and molecular dynamics calculations have also been performed to determine $V_0(\rho_{\mathrm{P}})$ in atomic perturbers. Lopez-Castillo, *et al.* [74] used path-integral molecular dynamics (PIMD) simulations to calculate $V_0(\rho_{\mathrm{P}})$ for argon at densities up to the triple-point density of 2.1 $\times 10^{22}$ cm^{-3}. In their algorithm [74], the path integral of a single quantum particle is replaced by the model classical system of a chain polymer with P beads. Each bead interacts with its two

nearest neighbors through constant harmonic forces $P\,m_e/(\beta^2\,\hbar^2)$ and with $(1/P)$th of the electron-fluid interaction potential $V_{el-F}(r)$. V_{el-F} is then given by

$$V_{el-F}(r, R_1, \ldots, R_N) \;=\; \sum_{i=1}^{N} V_{el-at}(|r - R_i|)\; f_{-}(|r - R_i|)\;, \tag{2.56}$$

where r is the electron position, R_i is the position of the ith atom, V_{el-at} is an electron-atom pseudopotential obtained from Li, Broughton and Allen [75], and the screening function $f_{-}(r)$ is a modified form of eq. (2.46). The electron-atom pseudopotential [75] was chosen because it is strongly repulsive at short electron/perturber distances, but goes over to the usual asymptotic polarization potential when the separation is larger than a cut-off radius r_c (which was chosen to be 4.27 au for argon). The screening function was modified in order to remove discontinuities at the cut-off radius. In addition, Lopez-Castillo, *et al.* [74] used the Lennard-Jones 6-12 potential to describe the atom-atom interaction in the fluid. They concluded that (i) the inclusion of screening is essential for reproducing the minimum in $V_0(\rho_{\rm P})$, (ii) the relaxation of the fluid during the electron/perturber interaction is negligible, (iii) $V_0(\rho_{\rm P})$ is weakly dependent on the degree of disorder of the fluid, and (iv) the convergence analysis $(P \to \infty)$ is important for obtaining accurate $V_0(\rho_{\rm P})$ at high densities.

Lopez-Castillo and Jay-Gerin [76] also provided a formalism for the study of $V_0(\rho_{\rm P})$ in simple fluids within the framework of multiple-scattering theory, which is important for understanding the behavior of $V_0(\rho_{\rm P})$ at low densities. Within first-order of the random-phase approximation, they expanded $V_0(\rho_{\rm P})$ to terms containing $\rho_{\rm P}^2$ with a parameter to gauge atom/atom interactions. (Under the assumption of a hard sphere interaction between perturbers, this coefficient is a constant.) This calculation agrees with the experimental data for argon up to argon densities of 1.6 $\times 10^{22}$ cm^{-3}, but

overestimates $V_0(\rho_P)$ at higher densities by up to 0.1 eV. If the perturber/perturber interactions are modeled using a Lennard-Jones 6-12 potential, the coefficient of the second-order term shows significant temperature dependence. However, experimental $V_0(\rho_P)$ data had not yet been obtained along different isotherms, but with the same perturber number density. We will show in this work that there is no temperature effect on $V_0(\rho_P)$, except near the critical temperature and density of the perturber.

Space, *et al.* [77] computed $V_0(\rho_P)$ for He, Ar and Xe using both the diffusion Monte Carlo (DMC) method and the fast Fourier transform (FFT) block Lanczos diagonalization (BLD) method. Their calculations involved the accurate determination of electron/He, electron/Ar and electron/Xe pseudopotentials, and confirmed the importance of many-body polarization interactions in modeling $V_0(\rho_P)$. Boltjes, *et al.* [78] used quantum molecular dynamics (QMD) to calculate $V_0(\rho_P)$ for He and Ar as a function of density under the assumption that the fluid structure is not disturbed by the quasi-free electron. Two different pseudopotentials were used for the electron-Ar interaction: (i) the Li, Broughton and Allen potential [75], and (ii) the modified Siska potential [79]. Both potentials provided calculational results close to the experiment up to 1.5 $\times 10^{22}$ cm^{-3}, but overestimated $V_0(\rho_P)$ at higher densities. These calculations also indicated that the induced dipole/induced dipole interaction in He was negligible, but that the interactions between induced dipoles in Ar should be considered when modeling high densities ($> 10^{22}$ cm^{-3}).

2.2.2 Previous experimental results

Section 2.2.1 detailed the modeling of dopant ionization energies and the energy of the quasi-free electron in dense perturbers. These theoretical models were de-

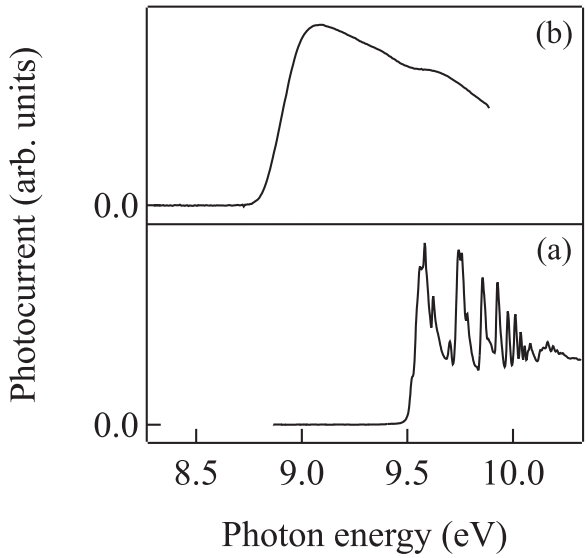

Figure 2.4: Photoionization spectra of (a) 0.10 mbar CH_3I and (b) 0.10 mbar CH_3I in dense argon ($\rho_P = 7.9 \times 10^{21}$ cm^{-3}). Note the energy shift in the photocurrent onset and the lack of autoionization structure in (b) due to the presence of high density argon.

veloped and tested against a handful of experimental results, which are discussed here. At high perturber densities, one cannot investigate the shift $\Delta(\rho_P)$ of the dopant ionization energy or high-n Rydberg states using absorption spectroscopy or standard photoionization spectroscopy because of the pressure broadening of the bound and autoionizing Rydberg states (cf. Fig. 2.4, for example). With this limitation in mind, several groups have investigated very dense media using photoconductivity techniques [48, 80–85, 89–91]. Most recently, Reininger, *et al.* [25] and our group [26, 42–47] have exploited field ionization of high-n dopant Rydberg states as a method for determining $\Delta(\rho_P)$ – and, subsequently, the quasi-free electron energy $V_0(\rho_P)$ – in various perturbers.

a. Photoinjection

The most commonly used direct approach to obtaining the quasi-free electron energy $V_0(\rho_P)$ is photoinjection [48, 80–85, 89–91], which involves injecting an electron from a metal (electrode) into a dense perturber. Since $V_0(\rho_P)$ is the energy required to take an electron from the vacuum into the perturbing fluid, the difference between the work function W_0 of the metal (electrode) in a vacuum and the work function $W_1(\rho_P)$ in a fluid corresponds directly to $V_0(\rho_P)$. In other words,

$$V_0(\rho_P) \;=\; W_1(\rho_P) \;-\; W_0 \;.$$

Thus, if one measures the photoemission spectrum of a metal in a vacuum and in a fluid separately, the difference in the threshold region can be used to determine $V_0(\rho_P)$.

Reininger, *et al.* measured the density dependence of $V_0(\rho_P)$ in Ar [80], Kr [81], and Xe [81] from the low density gas phase up to the density of the triple point liquid using photoinjection. These results are summarized in Fig. 2.5. One can clearly see that there exists a minimum in $V_0(\rho_P)$ for all three perturbers. However, one also notices that the scatter in the experimental data is quite high. Earlier photoinjection results by Allen and Schmidt [82] obtained in Ar at a density range of 1.0-1.8 $\times 10^{22}$ cm^{-3} show a similar scatter [cf. ($\triangle$) in Fig. 2.5a]. Similarly, Fig. 2.6 shows photoinjection results for $V_0(\rho_P)$ in the molecular perturbers methane and ethane. $V_0(\rho_P)$ in methane [85, 89] behaves in a manner similar to that of the attractive rare gases (cf. Fig. 2.6a). Ethane, on the other hand, showed significant differences [85, 90, 91]. The most striking of these differences is the positive value of $V_0(\rho_P)$ at ethane number

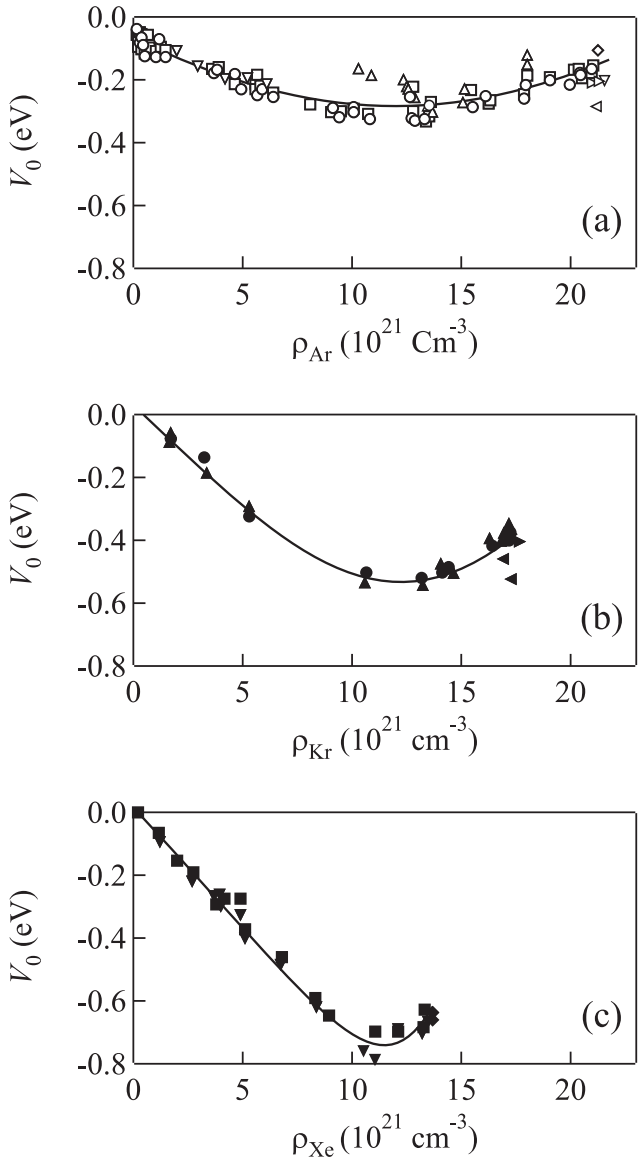

Figure 2.5: $V_0(\rho_P)$ in attractive rare gas fluids obtained from various photoinjection measurements, plotted as a function of perturber number density ρ_P. (a) P = Ar: (○, □) [80] with different evaluations, (△) [82], (◊) [83], (◁) [84], (▷) [85], and (▽) [48]. (b) P = Kr: (▲, ●) [81] with different evaluations, (◀) [83], and (▶) [85]. (c) P = Xe: (■, ▼) [81] with different evaluations, and (⧫) [83]. The lines are provided as a visual aid.

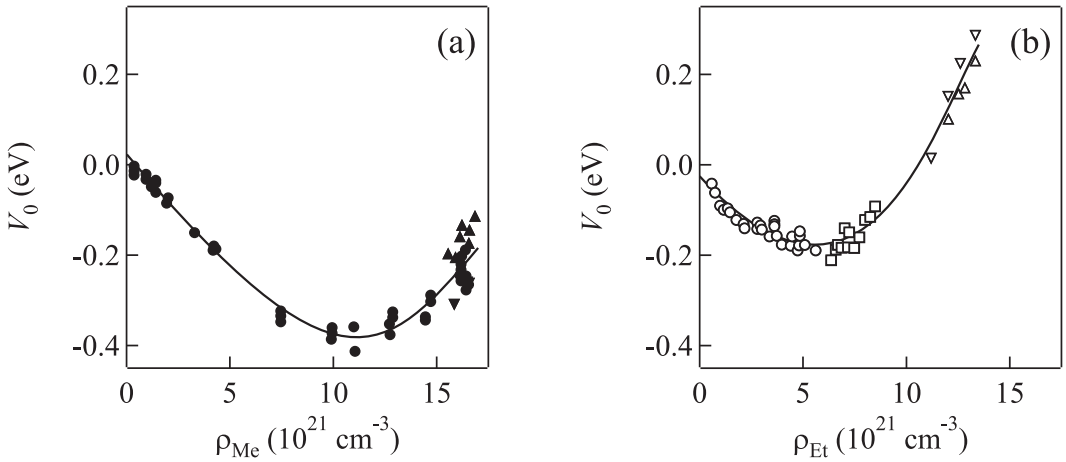

Figure 2.6: $V_0(\rho_P)$ in molecular fluids obtained from various photoinjection measurements, plotted as a function of perturber number density ρ_P. (a) P = methane: (•) [89] and (▲, ▼) [85] with different electrodes. (b) P = ethane: (○, □) [90] under different conditions, (▽) [91], and (△) [85]. The lines are provided as a visual aid.

densities greater than 10.3 $\times 10^{21}$ cm^{-3} (cf. Fig. 2.6b). The negative $V_0(\rho_P)$ illustrated in Fig. 2.5 and Fig. 2.6a for all densities reflects that the optical electron is quasi-free and, therefore, in the conduction band of the fluid. Electron localization within a fluid, on the other hand, occurs in repulsive systems and is indicated by a positive $V_0(\rho_P)$. Repulsive systems like He are not investigated in the present work due to their low critical- and triple-point temperatures. Thus, one possible explanation for the positive $V_0(\rho_P)$ in ethane is that ethane becomes a repulsive system at high densities and, therefore, that localized electron states exist in this system. We will offer an alternative explanation for this positive $V_0(\rho_P)$ in Chapter 5 of this work. The density dependence of $V_0(\rho_P)$ in larger non-polar molecular fluids has also been investigated using a variety of advanced photoinjection techniques [85, 92–96]. Holroyd, *et al.* also obtained $V_0(\rho_P)$ in a variety of hydrocarbon liquids [95, 96] at different temperatures. In addition, Holroyd and Russell found that in several hydrocarbons the apparent values of $V_0(\rho_P)$ changed when the photocathode materials [96] were varied. Simi-

lar temperature dependencies and electrode dependencies were observed in rare gas liquids, and in methane and ethane by Tauchert, *et al.* [85].

The photoinjection method contains two major problems. One can clearly see in Figs. 2.5 and 2.6 that the experimental results do not extrapolate to zero energy in the absence of a perturber (i.e., in a vacuum). This problem results from the formation of oxide layers on the metal surface of the electrode. These oxide layers form a barrier through which a photoemitted electron must tunnel, and the photoinjection energy of the oxide-contaminated metal electrode is therefore non-zero in the vacuum. The second problem is that the perturber interacts with the surface of the electrode and thereby changes the electronic structure of the electrode. This perturber/electrode interaction is dependent on the surface area and roughness of the electrode, the type of metal, the nature of the perturber and the number density of the perturber. These two factors cause the scatter of experimental data points in Figs. 2.5 and 2.6, as well as the discrepant results observed by Holroyd, *et al.* [96] and Tauchert, *et al.* [85]. Accurately correcting the experimental data for perturber/electrode interactions is difficult. Therefore, the development of another experimental method was necessary in order to investigate temperature effects and more detailed density effects on $V_0(\rho_{\mathrm{P}})$.

b. Field ionization

Since photoinjection is interpretationally problematic, Reininger and co-workers [4, 7, 27, 50–54, 97–99] developed a field ionization method to accurately obtain the shift $\Delta(\rho_{\mathrm{P}})$ of the dopant ionization energy, which leads to $V_0(\rho_{\mathrm{P}})$ indirectly through eq. (2.35) by subtracting the calculated $P_+(\rho_{\mathrm{P}})$ [i.e., eq. (2.41)]. For high-n atomic and molecular Rydberg states, the dopant core/optical electron potential is a Coulomb

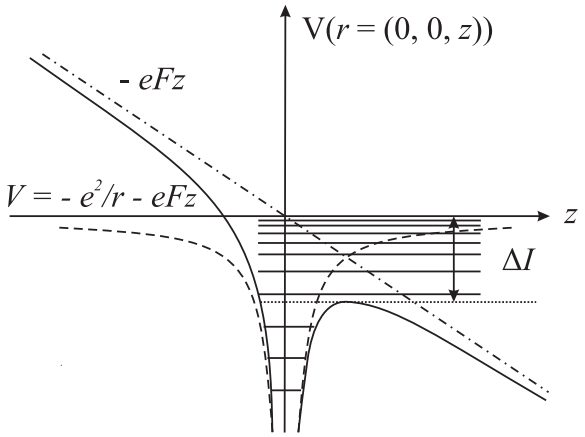

Figure 2.7: Field ionization of Rydberg states. (- - -) Coulomb potential ($-e^2/r$), (- · -) external electric field on z direction, (—— curve) core-electron potential under the electric field. Note ΔI is the lowering of the ionization limit.

potential (i.e., $-e^2/r$). When an external electric field F is applied, the angular momentum states are coupled. The effect of this coupling is to lower the ionization limit in comparison to the zero-field limit (cf. Fig. 2.7). For convenience, we will call the difference between the ionization limit in an electric field and the zero-field ionization limit ΔI. Thus, high-n Rydberg states with a binding energy less than ΔI will be ionized by the electric field.

By means of classical field ionization, the field-induced change in the ionization energy of hydrogen is given by $\Delta I = -2F^{1/2}$ [8]. In the field ionization of molecular Rydberg states, vibrational and rotational effects must be taken into consideration, and these effects lead to the classical field ionization limit being written as [4, 8]

$$\Delta I \;=\; -\,c_0\,F^{1/2}\,, \tag{2.57}$$

where c_0 is a positive constant.

Reininger and co-workers [4, 7, 27, 50–54, 97–99] used field ionization of high-n Rydberg states as a way to systematically obtain $\Delta(\rho_{\rm P})$. As mentioned previously,

experimentally obtaining $\Delta(\rho_P)$ with less scatter allows us to use eq. (2.35) with an accurate calculation of eq. (2.41). Fig. 2.8 summarizes $V_0(\rho_P)$ for the attractive rare gas fluids (i.e., Ar, Kr and Xe) obtained from the experimental $\Delta(\rho_P)$ using eq. (2.41) [4, 50, 52, 53, 98, 99]. (The details of the $P_+(\rho_P)$ calculations can be found in [4,50,52,53,98,99].) Clearly, these data follow the same trend as the photoinjection results shown in Fig. 2.5, but with much less scatter. Since the field ionization measurements are not affected by the formation of oxide layers and the surface structure of electrodes, these results are generally more reliable than those from photoinjection. However, temperature studies were not performed for any of the experimental data (i.e., solid markers) presented in Fig. 2.8. These data also do not extend to the very low density regime of $\leq 1 \times 10^{21}$ cm^{-3}. In the work presented here, we will investigate $V_0(\rho_P)$ in the attractive rare gases and selected molecular gases for various isotherms, including the critical isotherm, from low densities up to the density of the triple-point liquid. Since the field ionization technique requires that $V_0(\rho_P)$ be extracted from the experimentally determined $\Delta(\rho_P)$, we will show that the method of modeling $P_+(\rho_P)$ presented in eq. (2.41) yields a quasi-free electron energy that is independent of the dopant used to obtain the optical electron.

Fig. 2.8 also includes some of the theoretical approaches [56, 63, 71–74, 76–78] discussed in Section 2.2.1. The failure of the original SJC model [56] is clearly shown in comparison to the data for both Ar and Kr (cf. Fig. 2.8a and b) for all perturber densities. Better agreement between experiment and theory is achieved by the later, more complex calculations. However, most of the current calculations fit either the low density data well or the high density data well. None of the calculations fit the

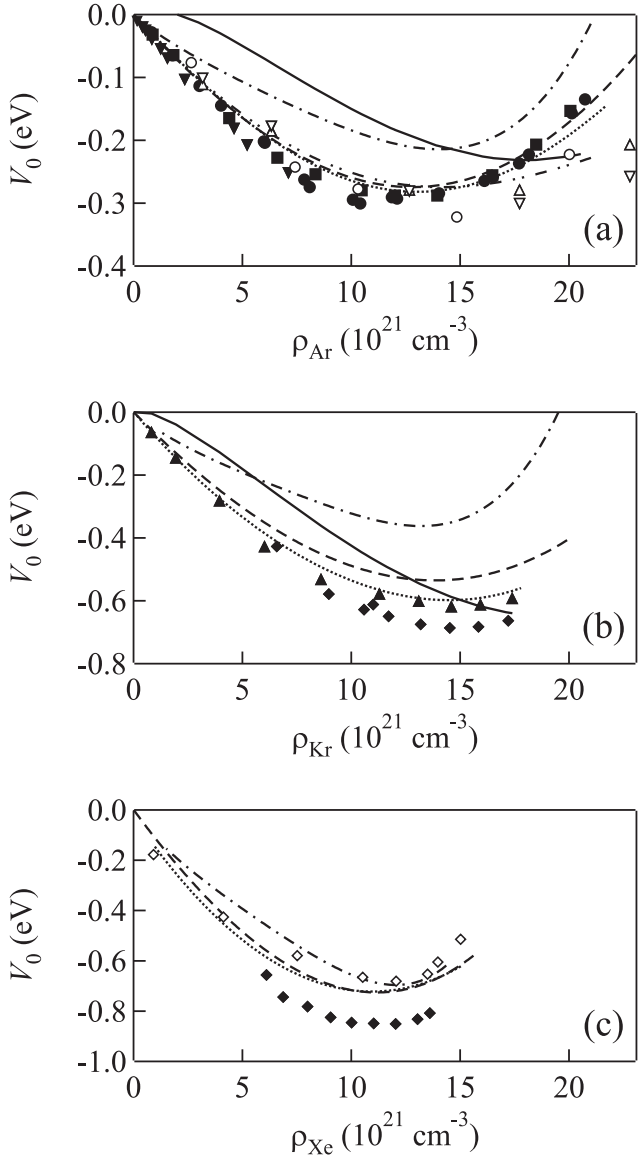

Figure 2.8: $V_0(\rho_P)$ obtained from field ionization of various dopants D plotted as a function of perturber P number density. (a) P = Ar. (●) D = H_2S [50]; (■) D = CH_3I [53]; and (▼) D = CH_3I [99]. (b) P = Kr. (▲) D = CH_3I [52] and (⧫) D = $(CH_3)_2S$ [98]. (c) P = Xe. (⧫) D = $(CH_3)_2S$ [98]. The lines and open markers represent calculations from the various theories presented in Section 2.2.1. (——) is calculated using the SJC model [56] [i.e., eq. (2.53)] with $r_h = 0.91$ Å for Ar and $r_h = 1.04$ Å for Kr. (· · ·) is obtained using a more accurate pseudopotential [63]. (- · -) is obtained by the classical continuum percolation approach [73] (originally fitted to photoinjection results). (- - -) is determined in the expanded lattice model where $V_P(r)$ is non-constant [71]. (- · · -) is calculated for Ar using a random-phase approximation within multiple scattering theory [76]. (△) and (▽) are calculated using quantum molecular dynamics for Ar [78]. (○) is $V_0(\rho_P)$ in Ar obtained by path integral molecular dynamics [74]. Finally, (◇) is determined for Xe with a mean-field many-body polarization potential [77].

entire density range with the same level of error. In general, the Wigner-Seitz models are superior to other methods in terms of accuracy and simplicity. We will show that a modification of the boundary conditions in the Wigner-Seitz model can reduce the difference between theory and experiment to within $\pm 0.5\%$ of experiment for all perturber densities and temperatures, including near the critical density and temperature. We will then expand this new model to selected molecular perturbers.

Chapter 3

Experiment

3.1 Experimental apparatus

The determination of $V_0(\rho_P)$ involves measuring dopant photoionization spectra in a dense fluid under different electric fields. These measurement require (i) a light source and monochromator with appropriate resolution (< 10 meV) over a large energy range, (ii) a sample cell that can withstand high pressures (up to 100 bar), (iii) a temperature control system that can stabilize the temperature of a sample to within ± 0.5°C over a broad range of temperatures (i.e., -191°C to 100°C), and (iv) a gas handling system for sample preparation.

The light was provided by the 1-m Aluminum Seya-Namioka monochromator (Al-Seya) on bending magnet 8 of the Aladdin electron storage ring at the University of Wisconsin Synchrotron Radiation Center (SRC). The Al-Seya beamline, which was decommissioned during Winter 2007, covered the energy range from 5 - 30 eV with a resolution of 0.9 Å, or ~ 8 meV in the spectral region of interest (i.e., 5 - 11 eV). The intensity of the monochromatic radiation was monitored and recorded by a nickel mesh placed perpendicular to the light path prior to the sample cell. The sample cell was placed in a ultra-high vacuum chamber (cf. Fig. 3.1) that was

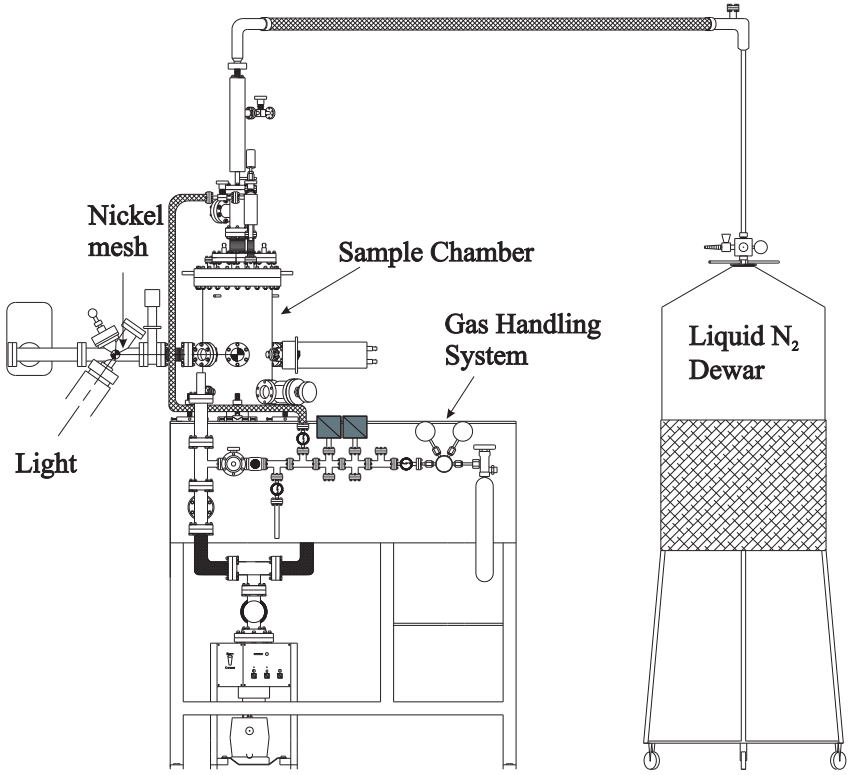

Figure 3.1: Schematic of the sample chamber used in all of the experiments presented here.

separated from the beamline by a pneumatic safety valve. The cell was aligned so that the monochromator focus was centered in the sample cell. The pressure in the sample chamber was maintained in the low 10^{-8} Torr range during experimental measurements by an ion pump attached to the bottom of the chamber. The safety valve was configured to close if the pressure in the sample chamber rose above the mid 10^{-8} Torr region. (We should note here that the base sample chamber pressure was maintained at high 10^{-9} Torr when not open to the monochromator.)

Two different copper sample cells [5] were used in these experiments: Cell 1 (cf. Fig. 3.2a) is equipped with entrance and exit MgF_2 windows and a pair of parallel plate electrodes (stainless steel, 3.0 mm spacing) oriented parallel to the incoming radiation and perpendicular to the windows. This orientation of electrodes and windows

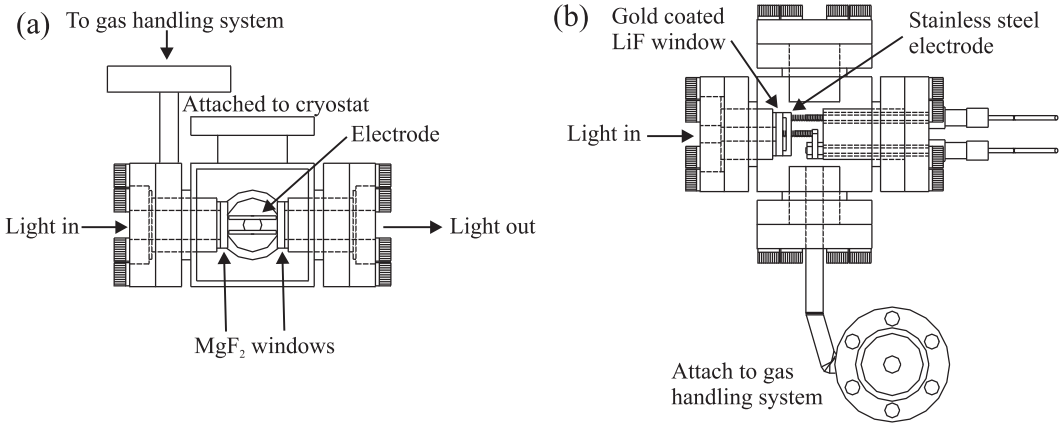

Figure 3.2: (a) Side view of cell 1. (b) Top view of cell 2. See text for discussion.

permits the simultaneous recording of photoionization and transmission spectra. The light path inside Cell 1 is 1.0 cm. Cell 2 (cf. Fig. 3.2b) is equipped with an entrance LiF window coated with a thin (7 nm) layer of gold to act as an electrode. The second electrode (stainless steel) is placed parallel to the window with a spacing of approximately 1.05 mm. Both cells were designed to withstand gas pressures up to 100 bar. All the experiments reported here were performed in Cell 1, except for selected data in ethane at non-critical temperatures and data obtained along the critical isotherm of ethane.

The temperature of the sample was controlled by attaching the sample cell to a cryostat that was simultaneously heated with a resistive heater and cooled by liquid nitrogen flow through the cryostat. The temperatures above and beneath the cell were measured with a Pt resistor and a silicon diode, respectively, and were regulated by a digital temperature controller (i.e., a Lakeshore 330 Autotuning Temperature Controller). The controller monitored the temperature of both sensors and adjusted the current flow through the resistive heater to bring both monitored temperatures close to the temperature set by the user. This system will hold the temperature to

within ±0.5°C of the set point for most samples after stabilization. Near the critical point of a fluid, small changes in temperature lead to large density swings. These density swings in the cell increase the difficulty of stabilizing the temperature by just adjusting the current flow through the heater. Therefore, for experimental data points taken near the critical point of the fluid, the temperature was also regulated by manually adjusting the liquid nitrogen flow. Using this technique, we were able to control the temperature to within ±0.2°C for these data points, which is crucial for maintaining constant density in the near critical point sample. The voltage applied to the cell electrodes was provided by a Bertan Series 225 High Voltage Power Supply. This power supply allows us to vary the voltage applied to the electrodes up to 5000 V, giving us a maximum electric field strength of 16,700 V/cm and 48,500 V/cm for Cell 1 and Cell 2, respectively.

3.2 Sample preparation

Fig. 3.3 shows a typical gas handling system setup. Before any sample is prepared, the system is baked to a base pressure of low 10^{-8} Torr or high 10^{-9} Torr. Once a suitable base pressure is achieved, a sample can be added to the sample cell. The preparation of any sample is performed in three steps: (1) adding the dopant; (2) adding the perturber; and (3) mixing the sample. These steps are detailed in [5]. Thus, we will present only a brief discussion of sample preparation.

1) Adding the dopant: The valve to the pump is closed, as are any valves to gas regulators connected to the perturber gas bottle. Valve V2 is opened slightly to allow the desired amount of the dopant into the gas handling system (GHS) and subsequently into the sample cell. Once the desired pressure (determined using the low

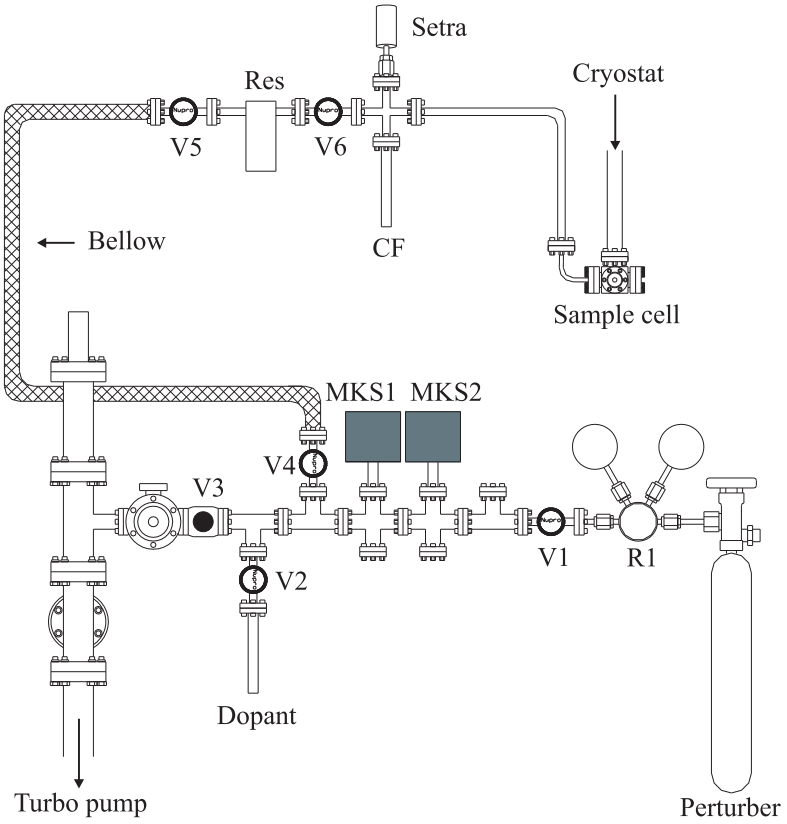

Figure 3.3: Schematic representation for a typical arrangement of the gas handling system. V1 - V6: valves; R1: dual stage regulator; MKS1: pressure manometer (maximum range: 10 mbar); MKS2: pressure manometer (maximum range: 1 bar); Res: reservoir; Setra: pressure manometer (maximum range: 200 bar); and CF: cold finger.

pressure gauges MKS1 and MKS2 that read to 10.00 mbar and 1.00 bar, respectively) is reached, both V2 and V6 are closed. The remaining dopant is removed from the GHS by opening the V3. The addition of the perturber is not begun until after the pressure in the GHS has returned to the low 10^{-7} Torr range to prevent contamination of the high purity perturber gas with the dopant. The time between dopant and perturber addition is usually 30 - 60 minutes, since our dopants tend to be liquids at room temperature and pressure and, therefore, are difficult to pump out of the vacuum system.

2) Adding the perturber: When the GHS has returned to a suitable pressure, the regulator R1 and the valve V1 are verified to be closed. The perturber bottle is opened briefly and then closed. The regulator is set to allow 30 psi on the low pressure side, which allows us to control the rate of gas flow into the GHS. The valve V1 can then be used to fill the GHS system to the desired amount of perturber gas up to a 1 bar limit. (The limit of 1 bar is due to the stainless steel bellows between V4 and V5.) Since all of our studies occur at medium and high density, our desired amount of perturber is usually above 1 bar. The opening of V6 decreases the total pressure to below 1 bar and, therefore, more perturber is added to bring the total pressure back to 1 bar before closing V1 and V6. At this point, all of the gas in the sample cell is collected into the cold finger (CF) with liquid N_2. Additional gas can be added to this initial sample in two different ways, namely, using the reservoir (Res) as a gas ballast volume or using the remaining GHS as the gas ballast volume. The Res ballast volume is approximately 3 times the volume of the sample cell region, while the GHS ballast volume is usually 10 times the volume of the sample cell region. The amount of gas needed to reach the desired pressure determines which method is chosen. To obtain a final pressure of 30 bar in the sample cell region, we would use the GHS as the ballast volume; whereas, if we wanted to add only 500 mbar, we would use the reservoir as the ballast volume. Adding perturber gas to the cell using a GHS fill is usually faster if one wants to start with a higher pressure sample. However, this procedure is risky since V3 can slip open during the process of collecting the gas into the cold finger. Thus, V3 and the pumping speed of the vacuum pump (which drops dramatically if V3 slips) must be monitored closely during a GHS fill procedure. The final pressure

of the sample is obtained by closing V6 and thawing the sample using a heat gun. The pressure is measured using the Setra pressure gauge, which is calibrated for the range 0 - 80.00 bar. If the sample is not at the desired final pressure, the sample is frozen with liquid N_2 and more perturber gas is added.

3) Mixing the sample: Steps 1 and 2 do not ensure a homogeneous mixing of the dopant and perturber, since the dopant is added before the perturber. Moreover, the perturber diffusion from the cold finger to the cell is slow. Thus, manual mixing of the dopant and perturber is necessary. This manual mixing is accomplished by collecting all of the sample into the cold finger using liquid N_2 and then releasing the sample back into the cell by warming the cold finger with a heat gun. This freeze-thaw process is repeated at least three times to guarantee homogeneous mixing. Then the temperature of the sample cell is adjusted to the desired temperature (or the temperature is allowed to stabilize) and the two photoionization spectra necessary for field ionization are obtained. The next sample is prepared by either adding additional perturber or by changing the temperature. Finally, we should note that the cold finger is at room temperature (if the critical temperature of the perturber is below room temperature). Thus, time must be allowed for the pressure of the sample to stabilize at the desired cell temperature.

The method discussed above is our standard way of preparing samples [26, 42–47] for perturbers having critical temperatures (T_c) below room temperature. However, for samples (e.g., ethane) with a critical temperature near or above room temperature, we must ensure that the temperature of the cold finger is higher than the critical temperature of the perturber. In fact, careful observation using ethane indicated

that a temperature gradient between the cold finger and the sample cell of 20 - 30°C should be maintained in order to ensure a homogeneous mixing of dopant and perturber in the sample cell. Because our system was not originally designed for this purpose, we modified the system by attaching resistive heat tape to CF and Res. This area of the GHS was wrapped with aluminum foil to insure uniform heating, and the temperature was monitored using a thermocouple on CF and a dial thermometer on Res. The heating of the GHS system, however, also mandated that more time be spent between samples to allow both the GHS and the sample cell to stabilize thermally. The final problem encountered when working with dense molecular gases, instead of dense atomic gases, is the molecular volume. The size of CF was chosen to minimize the amount of gas needed to prepare high pressure samples. However, the cold finger volume is too small to collect the amount of perturber necessary to achieve the desired final pressures for many of our samples. Therefore, we used Res as an additional cold finger. This requirement meant a three fold increase in the amount of perturber required to generate the same final sample pressure which, in turn, increased the cost of the experiment.

3.3 Dopant and Perturber information

The measurement of photoionization spectra in fluids at high perturber number densities (implying high pressures) necessitates the use of crystal windows in the sample cells which, in turn, have specific energy cut-offs because of light absorption. In these experiments, we use MgF_2 and LiF windows with energy cutoffs at 10.8 eV and 11.8 eV, respectively. Thus, the dopants chosen for these experiments must have Rydberg states and first ionization energies below 11.8 eV. Moreover, the dopants must

have sufficiently high vapor pressures to allow for their introduction into the gas phase system, and must possess an ionization energy in a spectral region where the perturbers are transparent. Finally, the dopant should not chemically react with the perturber during the spectroscopic measurements. With these limitations in mind, the dopants chosen were the following molecules: CH_3I, C_2H_5I, trimethylamine (TMA), N,N-dimethylaniline (DMAn) and triethylamine (TEA).

CH_3I, C_2H_5I, DMAn and TEA used in these experiments were purchased from Sigma-Aldrich. Since the amount of dopant used in sample preparation is relatively small (i.e., between 0.1 to 10 mbar), ultra-high purity dopants were not needed. Therefore, the dopants were used without further purification. The purities of each of these dopants, obtained from lot analysis provided by Sigma-Aldrich, were as follows: CH_3I, 99.45%; C_2H_5I, 99.1%; DMAn, 99.8% and TEA, 99.8%. All of these dopants, which are liquid at room temperature, were degassed by freezing with liquid nitrogen, then pumping using the turbo pump connected to the GHS, and then thawing using a heat gun. This process was repeated at least three times before the dopant was used. TMA, which is a gas at room temperature, was purchased from Matheson Gas Products at a purity of 99.5%. Perturber gases involved in this research were ultra-high purity gases purchased from Matheson Gas Products. The purity of each perturber is as follows: Ar, 99.9999%; Kr, 99.998%; Xe, 99.995%; CH_4, 99.999%; C_2H_6, 99.995%; and CF_4, 99.999%. The absence of contamination was verified by checking the photoionization and absorption spectra individually of each dopant and perturber. Trace impurities in some of the perturber gases were observed. However,

Table 3.1: The various equations of state (EOS) used to determine perturber number densities from the experimentally measured pressure and temperature, along with the references for the equation of state coefficients.

Perturber	Equation of state	Coefficients
Ar	Strobridge[1] EOS	[101]
Kr	Strobridge[1] EOS	[102]
Xe	Strobridge[1] EOS	[103]
CH_4	MBWR[2] EOS	[104]
C_2H_6	SW[3] EOS ($T < 205.15$ K and $T > 222.15$ K)	[106]
	MBWR[2] EOS (205.15 K $\geq T \geq$ 222.15 K)	[104]

[1]Strobridge equation of state [100].
[2]Modified Benedict-Webb-Rubin (MBWR) equation of state [104].
[3]Schmidt-Wagner (SW) equation of state [105].

these impurities did not interfere with the determination of dopant field ionization spectra at any perturber number density.

The number density of the perturber is calculated from an accurate equation of state using the pressure of the sample and the recorded temperature (obtained at the start and end of each field ionization scan). Because a myriad of equations of state (EOS) exists for the perturbers investigated in this work, the EOS and coefficients were chosen by determining the error in the density calculated from the EOS in comparison with published experimental thermodynamic data for each gas. The selected EOS had to give an error within $\pm 0.2\%$ of the density over the entire density range (i.e., low density to the density of the triple-point liquid). Table 3.1 lists the equations of state along with the reference containing the coefficients for each of the perturbers investigated. Since equations of state normally express the pressure as a function of density and temperature, the density was determined using a standard bisection method for root finding. Once an equation of state is selected, a $p - \rho - T$

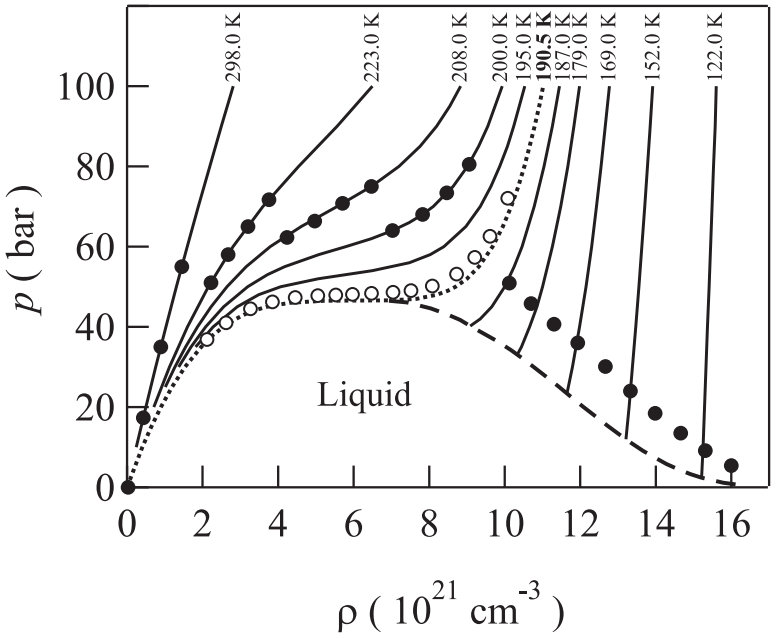

Figure 3.4: $p - \rho$ Phase diagram of CH_4 determined from the modified Benedict-Webb-Rubin equation of state [104] showing several non-critical isotherms (—), the critical isotherm ($\cdot\cdot\cdot$), and the vapor pressure curve (- - -). (•) present typical thermodynamic conditions for obtaining non-critical experimental data, while (○) indicate the thermodynamic conditions for the experimental data obtained near the critical point.

phase diagram is constructed and used to determine isotherms and temperatures for various data points. Fig. 3.4 shows the $p - \rho - T$ phase diagram of CH_4 with the thermodynamics conditions for various experimental points shown as (•). Since temperature stabilization is the most time consuming process, photoionization spectra were obtained for various perturber number densities along a single isotherm in the supercritical fluid region. The slope of the isotherms steepens for temperatures below the critical temperature. Therefore, in this region the temperature must be varied in order to change the density of the sample. In order to prevent gas condensation in the cell, which can cause a crack in the crystal window, the perturber pressure for these samples was always maintained at ≥ 3.0 bar above the perturber vapor pressure.

3.4 Data acquisition and field ionization correction

The monochromator was controlled by LabView software written by SRC staff. This software steps the grating to the desired wavelength, then pauses to read the picoammeters (Keithley 486, used as detectors in all experiments) before moving to the next wavelength. The picoammeters detect the photoemission current from the nickel mesh (cf. Fig. 3.1) and read the current collected at the electrodes in the sample cell (cf. Fig. 3.2). The monochromator control software creates a data file that contains the wavelength, energy, current stored in the storage ring, and data from all picoammeters for each point in the scan. These data files are then transferred to a separate computer for additional analysis.

Since the intensity of the synchrotron radiation decays over time, all photoionization spectra were normalized by the photoemission current from the Ni mesh. A field ionization spectrum is obtained by subtracting dopant photoionization spectra measured at two different electric fields to detect the high-n Rydberg states that are field ionized by the high field F_H, but not by the low field F_L. However, the F_L and F_H necessary to obtain the best field ionization spectra are very system dependent and, therefore, can only be determined empirically by measuring photoionization spectra at several different fields and at several perturber number densities. Once F_L and F_H are optimized for the system, a field ionization spectrum is obtained by subtracting a photoionization spectrum measured at F_L from a spectrum measured at F_H after intensity normalization (necessary to remove the effects of secondary ionization [4]). For example, the intensity normalized photoionization spectra of neat CH_3I measured at various electric field strengths are plotted as a function of photon energy in Fig. 3.5a.

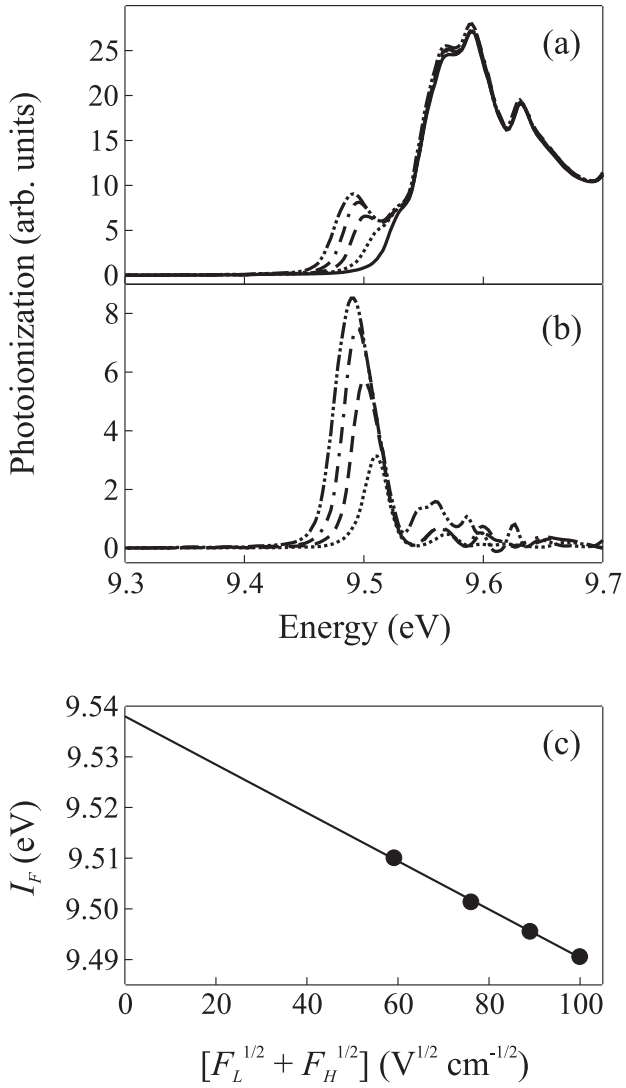

Figure 3.5: Field ionization study of 0.10 mbar CH_3I. (a) Photoionization spectra at (—) 333 V/cm, (···) 1667 V/cm, (- - -) 3333 V/cm, (- · -) 5000 V/cm, and (- ·· -) 6667 V/cm after intensity normalization, necessary to correct for secondary ionization. (b) Field ionization spectra obtained with $F_L = 333$ V/cm and with various F_H [see (a)]. (c) The energy I_F of the field ionization peak plotted as a function of the square root of the electric fields. See text for discussion.

Table 3.2: The first ionization energy $I_0(\rho_P)$ and the field ionization constant c_0 for all the dopants involved in this research.

Dopant	(eV) $I_0(\rho_P)$	(eV cm$^{1/2}$ V$^{-1/2}$) c_0
CH_3I	9.538 ± 0.005	$4.3 \pm 0.1 \times 10^{-4}$
C_2H_5I	9.349 ± 0.006	$3.0 \pm 0.5 \times 10^{-4}$
TMA	8.370 ± 0.008	$2.8 \pm 0.2 \times 10^{-4}$
TEA	7.833 ± 0.015	$4.9 \pm 0.3 \times 10^{-4}$
DMAn	7.450 ± 0.010	$5.1 \pm 0.8 \times 10^{-5}$

These spectra clearly show the changes in the photoionization spectra as a function of electric field. Since the field ionization spectrum depends on the field ionization of high-n Rydberg states, the variation in F_H leads to a characteristic shift in the energetic position of the field ionization peak (cf. Fig. 3.5b). By plotting this shift as a function of the square root of the electric field (cf. Fig. 3.5c), one can extrapolate the zero-field energy position of the ionization energy $I_0(\rho_P)$ using [42]

$$I_0(\rho_P) \;=\; I_F(\rho_P) \;+\; c_0 \left(\sqrt{F_L} \;+\; \sqrt{F_H} \right) , \tag{3.1}$$

where $I_F(\rho_P)$ is the dopant ionization energy perturbed by the electric field and by the dense gas, and c_0 is a dopant-dependent, perturber-independent positive constant that is empirically determined. Table 3.2 lists $I_0(\rho_P)$ and c_0 obtained from fitting the energy of several field ionization spectra for the neat dopants to eq. (3.1).

To remove any possible normalization errors, the photoionization spectra are intensity normalized in three different energy regions. This gives three different field ionization spectra, each of which is modeled with a nonlinear least-squares analysis using a Gaussian fit function. Since the field ionization spectra can be asymmetric,

three separate nonlinear Gaussian fits are performed. The energy of any field ionization peak [i.e., $I_{\rm F}(\rho_{\rm P})$] is, therefore, calculated from the average of the nine energy values determined from the three individual Gaussian fits on each of the three field ionization spectra. In this way, scatter in $I_{\rm F}(\rho_{\rm P})$ between different densities is greatly reduced. Once $I_{\rm F}(\rho_{\rm P})$ is obtained from the experimental data, eq. (3.1) and the data in Table 3.2 are used to calculate $I_0(\rho_{\rm P})$. The perturber dependent shift $\Delta(\rho_{\rm P})$ of the dopant ionization energy is then obtained from [42]

$$\Delta(\rho_{\rm P}) \;=\; I_0(\rho_{\rm P}) \;-\; I_g \;, \tag{3.2}$$

where I_g is the gas phase dopant ionization energy.

Chapter 4

Quasi-free electron energy $V_0(\rho_P)$ in rare gases

In this chapter, we first present new measurements of the perturber induced shift $\Delta(\rho_P)$ of the CH_3I ionization energy in low density Ar and Kr [26]. The temperature dependence observed in these data indicates the failure of the Fermi-Alekseev-Sobel'man model even at low perturber number densities. $V_0(\rho_P)$ data obtained using field ionization in all the attractive rare gases (i.e., Ar, Kr and Xe) are then presented as a function of perturber number density up to the density of the triple point liquid, both at non-critical temperatures and along the critical isotherm [42–47]. The local Wigner-Seitz model developed by our group is explained and used to model all data presented here. This model is shown to predict accurately the temperature dependence of $\Delta(\rho_P)$ at low perturber densities, as well as the dramatic change in $V_0(\rho_P)$ observed near the critical density and temperature of the perturber.

4.1 Experimental results

4.1.1 $\Delta(\rho_P)$ in low density Ar and Kr [26]

Field ionization of CH_3I high-n Rydberg states was performed in the low to medium density regime (i.e., $\rho_P \leq 3 \times 10^{21}$ cm^{-3}) for the perturbers argon and krypton, with

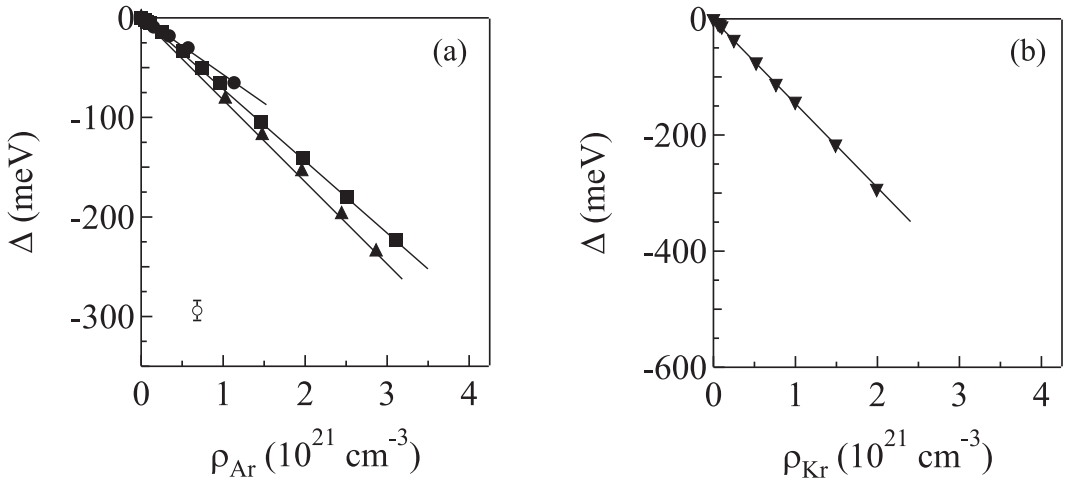

Figure 4.1: The perturber induced shift $\Delta(\rho_P)$ of the CH_3I ionization energy in (a) argon and (b) krypton plotted as a function of perturber number density ρ_P. (•, ▼) 25°C, (■) -60°C, and (▲) -114°C. The open marker is provided to show the experimental error. The lines are provided as a visual aid.

$F_L = 830 - 2,500$ V cm^{-1} and $F_H = 2,500 - 6,700$ V cm^{-1}. Fig. 4.1a presents the argon induced shift $\Delta(\rho_{Ar})$ of the CH_3I ionization energy plotted as a function of Ar number density at three different temperatures (i.e., 25°C, -60°C, and -114°C). These data show that $|\Delta(\rho_P)|$ increases as the temperature decreases. While the original low density Fermi model [15][i.e., eq. (2.15)] and the Al-Omari-Reininger-Huber model [27][i.e., eq. (2.34)] imply no temperature dependence, the Alekseev-Sobel'man model [6, 22][i.e., eq. (2.26)] predicts a decrease in $|\Delta(\rho_P)|$ as the temperature decreases, since the average thermal velocity v decreases with decreasing temperature. One can only model these new data by changing the electron scattering length A, which is unacceptable and indicates the failure of all these low density models. Fig. 4.1b presents new measurements of the krypton induced shift $\Delta(\rho_{Kr})$ of the CH_3I ionization energy (solid markers) plotted as a function of Kr number density at 25°C.

4.1.2 $V_0(\rho_P)$ in Ar, Kr and Xe

While experimental data exist for the energy of a quasi-free electron $V_0(\rho_P)$ in attractive rare gas perturbers (cf. Figs. 2.5 and 2.8), our group chose to obtain new experimental data along specific isotherms in order to evaluate temperature effects. Fig. 4.2 summarizes the perturber induced shift of the dopant ionization energy $\Delta(\rho_P)$ of CH_3I [42, 43, 45] and C_2H_5I [42, 44, 45] in dense Ar and Kr, and of N,N-dimethylaniline [46] and trimethylamine [46] in dense Xe, plotted as a function of perturber number density ρ_P. The data represented by the solid markers in Fig. 4.2a and b were taken along the non-critical isotherms -114.8°C and -117.6°C for Ar densities of (3.1 - 11.6) $\times 10^{21}$ cm^{-3}. The solid markers at higher Ar number densities required that the temperature be adjusted, since the density does not vary much with pressure for a perturber pressure of under 80 bar when the temperture is less than the critical temperature T_c. The data point at the highest argon density was obtained at a temperature of -181°C, which is near the triple point temperature of -189°C. The open markers in Figs. 4.2a and b were obtained on the isotherm of -121.5°C, which is near the argon critical temperature of -122.3°C. Similarly, the data represented by solid markers in Fig. 4.2c and d were obtained along the non-critical isotherms -57.1°C and -60.0°C for Kr densities of (2.0 - 9.7) $\times 10^{21}$ cm^{-3} as well as at other temperatures for the higher densities. (The data point at the highest krypton density was acquired at a temperature of -155°C, which is near the triple point temperature of -157°C.) The open markers in Fig. 4.2c and d were acquired along the isotherm of -63.3°C, which is near the krypton critical temperature of -63.7°C. In addition, the xenon induced shift of the dopant ionization energy at non-critical temperatures

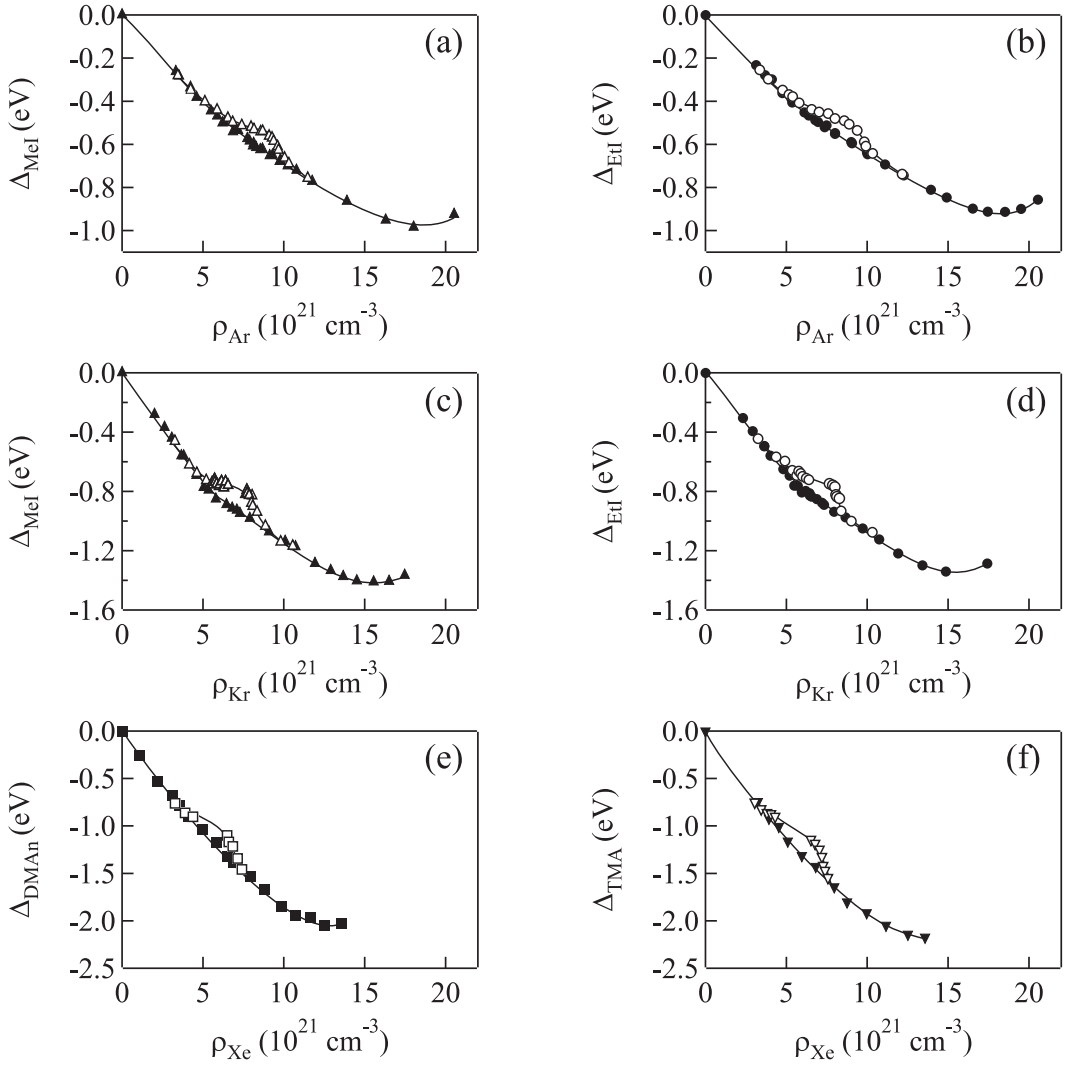

Figure 4.2: The perturber induced shift $\Delta(\rho_P)$ of the dopant (D) ionization energy in Ar (a and b), Kr (c and d), and Xe (e and f) plotted as a function of perturber number density ρ_P at non-critical temperatures (solid markers) and on an isotherm near the critical isotherm of the perturber (open markers). (▲ [42], △ [43, 45]) D = CH_3I, (● [42], ○ [44, 45]) D = C_2H_5I, (■ [46], □ [46]) D = N,N-dimethylaniline, and (▼ [46], ▽ [46]) D = trimethylamine. The lines are provided as a visual aid.

(cf. solid markers in Figs. 4.2e and f) were obtained along the non-critical isotherms of 19.8°C for Xe densities of (0.5 - 6.3) $\times 10^{21}$ cm^{-3} and 18.0°C for Xe densities of (6.4 - 7.0) $\times 10^{21}$ cm^{-3}, as well as at other temperatures for the higher densities. The data for the highest xenon density was obtained at a temperature of -109°C, which is close to the triple point temperature of -111°C. The open markers in Figs. 4.2e and f were acquired along an isotherm of 17.0°C, which is near the xenon critical temperature of 16.5°C.

The total error range for any experimental point is given by a sum of the field correction error, the goodness-of-fit error (for fitting a field ionization spectrum to a Gaussian line shape), and the error arising from the energy uncertainty due to the resolution of the monochromator (i.e., ± 4 meV). For measurements at non-critical temperatures, this total error averages to ± 0.015 eV for CH_3I and trimethylamine (TMA) and ± 0.020 eV for C_2H_5I and N,N-dimethylaniline (DMAn). For measurements along the critical isotherm of the perturber, this total error averages to ± 0.020 eV for CH_3I, ± 0.025 eV for C_2H_5I and TMA, and ± 0.030 eV for DMAn. We should note that the larger experimental error at the critical temperature arises from the inability to maintain the temperature and pressure to the high stability needed to minimize density fluctuations completely. The increased density fluctuations in turn increase the noise in the photoionization measurements and, therefore, in the field ionization spectra. The lack of data points in the xenon density range $(0.5 - 3.5) \times 10^{21}$ cm^{-3} with the dopant TMA (cf. Fig. 4.2f) is due to the saturated absorption of the xenon 6s Rydberg state at high xenon number density in the same spectral region as the ionization energy of TMA. The narrowness of the phase diagram in the sad-

dle region near the critical density of krypton and xenon, near the critical isotherm, prohibited the measurement of photoionization spectra in the krypton density range $(6.5 - 7.6) \times 10^{21}$ cm $^{-3}$ and the xenon density range $(4.5 - 6.5) \times 10^{21}$ cm^{-3}.

The data in Fig. 4.2 show a clear decrease in $|\Delta(\rho_P)|$ near the perturber critical density (i.e., $\rho_c = 8.0 \times 10^{21}$ cm^{-3} for Ar, $\rho_c = 6.6 \times 10^{21}$ cm^{-3} for Kr, and $\rho_c = 5.0 \times 10^{21}$ cm^{-3} for Xe). Also, a careful perusal of Fig. 4.2 shows that $\Delta(\rho_P)$ for different dopants in the same perturber differ slightly from each other. In order to determine if these differences arise from the quasi-free electron energy $V_0(\rho_P)$, the average ion/perturber polarization energy $P_+(\rho_P)$ must be evaluated and subtracted from $\Delta(\rho_P)$. We chose to calculate $P_+(\rho_P)$ using eqs. (2.36) - (2.41) with the radial distribution functions $g_{PP}(r)$ and $g_{PD}(r)$ calculated from a coupled homogeneous Percus-Yevick model, given by [42, 107]

$$g_{ij}(r) \;=\; r^{-1}\, \mathrm{e}^{-\beta U_{ij}(r)}\, Y_{ij}(r), \tag{4.1}$$

where i = P or D, j = P or D, U_{ij} is the intermolecular potential between species i and j, and

$$Y_{ij}(r) \;=\; \int_0^r dt\, \frac{dY_{ij}(t)}{dt}\,, \tag{4.2}$$

with

$$\begin{aligned} \frac{d}{dr} Y_{ij}(r) \;&=\; 1 \;+\; 2\,\pi \sum_k \rho_k \int_0^\infty dt\, \left(\mathrm{e}^{-\beta U_{kj}(t)} \;-\; 1\right)\, Y_{kj}(t) \\ &\quad \times \left[\mathrm{e}^{-\beta U_{ik}(r+t)}\, Y_{ik}(r+t) \;-\; \frac{r-t}{|r-t|}\, \mathrm{e}^{-\beta U_{ik}(|r-t|)}\, Y_{ik}(|r-t|) \;-\; 2\,t\right], \end{aligned} \tag{4.3}$$

where ρ_k is the number density of species k = P or D. It is important to note that when $\rho_D \ll \rho_P$, the four coupled equations represented by eq. (4.3) reduce to two coupled equations for g_{PP} and g_{PD}, and g_{PP} is independent of g_{PD}.

For these calculations, the perturber/perturber intermolecular potential was chosen to be a Lennard-Jones 6-12 potential,

$$U_{\rm PP}(r) \;=\; 4\,\varepsilon_{\rm PP}\,\left[\left(\frac{\sigma_{\rm PP}}{r}\right)^{12} - \left(\frac{\sigma_{\rm PP}}{r}\right)^{6}\right]\,, \tag{4.4}$$

where $\varepsilon_{\rm PP}$ is the well-depth for the perturber/perturber interaction, and $\sigma_{\rm PP}$ is the perturber collision parameter. The dopant/perturber intermolecular potential was a modified Stockmeyer potential with the form [108]

$$U_{\rm PD}(r) \;=\; 4\,\varepsilon_{\rm PD}\,\left[\left(\frac{\sigma_{\rm PD}}{r}\right)^{12} - \left(\frac{\sigma_{\rm PD}}{r}\right)^{6}\right] - \frac{1}{r^6}\,\alpha_{\rm P}\,\mu_{\rm D}^2\,, \tag{4.5}$$

where $\varepsilon_{\rm PD}$ is the well-depth for the dopant/perturber interaction, $\sigma_{\rm PD}$ is the dopant/perturber collision parameter, $\alpha_{\rm P}$ is the perturber polarizability, and $\mu_{\rm D}$ is the dipole moment of the dopant. (The modified Stockmeyer potential includes orientational effects via an angle average that presumes the free rotation of the polar dopants.) The determination of $\varepsilon_{\rm PD}$ and $\sigma_{\rm PD}$ begins with the calculation of $\varepsilon_{\rm DD}$ and $\sigma_{\rm DD}$ for each dopant from the dopant critical point information using

$$\frac{\varepsilon_{\rm DD}}{k_B} \;=\; \frac{T_{\rm c}}{T_{\rm c}^*}\,, \qquad \sigma_{\rm DD} \;=\; \left(\frac{\varepsilon_{\rm DD}\,p_{\rm c}^*}{p_{\rm c}}\right)^{1/3}\,, \tag{4.6}$$

where $T_{\rm c}^* = 1.312$ and $p_{\rm c}^* = 0.1279$ [109]. These parameters were then combined with the perturber/perturber intermolecular potential parameters using the Sikora combining rule [110]

$$\begin{aligned} \varepsilon_{\rm PD} \;&=\; \sqrt{\varepsilon_{\rm PP}\,\varepsilon_{\rm DD}}\;\frac{4\,I}{(1\,+\,I)^2}\;\frac{2^{13}\,V^{1/2}}{(1\,+\,V^{1/13})^{13}}\,, \\ \sigma_{\rm PD} \;&=\; 2^{-13/12}\,\left(\sigma_{\rm PP}^{12/13}\,+\,\sigma_{\rm DD}^{12/13}\right)^{13/12}\,, \end{aligned} \tag{4.7}$$

Table 4.1: Dopant and perturber thermodynamic information used to obtain Lennard-Jones potentials and to calculate radial distribution functions [42, 46]. All data are taken from CRC Handbook of Chemistry and Physics, 84th ed., D. R. Lide, ed. (CRC Press, 2004).

	($Å^3$) α	(D) μ	(K) T_c	(bar) p_c
Ar	1.6411	0	150.86	48.98
Kr	2.4844	0	209.46	55.20
Xe	4.044	0	289.74	58.42
CH_3I	7.97	1.641	528	65.9
C_2H_5I	10.0	1.976	554	47.0
TMA	8.15	0.612	433	40.8
DMAn	16.2	1.68	688	36.0

with

$$I = \frac{I_D}{I_P}, \qquad V = \frac{\varepsilon_{DD}\,\sigma_{DD}^{12}}{\varepsilon_{PP}\,\sigma_{PP}^{12}} \tag{4.8}$$

where I_D and I_P are the first ionization energies of dopant and perturber, respectively. Finally, eq. (4.5) is rewritten in the Lennard-Jones form

$$U_{PD}(r) = 4\,\varepsilon\,\left[\left(\frac{\sigma}{r}\right)^{12} - \left(\frac{\sigma}{r}\right)^{6}\right], \tag{4.9}$$

with

$$\varepsilon = \varepsilon_{PD}\left[1 + \frac{\alpha_P\,\mu_D^2}{4\,\varepsilon_{PD}\,\sigma_{PD}^6}\right]^2, \qquad \sigma = \sigma_{PD}\left[1 + \frac{\alpha_P\,\mu_D^2}{4\,\varepsilon_{PD}\,\sigma_{PD}^6}\right]^{-1/6}. \tag{4.10}$$

The information necessary to obtain the intermolecular potential parameters is given in Table 4.1, and the intermolecular potential parameters used in all of the calculations presented here are given in Table 4.2. We should note that small adjustments ($< \pm 5\%$) were made to the TMA/Xe and DMAn/Xe intermolecular potential parameters to remove all dopant dependence from $V_0(\rho_{Xe})$.

Table 4.2: Lennard-Jones parameters used in calculating the radial distribution functions (i.e., eqs. (4.1)-(4.3) of text) and the average polarization energies (i.e., eq. (2.41) of text) for attractive rare gas perturbers [42, 46].

	(Å) σ_{ij}	(K) ε_{ij}/k_B	(Å) σ^1	(K) $\varepsilon/k_B{}^1$
Ar-Ar	3.409	119.5		
Kr-Kr	3.591	172.7		
Xe-Xe	4.055	229.0		
CH_3I-CH_3I	4.761	402.4		
C_2H_5I-C_2H_5I	5.413	422.3		
TMA-TMA	5.227	330.0		
DMAn-DMAn	6.360	524.4		
CH_3I-Ar	4.081	158.8	4.074	162.2
C_2H_5I-Ar	4.402	135.1	4.394	139.1
CH_3I-Kr	4.173	214.1	4.166	218.6
C_2H_5I-Kr	4.495	187.8	4.487	191.8
TMA-Xe[2]	4.431	222.5	4.430	223.0
DMAn-Xe[2]	4.954	242.7	4.950	245.0

[1]From eq. (4.9) of text.
[2]Small adjustments ($< \pm 5\%$) were made to these parameters.

The average ion/perturber polarization energies $P_+(\rho_P)$ for CH_3I and C_2H_5I in Ar and in Kr as well as for DMAn and TMA in Xe, calculated from eq. (2.41), are shown as a function of perturber number density ρ_P in Figs. 4.3a-f. $V_0(\rho_P)$, which is extracted from [3, 26, 42–47]

$$V_0(\rho_P) \;=\; \Delta(\rho_P) \;-\; P_+(\rho_P)\;, \tag{4.11}$$

is presented in Fig. 4.4 as a function of ρ_P.

Clearly, $V_0(\rho_P)$ extracted from eq. (4.11) for the non-critical temperature data (cf. solid markers in Fig. 4.4) is similar to that previously reported from earlier field ionization measurements (cf. Fig. 2.8) and from photoconduction measurements (cf.

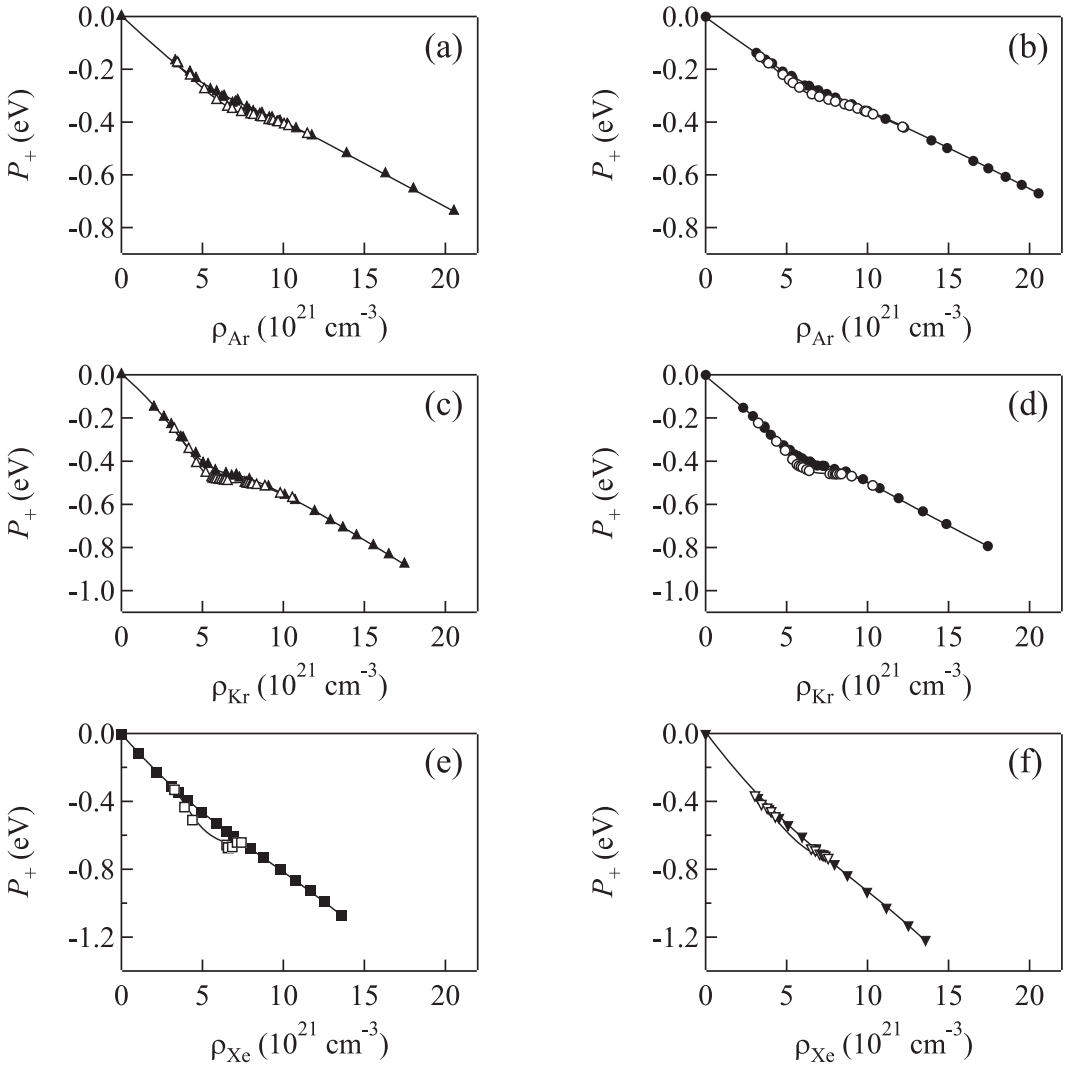

Figure 4.3: The average ion/perturber polarization energy $P_+(\rho_P)$ in Ar (a and b), Kr (c and d), and Xe (e and f), calculated from eq. (2.41) using the parameters in Table 4.2, plotted as a function of perturber number density ρ_P at non-critical temperatures (solid markers) and on an isotherm near the critical isotherm of the perturber (open markers). (▲ [42], △ [43,45]) D = CH_3I, (● [42], ○ [44,45]) D = C_2H_5I, (■ [46], □ [46]) D = N,N-dimethylaniline, and (▼ [46], ▽ [46]) D = trimethylamine. The lines are provided as a visual aid.

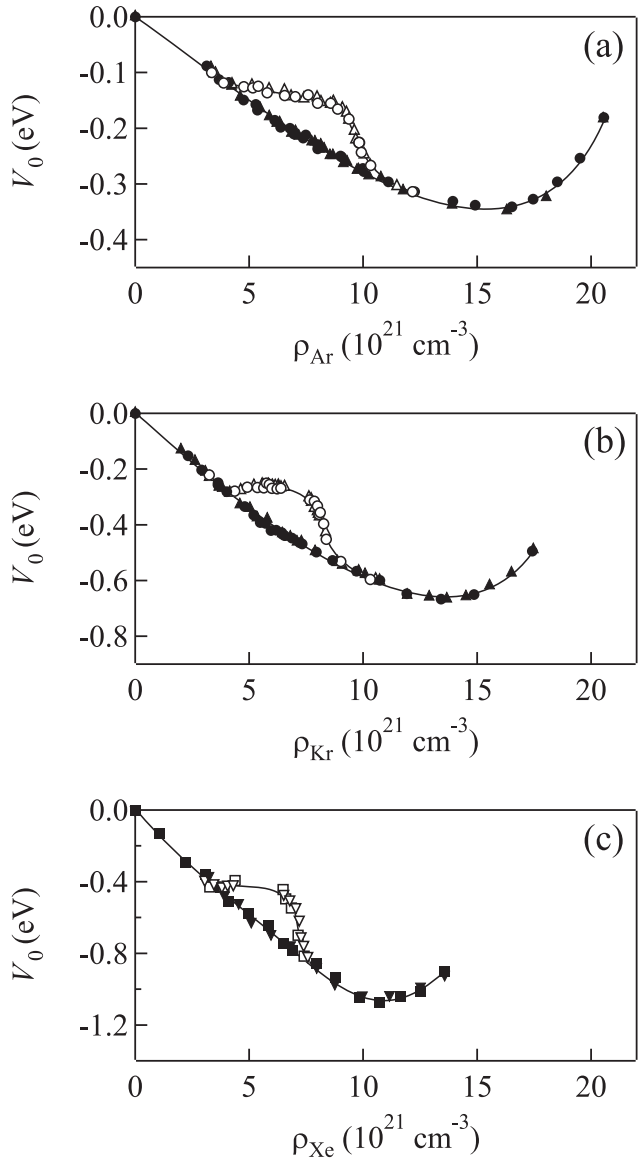

Figure 4.4: The quasi-free electron energy $V_0(\rho_P)$ for (a) Ar [42–44], (b) Kr [42,45] and (c) Xe [46] at non-critical temperatures (solid markers) and on an isotherm near the critical isotherm of the perturber (open markers), extracted from eq. (4.11), plotted as a function of perturber number density ρ_P. (▲ [42], △ [43, 45]) represent data extracted from CH_3I field ionization, (● [42], ○ [44,45]) are data obtained from C_2H_5I field ionization, (■ [46], □ [46]) are data determined from N, N-dimethylaniline field ionization, and (▼ [46], ▽ [46]) represent data from trimethylamine field ionization. The lines are provided as a visual aid.

Fig. 2.5). The small differences between the data of Fig. 2.8 and those of Fig. 4.4 can be attributed to the change in the average ion/perturber polarization energies because of the choice of intermolecular potentials. $V_0(\rho_P)$ also shows little or no temperature dependence along non-critical isotherms. Thus, the temperature variation in $\Delta(\rho_P)$ at low perturber number densities (cf. Fig. 4.1) must be caused by a temperature dependence in $P_+(\rho_P)$. However, $V_0(\rho_P)$ does vary considerably near the critical point of the perturber. This variation may well have a bearing on the changes in product distribution and reactivity [1,2] observed in chemical reactions conducted in certain supercritical fluids. In addition, $V_0(\rho_P)$ at non-critical temperatures and that along the critical isotherm both show no dopant dependence. Therefore, the slight dopant dependence of $\Delta(\rho_P)$ (cf. Fig. 4.2) is caused by the variation in the average ion/perturber polarization energies $P_+(\rho_P)$.

4.2 Discussion

4.2.1 Local Wigner-Seitz model

Since all previous low density models fail to predict the temperature dependence in the low density $\Delta(\rho_P)$ data reported in Fig. 4.1, and since the striking critical point effect seen in Figs. 4.2 and 4.4 requires a theoretical explanation, our group [26,42–47] developed a new model by modifying the SJC model for $V_0(\rho_P)$ and by including the accurate calculation of $P_+(\rho_P)$. In general, the local Wigner-Seitz model for $V_0(\rho_P)$ differs from the SJC model in several significant ways [42]. First, the translational symmetry for the system is defined by a local radius related to the first solvent shell in the perturber, instead of the bulk Wigner-Seitz radius [i.e., eq. (2.13)]. This change is reflected in the calculation of the zero-point kinetic energy of the quasi-free electron.

Second, the average electron/medium polarization is determined in a manner similar to the average ion/medium polarization [i.e., eqs. (2.36) - (2.41)]. Third, since we have controlled the temperature to $\pm 0.5^{\circ}$C, we include the thermal energy of the quasi-free electron (i.e., $(3/2)k_B\,T$), which is greater than the experimental error in some of these measurements. Finally, a phase shift parameter is added to reflect the local dynamic polarization of a perturber by the optical electron. Thus, within the local Wigner-Seitz model, the quasi-free electron energy $V_0(\rho_{\rm P})$ is given by [26, 42–47]

$$V_0(\rho_{\rm P}) \;=\; \frac{3}{2}\,k_B\,T \;+\; E_k(\rho_{\rm P}) \;+\; P_{-}(\rho_{\rm P})\;, \tag{4.12}$$

where $E_k(\rho_{\rm P})$ is the zero-point kinetic energy of the quasi-free electron, and $P_{-}(\rho_{\rm P})$ is the ensemble average electron/perturber polarization energy.

We calculate $P_{-}(\rho_{\rm P})$ in a manner similar to that of the ion/perturber polarization energy $P_{+}(\rho_{\rm P})$ in eqs. (2.36) - (2.41). Following Lekner's original approach [49], the electron/perturber polarization energy $w_{-}(r_1,\ldots,r_N)$ is written as

$$w_{-}(r_1,\ldots,r_N) \;=\; -\,\frac{1}{2}\,\alpha_{\rm P}\,e^2\,\sum_{i}^{N} r_i^{-4}\,f_{-}(r_i)\;, \tag{4.13}$$

where $f_{-}(r)$ is the screening function given by

$$f_{-}(r) \;=\; 1 \;-\; \pi\,\alpha_{\rm P}\,\rho_{\rm P}\int_0^{\infty} ds\;s^{-2}\,g_{\rm PP}(s)\int_{|r-s|}^{r+s} dt\;t^{-2}\,f_{-}(t)\,\theta(r,s,t)\;. \tag{4.14}$$

with $\theta(r,s,t)$ defined in eq. (2.38). The moment analysis of the probability distribution [i.e., eq. (2.29) with $w_{+}(r_1,\ldots,r_N)$ replaced by $w_{-}(r_1,\ldots,r_N)$] yields the first moment, or $P_{-}(\rho_{\rm P})$, as

$$P_{-}(\rho_{\rm P}) \;\equiv\; m_1(\rho_{\rm P}) \;=\; -\,4\,\pi\,\rho_{\rm P}\int_0^{\infty} g_{\rm PP}(r)\,w_{-}(r)\,r^2\,dr\;. \tag{4.15}$$

The zero-point kinetic energy $E_k(\rho_{\rm P})$ of the quasi-free electron, on the other hand, is obtained from solving the Schrödinger equation for the quasi-free electron in a dense perturber, or [26, 42–47, 56]

$$\nabla^2\psi \;+\; \frac{2\,m_e}{\hbar^2}\left(V_0 \;-\; \frac{3}{2}\,k_B\,T \;-\; V(r)\right)\psi \;=\; 0\;, \tag{4.16}$$

where $V(r)$ is the spherically symmetric potential that describes the interaction between the quasi-free electron and the neat perturber. The local Wigner-Seitz model [26, 42–47] assumes that

$$V(r) \;=\; P_{-}(\rho_{\rm P}) \;+\; V_{loc}(r)\;, \tag{4.17}$$

where $P_{-}(\rho_{\rm P})$ is given by eq. (4.15) and is constant for a fixed perturber number density, and $V_{loc}(r)$ is a short-ranged potential that accounts for local dynamic polarization of a perturber by the optical electron. Within these assumptions, eq. (4.16) can be rewritten as

$$\nabla^2\psi \;+\; \frac{2\,m_e}{\hbar^2}\;(E_k \;-\; V_{loc}(r))\;\psi \;=\; 0\;. \tag{4.18}$$

If we define a wavevector

$$k_0 \;\equiv\; \frac{\sqrt{2\,m_e\,E_k}}{\hbar}\;, \tag{4.19}$$

then for a low-kinetic-energy (i.e., s-wave) electron scattering elastically from the short-ranged potential, the asymptotic solution to eq. (4.18) is [111]

$$\psi(r) \;\sim\; \frac{1}{r}\;\sin\left(k_0\,r \;+\; \eta_0\right)\;, \tag{4.20}$$

where η_0 is the phase shift induced by the short-ranged potential.

At high densities, the minimum distance between the optical electron and a single perturber is given by the absolute value of the scattering length $|A|$. However, the maximum distance for the short-ranged interaction is determined by the average translational symmetry for the problem. In a neat fluid of interacting perturbers the density is nonuniform, with the local density $\rho_{\rm P}(r)$ given by [112, 113]

$$\rho_{\rm P}(r) \;=\; \rho_{\rm P}\, g_{\rm PP}(r)\;. \tag{4.21}$$

Using this local density, the Wigner-Seitz radius that determines the average translational symmetry is [26, 42–47]

$$r_\ell \;\equiv\; \sqrt[3]{\frac{3}{4\,\pi\, g_{max}\;\rho_{\rm P}}}\;, \tag{4.22}$$

where g_{max} is the maximum of the perturber/perturber radial distribution function $g_{\rm PP}(r)$. (Thus, the local Wigner-Seitz radius represents one half of the spacing between two perturbers in the first solvent shell.) If the interactions in the first solvent shell dominate $E_k(\rho_{\rm P})$, then the total range r_b for the local potential $V_{loc}(r)$ will be given by

$$r_b \;=\; r_\ell \;-\; |A|\;. \tag{4.23}$$

The average translational symmetry of the potential requires that

$$V_{loc}(r) \;=\; V_{loc}(r \;+\; 2\,r_b)\;, \tag{4.24}$$

which, when applied to the asymptotic wavefunction, yields

$$\sin(k_0\,r \;+\; \eta_0) \;=\; \sin[k_0\,(r \;+\; 2\,r_b) \;+\; 3\,\eta_0]\;, \tag{4.25}$$

Thus, the wavevector k_0, the phase shift η_0 and the scattering length A are related by

$$\eta_0 \;=\; m\,\pi \;-\; k_0\,(r_\ell \;-\; |A|)\;, \tag{4.26}$$

or $\eta_0 \;=\; -\,k_0\,(r_\ell \;-\; |A|)$ for $m = 0$. Thus, the zero-point kinetic energy of the quasi-free electron in eq. (4.19) becomes

$$E_k \;=\; \frac{(\hbar\,k_0)^2}{2\,m_e} \;=\; \frac{\hbar^2\,\eta_0^2}{2\,m_e\,(r_\ell \;-\; |A|)^2}\;. \tag{4.27}$$

This allows the quasi-free electron energy $V_0(\rho_P)$ to be written as

$$V_0(\rho_P) \;=\; P_-(\rho_P) \;+\; \frac{3}{2}\,k_B\,T \;+\; \frac{\hbar^2\,\eta_0^2}{2\,m_e\,(r_\ell \;-\; |A|)^2}\;, \tag{4.28}$$

and the perturber induced shift $\Delta(\rho_P)$ to be given as [26]

$$\Delta(\rho_P) \;=\; P_+(\rho_P) \;+\; P_-(\rho_P) \;+\; \frac{3}{2}\,k_B\,T \;+\; \frac{\hbar^2\,\eta_0^2}{2\,m_e\,(r_\ell \;-\; |A|)^2}\;\;. \tag{4.29}$$

for high perturber number densities.

4.2.2 Temperature dependence in $\Delta(\rho_P)$ at low perturber density

Fig. 4.5 presents the calculated $\Delta(\rho_P)$ in low density Ar and Kr using the local Wigner-Seitz model [i.e., eq. (4.29)] in comparison to the new field ionization results. The perfect fit to the Ar induced CH_3I ionization energy shift $\Delta(\rho_{Ar})$ in Fig. 4.5a clearly shows that the local Wigner-Seitz model accurately predicts the temperature behavior of $\Delta(\rho_P)$ to within the experimental error of ± 10 meV. This temperature behavior arises from the temperature dependence of $P_+(\rho_P)$ caused by variations in the dopant/perturber radial distribution function $g_{PD}(r)$. Although the temperature variation in $g_{PD}(r)$ is large, the variation in $g_{PP}(r)$ is small except near the critical

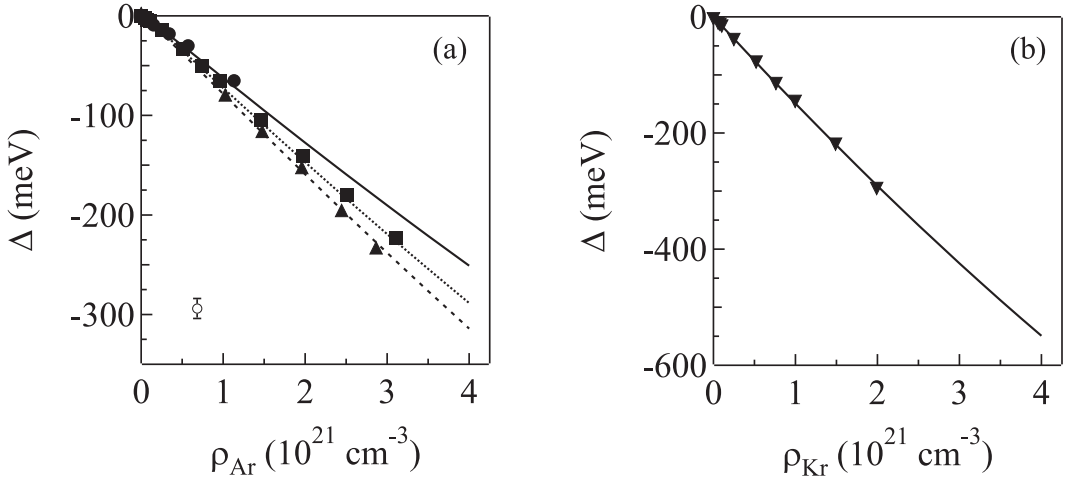

Figure 4.5: The perturber induced shift $\Delta(\rho_P)$ of the CH_3I ionization energy in (a) argon and (b) krypton plotted as a function of perturber number density ρ_P. The solid markers are the experimental data, while the lines are calculated using eq. (4.29). (●, ▼,solid line) 25°C, (■,dotted line) -60°C, and (▲,dashed line) -114°C. The potential parameters required to determine $P_\pm(\rho_P)$ are listed in Table 4.2. For Ar [47], $A = -0.82$ Å and $\eta_0 = -0.329$. For Kr [47], $A = -1.30$ Å and $\eta_0 = -0.133$. The open marker is provided to show the experimental error. See text for discussion.

temperature and density of the perturber. Thus, the quasi-free electron energy $V_0(\rho_P)$ varies with temperature only near the critical density [26,43–47] (see section 4.2.3 for details). (The parameters used in the local Wigner-Seitz calculation are: $A = -0.82$ Å and $\eta_0 = -0.329$ for Ar, and $A = -1.30$ Å and $\eta_0 = -0.133$ for Kr.)

Since the local Wigner-Seitz model works well in the low density region, one can begin to probe the difference between $\Delta_{pol}(\rho_P)$ and $P_+(\rho_P)$, as well as that between $\Delta_{sc}(\rho_P)$ and $V_0(\rho_P)$, as shown in Fig. 4.6. By neglecting the fact that the perturber/perturber interactions increase as the dopant core polarizes the perturber, all the previous low density models (i.e., Fermi model [15], Alekseev-Sobel'man model [6, 22], and Al-Omari-Reininger-Huber model [27]) greatly underestimate the perturber induced shift caused by dopant core/perturber interactions, as has been pointed out previously in the context of sudden and adiabatic polarization effects [25].

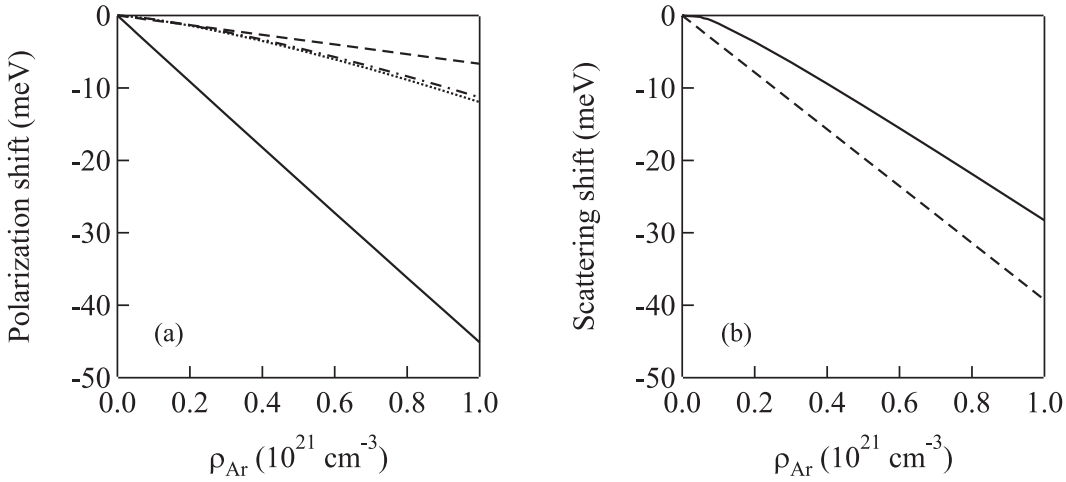

Figure 4.6: (a) The argon induced shift in the CH_3I ionization energy due to CH_3I^+/argon interactions from (solid line) the local Wigner-Seitz model [i.e., $P_+(\rho_P)$ from eq. (2.41)] and from (non-solid lines) previous models [$\cdots$, Fermi model in eq. (2.14), - - -, Alekseev-Sobel'man model in eq. (2.28), and - $\cdot$ -, Al-Omari-Reininger-Huber model in eq. (2.33)]. (b) The argon induced shift in the CH_3I ionization energy due to interaction of the optical electron with argon. The solid line is $V_0(\rho_P)$ calculated from eq. (4.28), while the dashed lines is $\Delta_{sc}(\rho_P)$ obtained from eq. (2.10) for all the scattering models. All calculations were performed for a temperature of $-60°$C. See text for discussion.

This underestimation of $\Delta_{pol}(\rho_P)$ is counterbalanced by the overestimation of $\Delta_{sc}(\rho_P)$, since the latter neglects the polarization of the perturber by the quasi-free electron, as well as the local density of the perturber. Thus, $\Delta_{sc}(\rho_P)$ is significantly larger than the quasi-free electron energy $V_0(\rho_P)$. (We should note here that it was serendipitous that the original experimental studies [3,18,19] were performed at room temperature and at very low perturber densities. Using eqs. (2.1), (2.10), and (2.28) on the data of Fig. 4.5a yields a scattering length A of -0.91 Å at 25°C and -1.51 Å at -114°C. The scattering length from low-kinetic-energy electron scattering experiments is -0.89 Å.)

4.2.3 Critical point effect in Ar, Kr and Xe

Fig. 4.7 shows the calculated average electron/perturber polarization energy $P_-(\rho_P)$ plotted as a function of ρ_P for Ar, Kr and Xe at non-critical temperatures and on an isotherm near the critical isotherm of the perturber [42–46]. One can clearly see in Fig. 4.7 that $P_-(\rho_P)$ shows only a slight increase in $|P_-(\rho_P)|$. This slight increase of the polarization energy at the critical density near the critical temperature of the perturber is also apparent in the dopant core/perturber polarization energy (cf. Fig. 4.3). This critical point effect, which results from the increase of the radial distribution function at the perturber critical point, is similar to the behavior observed for vibrational and UV-visible absorption bands [2].

Fig. 4.8 presents the zero-point kinetic energy $E_k(\rho_P)$ calculated from eq. (4.27) [42–46] with the parameters given in Table 4.3 [47]. Similar to $P_-(\rho_P)$ and $P_+(\rho_P)$, the zero-point kinetic energy $E_k(\rho_P)$ also increases along the critical isotherm near the critical point. (It is interesting to note that the critical isotherm turning points that bound the saddle point in the argon phase diagram coincide with the number densities that delimit the deviations of $E_k(\rho_P)$ from the non-critical isotherm values.) This increase in the kinetic energy of the quasi-free electron, which results from critical point fluctuations that are reflected in variations in the radial distribution function in the critical point region, is a consequence of the decreasing value of r_b: as the total range of the local potential $V_{loc}(r)$ decreases (or the translational boundary condition for the quasi-free electron wavefunction decreases), the kinetic energy of the quasi-free electron must increase.

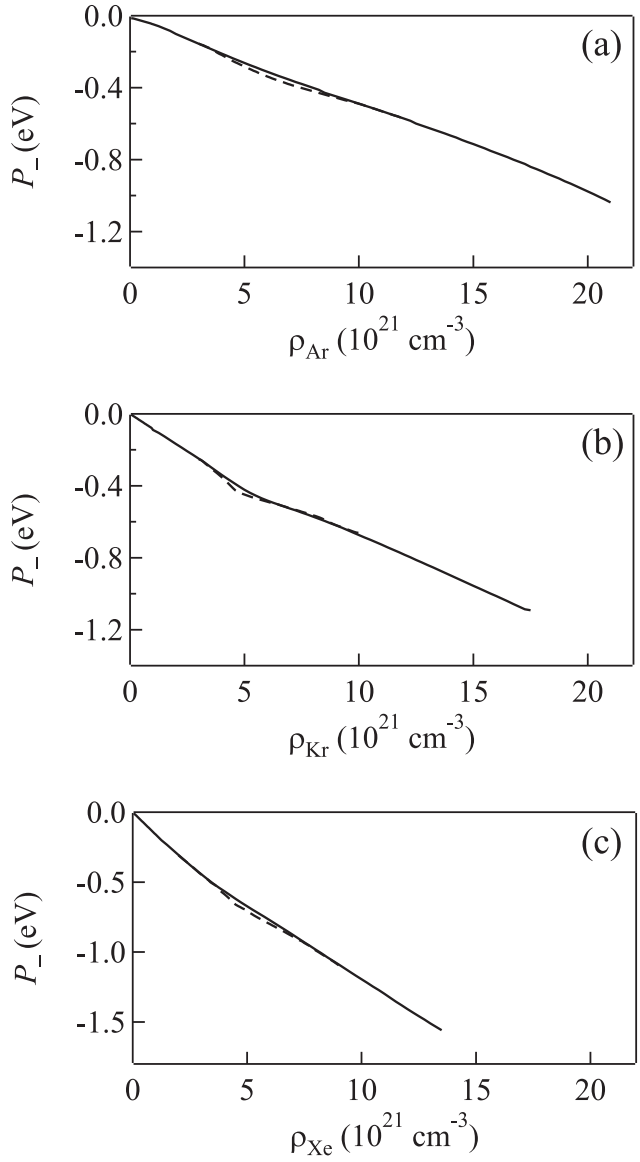

Figure 4.7: The average electron/perturber polarization energy $P_{-}(\rho_P)$ in (a) Ar [42–44], (b) Kr [42,45] and (c) Xe [46], calculated from eq. (4.15) using the intermolecular potential parameters in Table 4.2, plotted as a function of perturber number density ρ_P, at non-critical temperatures (——) and on an isotherm near the critical isotherm of the perturber (- - -).

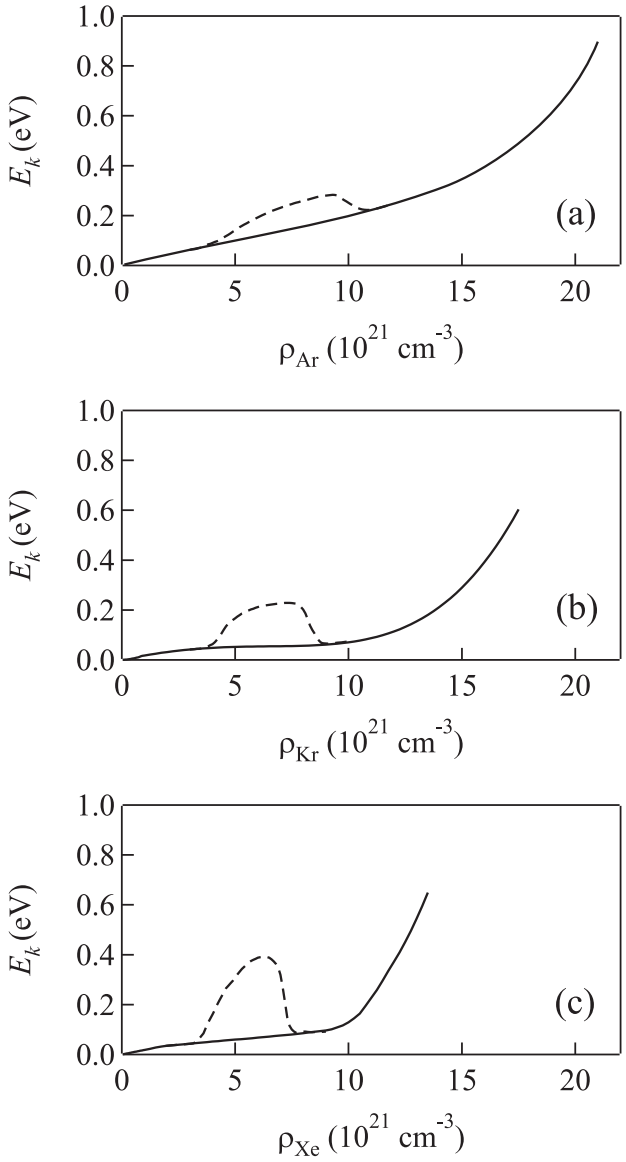

Figure 4.8: The zero-point kinetic energy $E_k(\rho_P)$ in (a) Ar [42–44], (b) Kr [42, 45] and (c) Xe [46], calculated from eq. (4.27) using the parameters in Table 4.3, plotted as a function of perturber number density ρ_P, at non-critical temperatures (——) and on an isotherm near the critical isotherm of the perturber (- - -).

Table 4.3: The zero-kinetic-energy electron scattering length A and the phase shift η_0 used in the local Wigner-Seitz model [i.e., eqs. (4.27)-(4.29)] calculation for argon, krypton and xenon.

Perturber	A (Å)	η_0
Ar	-0.82 ± 0.02	0.329 ± 0.003
Kr	-1.30 ± 0.05	0.133 ± 0.004
Xe	-1.75 ± 0.08	0.015 ± 0.005

Finally, Fig. 4.9 presents the quasi-free electron energy $V_0(\rho_P)$ obtained within the local Wigner-Seitz model (lines) in comparison to the experimental results (markers) [42–47]. The error shown at the top of Figs. 4.9a, b and c is the difference between the extracted $V_0(\rho_P)$ values (cf. Fig. 4.4) and the values calculated from eq. (4.28). The horizontal dotted lines denote the overall experimental error limits. Clearly, the calculated $V_0(\rho_P)$ closely matches the $V_0(\rho_P)$ extracted from the experimental field ionization data over the entire density range for all temperatures. Moreover, the scatter falls within the intrinsic error of the experimental measurements. From Fig. 4.7 and Fig. 4.8, along the critical isotherm near the perturber critical point, the zero-point kinetic energy $E_k(\rho_P)$ increases by approximately 0.1 eV in Ar, 0.16 eV in Kr, and 0.3 eV in Xe, while $|P_-(\rho_P)|$ increases by 0.03 eV for Ar, 0.04 eV for Kr, and 0.04 eV for Xe. Therefore, $E_k(\rho_P)$ is the determining factor for the decrease in $|V_0(\rho_P)|$. Furthermore, the increase in $E_k(\rho_P)$ near the xenon critical point is nearly a factor of 4 greater than that in argon and nearly a factor of 2 greater than that in krypton, which presumably results from the greater polarizability of xenon.

With an accurate calculation of $V_0(\rho_P)$ (cf. Fig. 4.9), eq. (2.35) can now be used to model the perturber-induced energy shift $\Delta(\rho_P)$ of the dopant ionization energy.

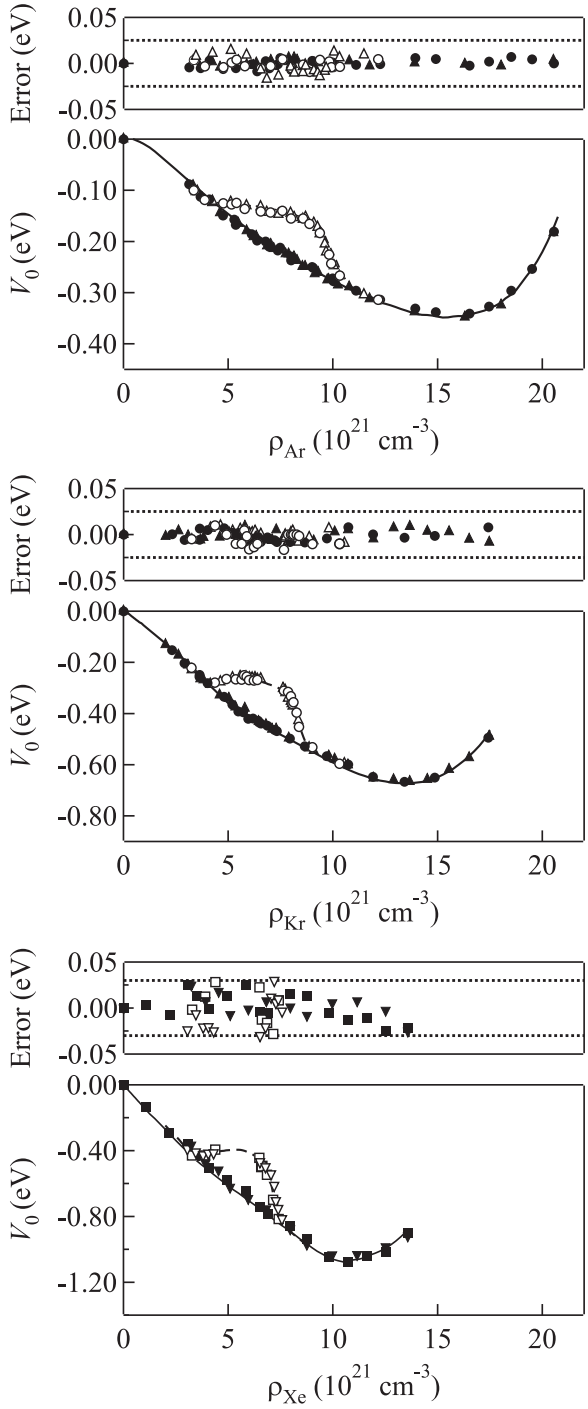

Figure 4.9: Comparison of experiment (markers) and calculation (lines) for the quasi-free electron energy $V_0(\rho_P)$ in (a) Ar, (b) Kr, and (c) Xe. See the legend of Fig. 4.4 for the definition of the markers. The solid line is for various non-critical temperatures; the dashed line is for an isotherm near the perturber critical isotherm. The error shown is the difference between the experimental $V_0(\rho_P)$ and the calculated values. The horizontal dotted lines represent the experimental error limits. See text for details.

Fig. 4.10 presents the calculated $\Delta(\rho_P)$ for all dopant/perturber systems (lines), using $P_+(\rho_P)$ shown in Fig. 4.3 and $V_0(\rho_P)$ given in Figs. 4.9, in comparison to the experimentally determined values (markers) [42–46]. Clearly, the calculated $\Delta(\rho_P)$ also closely matches experiment with a scatter that falls within the experimental error of $\pm$ 0.02 - 0.03 eV. These data show that the decrease in $|V_0(\rho_P)|$ is the dominant factor in the overall decrease in $|\Delta(\rho_P)|$ near the critical point along the critical isotherm of the perturber.

Thus, the local Wigner-Seitz model accurately predicts the quasi-free electron energy $V_0(\rho_P)$ and the perturber-induced dopant ionization energy shift $\Delta(\rho_P)$ for all dopant/perturber systems, and therefore provides a significant improvement in accuracy in comparison to previously published models (cf. Fig. 2.8). (It is important to note that there is only a single adjustable parameter η_0 in this model.) With an accurate model for the behavior of the quasi-free electron in attractive atomic perturbers, the next step in understanding electron interactions in supercritical fluids is to investigate molecular fluids. In the next chapter, we will present experimental field ionization data for various dopants in molecular supercritical fluids, and we will use these data to extend the local Wigner-Seitz model to molecular fluids.

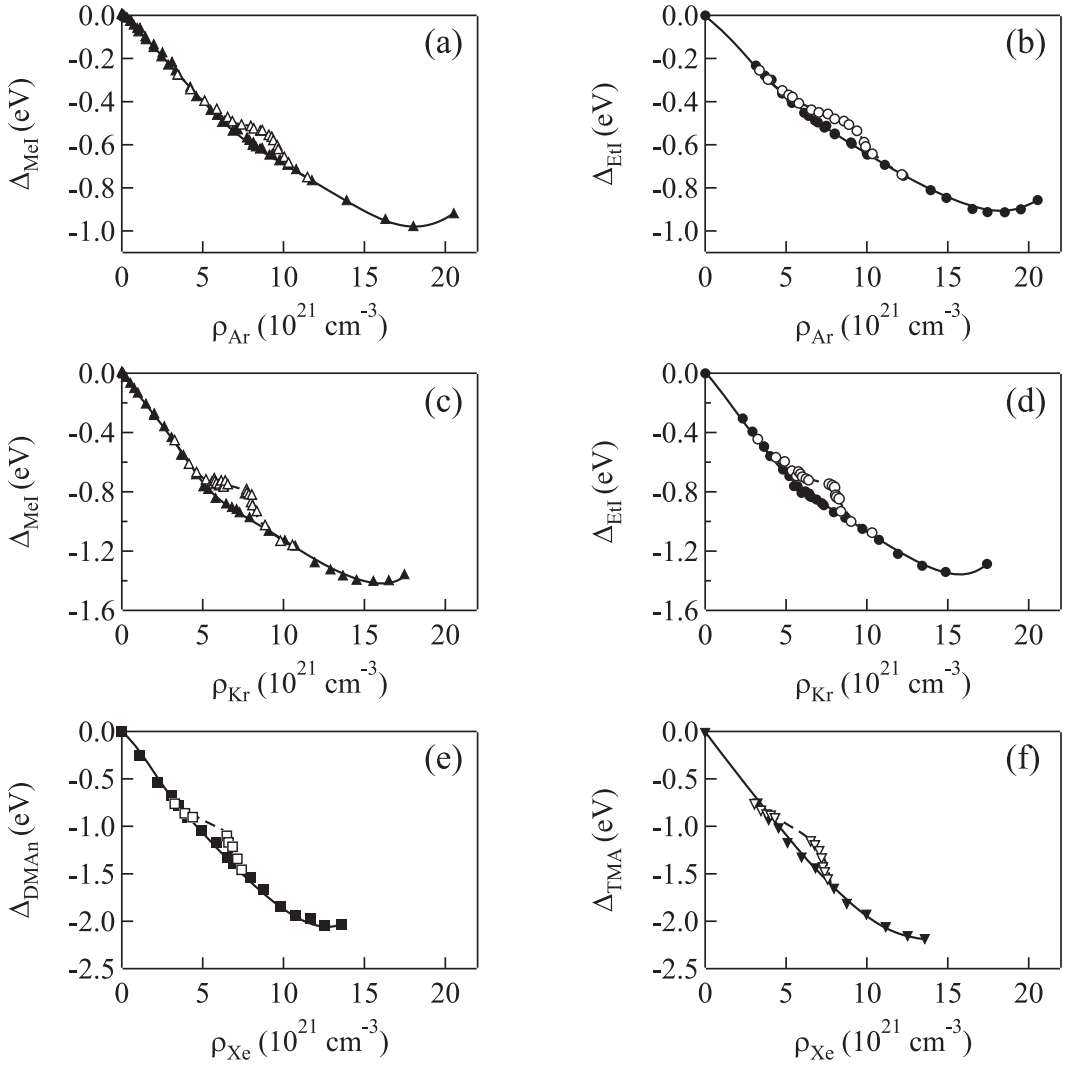

Figure 4.10: Comparison of experiment (markers) and calculation (lines) for the perturber-induced dopant ionization energy $\Delta(\rho_P)$ as a function of perturber number density ρ_P. See the legend of Fig. 4.2 for the definition of the markers. The solid line is for various non-critical temperatures; the dashed line is for an isotherm near the perturber critical isotherm. See text for details.

Chapter 5

Quasi-free electron energy $V_0(\rho_{\mathrm{P}})$ in molecular gases

In this chapter, we present field ionization of trimethylamine (TMA) in methane and triethylamine (TEA) in ethane at non-critical temperatures and on an isotherm near the perturber critical isotherm. Critical point effects similar to those observed in atomic fluids (cf. Chapter 4) are reported for methane and ethane. In order to extend the local Wigner-Seitz model to molecular fluids, various perturber/perturber intermolecular potentials, as well as methods to calculate radial distribution functions, are then investigated. The local Wigner-Seitz fits to $\Delta(\rho_{\mathrm{P}})$ and $V_0(\rho_{\mathrm{P}})$ in methane and ethane are presented and discussed. Finally, we also discuss our unsuccessful attempts to measure field ionization of various dopants in CF_4, and we use the results obtained from methane and ethane to predict $V_0(\rho_{\mathrm{P}})$ for CF_4.

5.1 Experimental results

5.1.1 $\Delta(\rho_{\mathrm{P}})$ of TMA in methane

Methane was the first molecular fluid chosen for this study because it is an attractive molecule (indicating a negative electron scattering length A) of high symmetry and can therefore be considered as a molecular analogue of the attractive rare gas systems

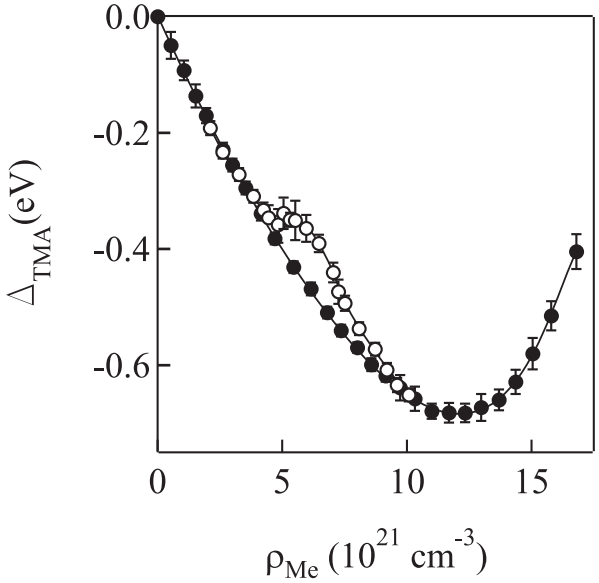

Figure 5.1: Methane induced shift $\Delta(\rho_{\rm Me})$ of the TMA ionization energy plotted as a function of methane number density $\rho_{\rm Me}$ at various non-critical temperatures (•) and for an isotherm (−81.5° C) near the methane critical isotherm (∘). The lines are provided as a visual aid.

discussed in Chapter 4. Fig. 5.1 presents the methane induced shift $\Delta(\rho_{\rm Me})$ of the TMA ionization energy plotted as a function of methane number density $\rho_{\rm Me}$. The data represented by the solid markers were taken along the non-critical isotherms 23.7°C, −35.1°C, −69.9°C and −74.8°C for methane densities of (0.5 - 8.6) $\times 10^{21}$ cm^{-3}, as well as at other temperatures for the higher densities. The data point at the highest methane density was acquired at a temperature of −179°C, which is near the triple point temperature of −182°C. The open markers in Fig. 5.1 were obtained along the isotherm of −81.5°C, which is near the methane critical temperature of −82.0°C. The electric fields, selected to obtain the best field ionization spectra, were $F_L = 5000$ V cm^{-1} and $F_H = 13333$ V cm^{-1} for all spectra. The maximum error for non-critical temperatures is 27 meV, while the error is 35 meV along the critical isotherm of methane. The larger error that is evident for a few points near the

critical temperature and density is due to increased noise and asymmetry in the field ionization spectra caused by increased light absorption and light scattering by critical point CH_4. Similar to the data in attractive rare gas systems (cf. Chapter 4), the data presented in Fig. 5.1 show a clear decrease in the density dependent shift $\Delta(\rho_{Me})$ near the methane critical number density ($\rho_{Me} = 6.1 \times 10^{21}$ cm^{-3}) along the critical isotherm. Moreover, $\Delta(\rho_{Me})$ achieves a minimum at the methane density of 12×10^{21} cm^{-3}, which was also observed in previous photoinjection results [85,89] (cf. Fig. 2.6a).

5.1.2 $\Delta(\rho_P)$ of TEA in ethane

Since the field ionization results (cf. Fig. 5.1) show that the methane induced shift $\Delta(\rho_{Me})$ of dopant ionization energy behaves in a manner similar to that of the attractive rare gases [42–47] (cf. Fig. 4.2), a natural extension of these measurements was to study ethane, which is also an attractive system. However, the photoinjection measurements of ethane [85, 90, 91] (cf. Fig. 2.6b) showed significant differences in comparison to those of methane [85, 89] (cf. Fig. 2.6a). The most striking of these differences is the positive value of $V_0(\rho_P)$ at ethane number densities greater than 10.3×10^{21} cm^{-3}. Given the problems in correcting photoinjection measurements (cf. Section 2.2.2.a), we decided to perform field ionization measurements in ethane at non-critical temperatures to confirm these differences. This new study also gave us the opportunity to obtain data along the ethane critical isotherm, thereby enabling us to investigate critical point effects in ethane.

The field ionization results in ethane were obtained during two different measurement periods using two different sample cells (cf. Fig. 3.2). Fig. 5.2 presents the

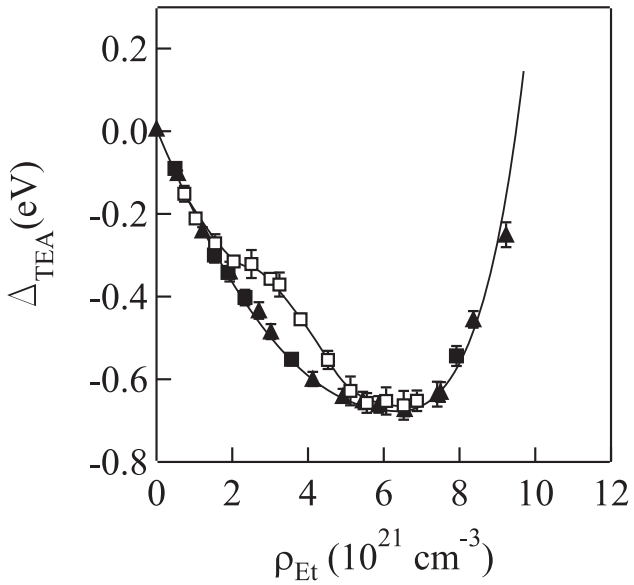

Figure 5.2: Ethane induced shift $\Delta(\rho_{Et})$ of the TEA ionization energy plotted as a function of ethane number density ρ_{Et} at various non-critical temperatures (▲, ■) and for an isotherm (32.5° C) near the ethane critical isotherm (□). Some data points were measured in cell 1 (cf. Fig. 3.2a) (▲) while others were measured in cell 2 (cf. Fig. 3.2b) (■, □). The lines are provided as a visual aid.

ethane induced shift $\Delta(\rho_{Et})$ of the TEA ionization energy plotted as a function of ethane number density ρ_{Et}. Clearly, since the data measured in Cell 2 (■) are consistent with those from Cell 1 (▲) for non-critical temperatures, the $\Delta(\rho_{Et})$ obtained for the critical temperature in Cell 2 (□) is valid. The data represented by the solid markers were taken along the non-critical isotherms 37.8°C and 42.6°C for ethane densities of (0.5 - 5.9) $\times 10^{21}$ cm^{-3}, as well as at other temperatures for the higher densities. The open markers were obtained along the isotherm of 32.7°C, which is near the ethane critical temperature of 32.2°C. The maximum error for non-critical temperatures is 30 meV, while the error is 40 meV along the critical isotherm of ethane. The lack of data points in the high ethane density range (i.e., $\rho_{Et} > 10.0 \times 10^{21}$ cm^{-3}) results from poor quality field ionization spectra caused by the shift of the TEA ionization energy under the broad absorption band of ethane. However, these

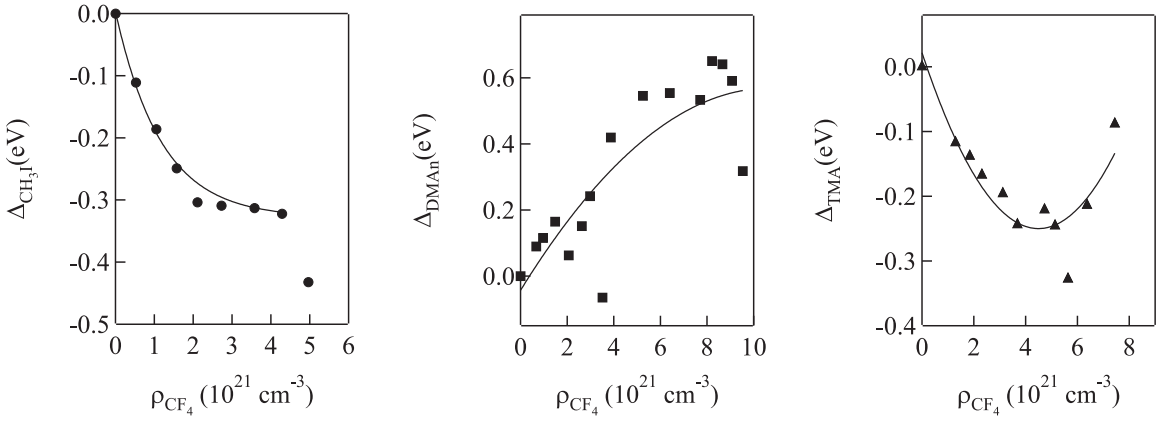

Figure 5.3: CF_4 induced shift $\Delta(\rho_{CF_4})$ of the ionization energy of (a) CH_3I (●), (b) DMAn (■), and (c) TMA (▲) plotted as a function of CF_4 number density ρ_{CF_4} at various noncritical temperatures. The lines are provided as a visual aid.

experimental data illustrate that $\Delta(\rho_{Et})$ will become positive at high ethane number densities. Therefore, the quasi-free electron energy $V_0(\rho_{Et})$ extracted from these data using eq. (4.11) will become positive, because $P_+(\rho_P)$ is always negative.

5.1.3 Field ionization of various dopants in CF_4

Carbon tetrafluoride (CF_4) was chosen for study because of its importance in plasma etching procedures, because it is transparent in the energy region of interest, and because its critical temperature (i.e., $T_c = -35.7°C$) and pressure (i.e., $p_c = 37.7$ bar) are easily within the capabilities of our gas handling system and sample cell. However, we were unsuccessful in obtaining the necessary field ionization data required to extract the quasi-free electron energy $V_0(\rho_{CF_4})$. We attempted to measure the field ionization of CH_3I (cf. Fig. 5.3a), DMAn (cf. Fig. 5.3b) and TMA(cf. Fig. 5.3c). As can be clearly seen in Fig. 5.3, we were unable to obtain a consistent data set at medium to high CF_4 number densities. (The triple point density of CF_4 is 12.9×10^{21} cm^{-3}.) Since we have encountered problems in measuring dopant field ionization in

CF_4 with three very different dopants, we have concluded that the difficulties inherent in measuring dopant field ionization are caused by the perturber. Although CF_4 is not known to form a stable negative ion, the behavior that we observed in the dopant field ionization spectra seems to indicate some form of electron trapping in the fluid. (If the quasi-free electron is trapped by the fluid, we would not expect to collect all of the electrons generated from the excitation, thereby resulting in fluctuations in the field ionization spectrum.) One possible explanation for this behavior is the stabilization of a CF_4 negative ion within a cluster of CF_4 molecules.

5.2 Discussion

5.2.1 Calculation of radial distribution functions (RDFs)

Within the local Wigner-Seitz model [26, 42–47] [i.e., eq. (4.29)], the calculation of $P_-(\rho_P)$ [i.e., eq. (4.15)] and $P_+(\rho_P)$ [i.e., eq. (2.41)] involves the perturber/perturber radial distribution function $g_{PP}(r)$ and the dopant/perturber radial distribution function $g_{PD}(r)$, while r_l in eq. (4.29) is determined by the maximum g_{max} of $g_{PP}(r)$ [i.e., eq. (4.22)]. Therefore, accurately calculating the radial distribution function for the system over a large density and temperature range is very important for the local Wigner-Seitz model. In our original attempt to model the TMA/CH_4 system, we encountered numerical instabilities in determining the RDFs at high densities near the perturber triple point, as well as along isotherms close to the critical temperature (especially when changing intermolecular potentials). In an attempt to stabilize these numerical calculations, we compared the direct iteration method [107] and the Gillan-Labik method [114,115] for numerically integrating the Ornstein-Zernike relation with a Percus-Yevick closure.

The direct iteration method was used to calculate the RDFs in our original investigations [42] given in Section 4.1.2. As long as $\rho_{\rm P}$ is three orders of magnitude larger than $\rho_{\rm D}$, the dimensionality of the problem [i.e., eqs. (4.1) - (4.3)] is reduced from four to two, namely $Y_{\rm PP}(r)$ and $Y_{\rm PD}(r)$. In the discussion that follows, we define $Y^{(i)}$ as the set $\{Y_{\rm PP}(r),\, Y_{\rm PD}(r)\}$ for each iteration i. To numerically solve for $Y_{\rm PP}(r)$ and $Y_{\rm PD}(r)$ within the direct iteration method, we used a technique developed by Broyles [116] during the 1960s. This technique initially guesses that, for the first density/temperature calculation, $Y^{(1)} = r$, where r is the pairwise internuclear distance. Then, this initial guess is placed into eqs. (4.2) and (4.3) to obtain $Y^{(2)}$. Once $Y^{(2)}$ is determined, a linear combination of $Y^{(1)}$ and $Y^{(2)}$ is taken using [116]

$$Y^{(2)} = aY^{(2)} + (1-a)Y^{(1)}\,, \tag{5.1}$$

where $0 < a < 1$. (We should note here that a straight iterative technique will diverge exponentially [116], which is the reason that a linear combination of the previous input and the current output radial distribution functions are used to determine the new input.) This new $Y^{(2)}$ is inserted back into eqs. (4.2) and (4.3) to determine the next iterative pair $Y^{(3)}$; $Y^{(3)}$ is then modified using eq. (5.1) to give a new $Y^{(3)}$ which is input back into eqs. (4.2) and (4.3). This simple iteration continues until two iterative steps yield values for $Y^{(n)}$ and $Y^{(n+1)}$ that satisfy the convergence criteria

$$\frac{1}{3M}\sum_{k=1}^{M}\left[\Delta Y^2_{\rm PP}(r_k) + \Delta Y^2_{\rm PD}(r_k)\right] < 10^{-9}\,, \quad \max(\Delta Y)^2 < 10^{-8}\,, \tag{5.2}$$

where $\Delta Y_{ij}(r) = Y_{ij}^{(n+1)}(r) - Y_{ij}^{(n)}(r)$ and $\Delta Y = Y^{(n+1)} - Y^{(n)}$. Once the system converges, this $Y^{(n)}$ is saved for use as the $Y^{(1)}$ for the next temperature/density point. Within this simple iterative approach, each step generates a set $Y^{(i)}$ that

oscillates around the "exact" solution to eqs. (4.2) and (4.3). Our investigations showed that this method converges for the rare gases at all densities with a Lennard-Jones 6-12 potential, but can diverge when switching to other spherical intermolecular potentials, especially when calculating RDFs for high perturber densities or along the critical isotherm.

Another commonly used integration technique for the Ornstein-Zernike equations (especially when handling closures other than the Percus-Yevick closure) is the Gillan-Labik method [114, 115]. This method starts by determining the indirect correlation function from the Fourier transform of the Ornstein-Zernike equations, namely

$$\widetilde{h}_{ij}(s) - \widetilde{c}_{ij}(s) = \sum_k \rho_k \, \widetilde{c}_{jk}(s) \, \widetilde{h}_{ki}(s) \; , \tag{5.3}$$

where $\widetilde{h}_{ij}(s)$ and $\widetilde{c}_{ij}(s)$ are the Fourier transforms of the total correlation function $h_{ij}(r)$ and the direct correlation function $c_{ij}(r)$, respectively, in the reciprocal s space. The indirect correlation function, given by eq. (5.3), is divided into two parts: a slowly varying coarse part and a rapidly oscillating fine part. The solutions for each iteration are generated by a combination of Newton-Rhapson integration steps (on the coarse part) and direct iteration steps (on the fine part). Since the Gillan-Labik method does not depend on an analytical solution of the Ornstein-Zernike equation with a specified closure, it can be successfully applied to eq. (5.3) with any closure (e.g., the Hypernetted chain (HNC) closure, the Percus-Yevick closure, etc.). However, although the Gillan-Labik method increases the calculation speed dramatically, this method does not increase the probability of convergence to a stable numerical solution at high perturber number densities or at temperatures and densities near the critical point of the perturber. Moreover, for intermolecular potentials that give stable calculations, the

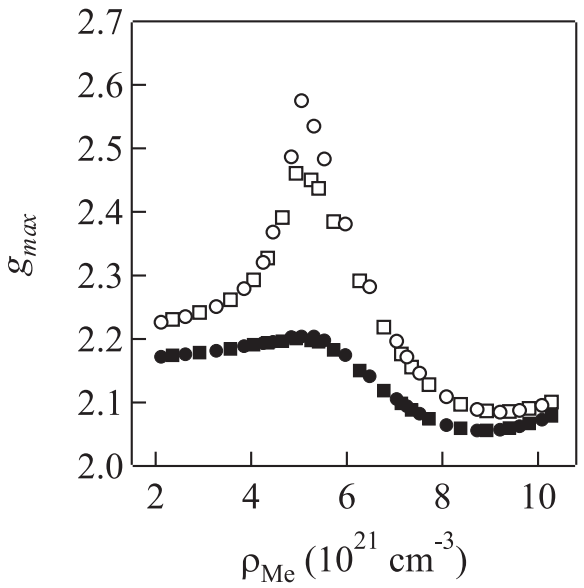

Figure 5.4: The maximum g_{max} of the perturber/perturber radial distribution function $g_{PP}(r)$ plotted as a function of methane number density ρ_{Me} along isotherms 0.5°C (open markers) and 5.0°C (closed markers) above the methane critical temperature. The radial distribution functions are calculated using both the direct iteration method (●, ○) and the Gillan-Labik method (■, □). A Lennard-Jones 6-12 potential is used for the perturber/perturber interaction with parameters $\sigma_{PP} = 3.599$ Å, $\varepsilon_{PP}/k_B = 151.0$ K. See text for discussion.

Gillan-Labik method gives a smaller critical point effect for the Percus-Yevick closure than does the direct iteration method (cf. Fig. 5.4). We also used the Gillan-Labik method to integrate eq. (5.3) within a Hypernetted chain (HNC) closure. However, we never succeeded in obtaining RDFs (i.e., $g_{ij}(r) = h_{ij}(r) + 1$) for temperatures and densities near the critical point of a fluid. We concluded our investigation of different numerical approaches by testing the Baxter method [117, 118], which arises from a factorized Ornstein-Zernike equation. However, the stability of this numerical technique is again a problem for high perturber number densities and for temperatures and densities near the critical point of the perturber.

While we were unsuccessful in finding a more stable integration technique for the Ornstein-Zernike relation, we were able to stabilize the numerical calculation of

eqs. (4.2) and (4.3) using an optimizing routine developed by Ng [119]. This routine [119] uses a weighted linear combination of three previous iterations to generate the input for the next iteration. The application of this procedure to eqs. (4.2) and (4.3) begins by rewriting these equations as

$$Y^{(n+1)} = \mathcal{A}\, Y^{(n)} \,, \tag{5.4}$$

where $\mathcal{A}$ is the operator defined by

$$\mathcal{A} = \int_0^r dt\, \frac{d}{dt} \,. \tag{5.5}$$

For the sake of convenience, we define the input for the nth iteration as $Y^{(n)}$ and the output of the nth iteration as $G^{(n)}$ [i.e., $G^{(n)} \equiv \mathcal{A}\, Y^{(n)} = Y^{(n+1)}$]. We also define a function $D^{(n)}$, the norm of which determines the degree of convergence of the solution. Thus, $D^{(n)} \equiv G^{(n)} - Y^{(n)} = Y^{(n+1)} - Y^{(n)}$. This procedure requires the knowledge of four sets of radial distribution functions, three of which are obtained from previous iterations [i.e., $Y^{(n-2)}$, $Y^{(n-1)}$ and $Y^{(n)}$] and the fourth of which is the output from the current iteration $Y^{(n+1)}$. We then assume that we can write a possible input function as [119]

$$\overline{Y} = (1 - c_1 - c_2)Y^{(n)} + c_1 Y^{(n-1)} + c_2 Y^{(n-2)} \,, \tag{5.6}$$

where c_1 and c_2 are constants that can be optimized in such a way that $\overline{Y}$ is the best solution to eq. (5.4). If $\mathcal{A}$ behaves linearly for the iterative steps involved in the calculation, we can write [119]

$$\begin{aligned} \mathcal{A}\overline{Y} &= (1 - c_1 - c_2)\mathcal{A}Y^{(n)} + c_1 \mathcal{A}Y^{(n-1)} + c_2 \mathcal{A}Y^{(n-2)} \\ &= (1 - c_1 - c_2)G^{(n)} + c_1 G^{(n-1)} + c_2 G^{(n-2)} \,. \end{aligned} \tag{5.7}$$

The convergence of the solution $\overline{Y}$ can be tested by taking the norm of the difference between $\overline{Y}$ and $\mathcal{A}\overline{Y}$, which can be written as [119]

$$\overline{D}^2 = \| \mathcal{A}\overline{Y} - \overline{Y} \|^2 = \| D^{(n)} - c_1 D_{01} - c_2 D_{02} \|^2 , \tag{5.8}$$

where

$$D_{01} = D^{(n)} - D^{(n-1)} , \quad D_{02} = D^{(n)} - D^{(n-2)} . \tag{5.9}$$

Minimization of $\overline{D}^2$ with respect to c_1 and c_2 gives coefficients that optimize $\overline{Y}$ as the best solution to eq. (5.4) for any given iteration step. The functional forms of c_1 and c_2 are given by [119]

$$\begin{aligned} c_1 &= \frac{(D^{(n)}, D_{01})(D_{02}, D_{02}) + (D^{(n)}, D_{02})(D_{01}, D_{02})}{(D_{01}, D_{01})(D_{02}, D_{02}) - (D_{01}, D_{02})^2} , \\ c_2 &= \frac{(D^{(n)}, D_{02})(D_{01}, D_{01}) + (D^{(n)}, D_{01})(D_{01}, D_{02})}{(D_{01}, D_{01})(D_{02}, D_{02}) - (D_{01}, D_{02})^2} , \end{aligned} \tag{5.10}$$

where (x, y) represent inner products defined by

$$(x, y) = \int x(r) y(r) dr . \tag{5.11}$$

Thus, the best input for the $(n+1)$th iteration is given by eq. (5.7) with c_1 and c_2 defined by eq. (5.10). When we coded this procedure, we assumed $Y^{(1)} = r$ for the first temperature/density point. The second and the third iteration were determined using the standard iterative technique with a smaller a in eq. (5.1). However, all three of these iterations were stored to be used in the fourth iteration, the input of which is defined by eq. (5.7). Each subsequent iteration uses the input generated by eq. (5.7), which means that three sets of radial distribution functions must be stored at all times. Once the calculation converges for the given temperature/density point, the algorithm moves to the next temperature/density point and uses the last three

sets of $Y^{(i)}$ from the previous temperature/density point to generate the first guess. Thus, the simple iterative method represented by eq. (5.1) is only used to generate the first three iterative guesses of the first temperature/density point.

We have extended this optimization model [119] to allow for the inclusion of an unlimited number m of iterative solutions to be combined to generate the input for the next iteration. This extension involves numerically solving homogeneous linear equations to obtain the $m-1$ weighting coefficients (i.e., c_1, c_2, $\cdots$, c_{m-1}). Notice that when m is chosen to be 1, the method reduces to the original direct iteration procedure [107]. Further tests showed that the calculated results with different m values are all within the convergence criteria [i.e., eq. (5.2)] of the "exact" solution to eqs. (4.1) - (4.3), which allows one to choose m so as to maximize the stability of the calculation for any perturber density/temperature data set.

5.2.2 Intermolecular potentials

One of our goals in this study was to achieve an understanding of the intermolecular potentials governing the dopant/perturber and perturber/perturber interactions in dense molecular fluids. One question was the appropriateness of using spherical intermolecular potentials to model data in non-spherical dense fluids. Table 5.1 lists several commonly used spherical intermolecular potentials [120], namely, Lennard-Jones 6-12 (LJ6-12), Lennard-Jones 7-28 (LJ7-28), Kihara (KIH), Exponential-6 (EXP6), and 11-6-8 potential, while Fig. 5.5 plots each of the potentials as a function of the intermolecular distance r with selected parameters for methane [121–125].

Obviously, different potentials reflect different attractive and repulsive interactions by the varying potential well-depths, collision radii and steepness of both the attrac-

Table 5.1: Various spherical intermolecular potentials [120] used to extend the local Wigner-Seitz model to methane and ethane. For these potentials, σ and r_m are collision radii, ε is the potential well-depth, a is the size parameter, and γ gauges the steepness of the intermolecular potential.

Name	Functional form
Lennard Jones 6-12 (LJ6-12)	$U(r) = 4\,\varepsilon\,\left[\left(\frac{\sigma}{r}\right)^{12} - \left(\frac{\sigma}{r}\right)^{6}\right]$
Lennard Jones 7-28 (LJ7-28)	$U(r) = 4\,\varepsilon\,\left[\left(\frac{\sigma}{r}\right)^{28} - \left(\frac{\sigma}{r}\right)^{7}\right]$
Kihara (KIH)	$U(r) = 4\,\varepsilon\,\left[\left(\frac{\sigma-2a}{r-2a}\right)^{12} - \left(\frac{\sigma-2a}{r-2a}\right)^{6}\right]$
Exponential-6 (EXP6)	$U(r) = \frac{\varepsilon}{1-6/\gamma}\,\left[\frac{6}{\gamma}\,e^{\gamma(1-r/r_m)} - \left(\frac{r_m}{r}\right)^{6}\right]$
11-6-8 Potential (11-6-8)	$U(r) = 4\,\varepsilon\,\left[\frac{12}{5}\left(\frac{r_m}{r}\right)^{11} - \frac{2}{5}\left(\frac{r_m}{r}\right)^{6} - 3\left(\frac{r_m}{r}\right)^{8}\right]$

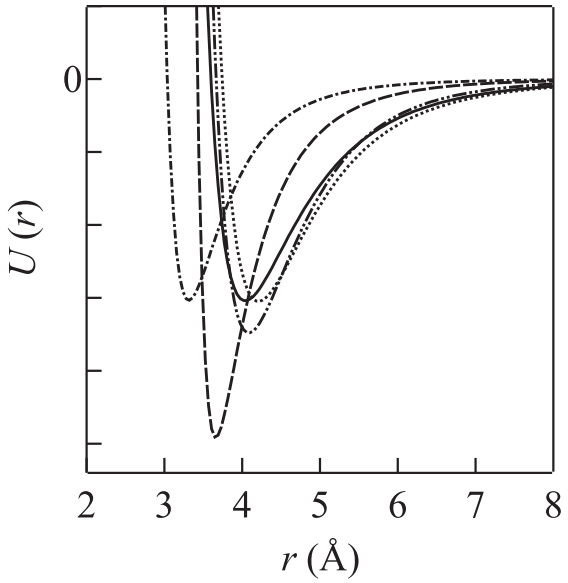

Figure 5.5: Different intermolecular potentials for methane/methane interactions. (——) Lennard-Jones 6-12 potential with $\varepsilon/k_B = 152.0$ K, $\sigma = 3.599$ Å [121]; (- - -) Lennard-Jones 7-28 potential with $\varepsilon/k_B = 130.0$ K, $\sigma = 3.426$ Å [122]; (- · -) Kihara potential with $\varepsilon/k_B = 151.7$ K, $\sigma = 3.0367$ Å, $a = 0.3864$ Å [123]; (· · ·) Exponential-6 potential with $\gamma = 14$, $\varepsilon/k_B = 152.4$ K, $r_m = 4.209$ Å [124]; and (- · · -) 11-6-8 potential with $\varepsilon/k_B = 174.0$ K, $r_m = 4.0849$ Å [125].

tive and repulsive terms. In order to achieve a better overall fit to the experimental data, we needed to be able to adjust all of the above parameters. Our first choice for a spherical potential suitable for modeling molecular systems was the two-Yukawa (TY) potential, given by

$$U(r) = \begin{cases} \infty \,, & r < R \,, \\ -\kappa_0 \varepsilon r^{-1} \left[e^{-z_1(r-\sigma)} - e^{-z_2(r-\sigma)} \right] \,, & r \geq R \,. \end{cases} \tag{5.12}$$

because this potential allows us to vary the collision radius σ, the well-depth $\kappa_0\varepsilon$ and the steepness of the attractive z_1 and repulsive z_2 tails independently. (R is a hard core radius that defines the minimum distance between spherical perturbers.) Another advantage of using the two-Yukawa potential is that it can mimic any of the other spherical potentials. For example, if we assume that σ and ε are the same as in the Lennard-Jones 6-12 potential (cf. Table 5.1), Tang, *et al* [126] showed that κ_0, z_1 and z_2 can be determined by solving the constraint equations

$$\left[rU^{TY}(r) \right] \big|_{r=\sigma} = \left[rU^{LJ}(r) \right] \big|_{r=\sigma} \,, \quad \left[rU^{TY}(r) \right]' \Big|_{r=\sigma} = \left[rU^{LJ}(r) \right]' \Big|_{r=\sigma} \,, \tag{5.13}$$

where U^{TY} stands for the two-Yukawa potential while U^{LJ} represents the Lennard-Jones 6-12 potential. In addition, minimizing

$$\mathcal{I} = \int_\sigma^\infty \left[rU^{TY}(r) - rU^{LJ}(r) \right]^2 dr \tag{5.14}$$

leads to

$$\frac{\partial \mathcal{I}}{\partial z_1} = 0 \,, \quad \frac{\partial \mathcal{I}}{\partial z_2} = 0 \,. \tag{5.15}$$

Solving eqs. (5.13) $-$ (5.15) with an upper integration limit in eq. (5.14) of 3σ yields $\kappa_0 = 2.1714\sigma$, $z_1 = 2.9637/\sigma$ and $z_2 = 14.0167/\sigma$ [126].

However, the two-Yukawa potential has five parameters that can be adjusted independently. Therefore, in order to verify the validity of the perturber/perturber intermolecular potential parameters and the radial distribution functions calculated using these parameters, the thermodynamic properties of the system were simulated and compared to experimental data. For simplicity we chose to calculate the equation of state (EOS) of the perturber using the standard relationship [127]

$$\frac{p}{k_B T} = \rho_P - \frac{2\pi\rho_P}{3k_B T}\int_0^\infty r^3 \frac{dU_{PP}(r)}{dr} g_{PP}(r) dr \ . \tag{5.16}$$

Once the pressures were calculated from eq. (5.16) for a set of two-Yukawa potential parameters, we then compared these $p-\rho-T$ data to the experimental $p-\rho-T$ data [where ρ was obtained from the accurate EOS for the perturber (cf. Table 3.1)]. Once the intermolecular potential parameters yielded thermodynamic data comparable to experiment, we then used these parameters to model the perturber induced shift of the dopant ionization energy. We always began these studies with the two-Yukawa parameters that mimic the Lennard-Jones 6-12 potential [i.e., eqs. (5.13) − (5.15)]. Since the product $\kappa_0\varepsilon$ controls the well-depth, we can adjust ε and hold κ_0 constant (i.e., $\kappa_0 = 8.5000$ Å in the calculations given here). Fig. 5.6 presents the calculated pressure p (open markers) as a function of the perturber number density ρ_P in comparison to the experimental pressures (solid markers) for the density/temperature data sets used in our investigations. Clearly, with the parameters provided in the figure caption, the spherical two-Yukawa potential predicts the thermodynamic behavior quite accurately for both CH_4 and C_2H_6. This accuracy also indicates that the Percus-Yevick radial distribution function calculation with a simple spherical potential is adequately valid for these molecular systems. (We should note that the larger

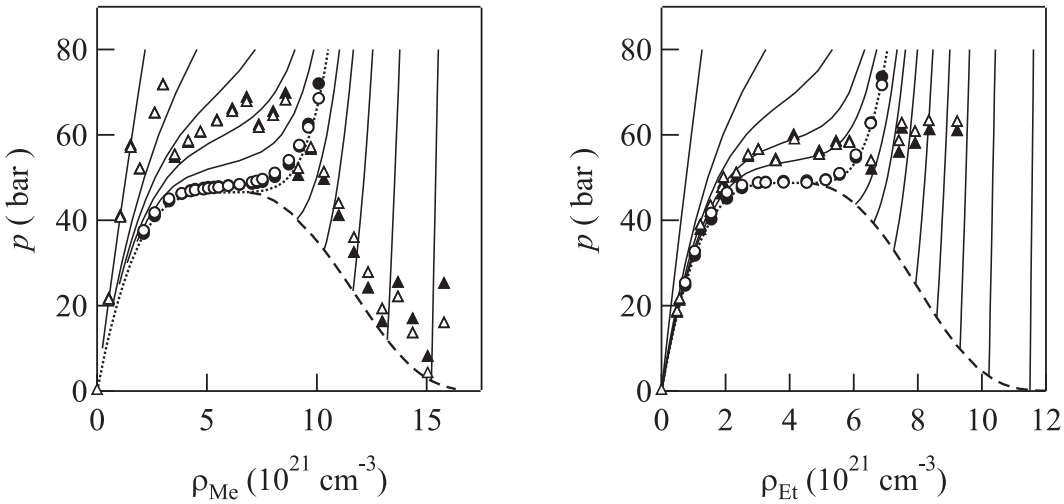

Figure 5.6: The $p-\rho$ phase diagram of (a) CH_4 and (b) C_2H_6 for the equations of state in Table 3.1 showing several non-critical isotherms (—), the critical isotherm ($\cdots$), and the vapor pressure curve (- - -). (▲, •) present thermodynamic conditions for selected non-critical and critical experimental field ionization data, respectively. (△ and ○) present calculated thermodynamic conditions for non-critical temperatures and along the critical isotherm, respectively. The calculated values were obtained from eq. (5.16) with $g_{PP}(r)$ calculated from eqs. (4.1)−(4.3). The two-Yukawa potential parameters for CH_4 are $\sigma_{PP} = 3.500$ Å, $\varepsilon_{PP} = 152.0$ K, $\kappa_0 = 8.500$ Å, $z_1 = 0.847$ Å^{-1}, and $z_2 = 4.000$ Å^{-1}, while those for C_2H_6 are $\sigma_{PP} = 4.015$ Å, $\varepsilon_{PP} = 253.8$ K, $\kappa_0 = 8.500$ Å, $z_1 = 0.685$ Å^{-1}, and $z_2 = 3.500$ Å^{-1}.

error that appears at the high perturber number density region could be caused by the steep isotherms as well as by the failure of the spherical potentials in the higher density regions. We should also like to note here that we have compared the experimental phase diagram and the calculated phase diagram for the atomic perturbers and have achieved fits similar to those shown in Fig. 5.6.)

5.2.3 $\Delta(\rho_P)$ in molecular systems

Once the perturber/perturber intermolecular potential has been determined by the best fit to the thermodynamic equation of state, $\Delta(\rho_P)$ can be fitted to the local

Wigner-Seitz model [i.e., eq. (4.29)], or

$$\begin{aligned}\Delta(\rho_P) &= P_+(\rho_P) + V_0(\rho_P) \\ &= P_+(\rho_P) + P_-(\rho_P) + \frac{3}{2}k_B T + E_k(\rho_P) \\ &= P_+(\rho_P) + P_-(\rho_P) + \frac{3}{2}k_B T + \frac{\hbar^2 \eta_0^2}{2 m_e (r_\ell - |A|)^2} \ .\end{aligned} \tag{5.17}$$

We chose the modified Stockmeyer potential [i.e., eq. (4.5)] in the Lennard-Jones 6-12 potential form [i.e., eq. (4.9)] to simulate the dopant/perturber interaction. The dopant/perturber intermolecular potential parameters along with the scattering length A and the phase shift η_0 were adjusted to give the best fit to the experimental data. Tables 5.2a and 5.2b list all the intermolecular parameters used in calculating the necessary radial distribution functions for $P_+(\rho_P)$, $P_-(\rho_P)$, and $E_k(\rho_P)$. Table 5.2c gives the scattering length A and the phase shift η_0 used in eq. (5.17) to give the best fit to experimental data.

Fig. 5.7a compares the calculated $\Delta(\rho_P)$ [solid lines] to the field ionization results (markers) for TMA in methane and TEA in ethane. Clearly, the calculated $\Delta(\rho_P)$ closely matches experiment, with a scatter that falls within the experimental error of $\pm 0.03 - 0.04$ eV for both systems. The lack of calculated results at the highest methane density is due to our inability to stabilize the RDF calculations at this density. In order to show the trend in $\Delta(\rho_P)$ in ethane, one more calculated point for ethane at the density of 9.6×10^{21} cm^{-3} is presented in the region where field ionization results are unavailable because of the strong ethane absorption band. Fig. 5.7b presents the quasi-free electron energy $V_0(\rho_P)$ obtained within the local Wigner-Seitz model (lines) in comparison to the experimental results (markers). The experimental $V_0(\rho_P)$ are obtained by subtracting the calculated ion/perturber polarization energies $P_+(\rho_P)$

Table 5.2: Parameters used in the local Wigner-Seitz calculation for molecular perturbers.

(a) Dopant and perturber thermodynamic information used to obtain intermolecular potential parameters.

	($Å^3$) α	(D) μ	(K) T_c	(bar) p_c
CH_4	2.593	0	190.56	45.95
C_2H_6	4.45	0	305.33	48.72
TMA	8.15	0.612	433	40.8
TEA	13.1	0.66	535.6	30.3

(b) Intermolecular potentials and parameters used in calculating the radial distribution functions.

	(Å) σ	(K) ε/k_B	(Å) κ_0	($Å^{-1}$) z_1	($Å^{-1}$) z_2
CH_4-CH_4 (TY)	3.300	143.5	8.500	0.900	4.250
C_2H_6-C_2H_6 (TY)	4.015	253.8	8.500	0.685	3.500
TMA-CH_4 (LJ6-12)	6.500	125.0	–	–	–
TEA-C_2H_6 (LJ6-12)	5.100	230.0	–	–	–

(c) The zero-kinetic-energy electron scattering length A and the phase shift η_0 used in the local Wigner-Seitz model calculations for methane and ethane.

Perturber	A (Å)	η_0
CH_4	-0.826 ± 0.004	0.463 ± 0.003
C_2H_6	-1.655 ± 0.005	0.321 ± 0.003

from $\Delta(\rho_P)$, while the calculated $V_0(\rho_P)$ comes directly from eq. (4.28) with the parameters given in Table 5.2c. Similar to the previous photoinjection results [85, 89–91] (cf. Fig. 2.6) at non-critical temperatures, these new field ionization measurements and calculations give a negative $V_0(\rho_P)$ for all methane densities, which indicates the existence of a quasi-free electron in the conduction band of methane at all methane

number densities. $V_0(\rho_P)$ in ethane, on the other hand, is negative at low to medium densities and then becomes positive at densities greater than 8.0×10^{21} cm^{-3}. In order to understand these results, we must investigate the individual components of $V_0(\rho_P)$ and $\Delta(\rho_P)$.

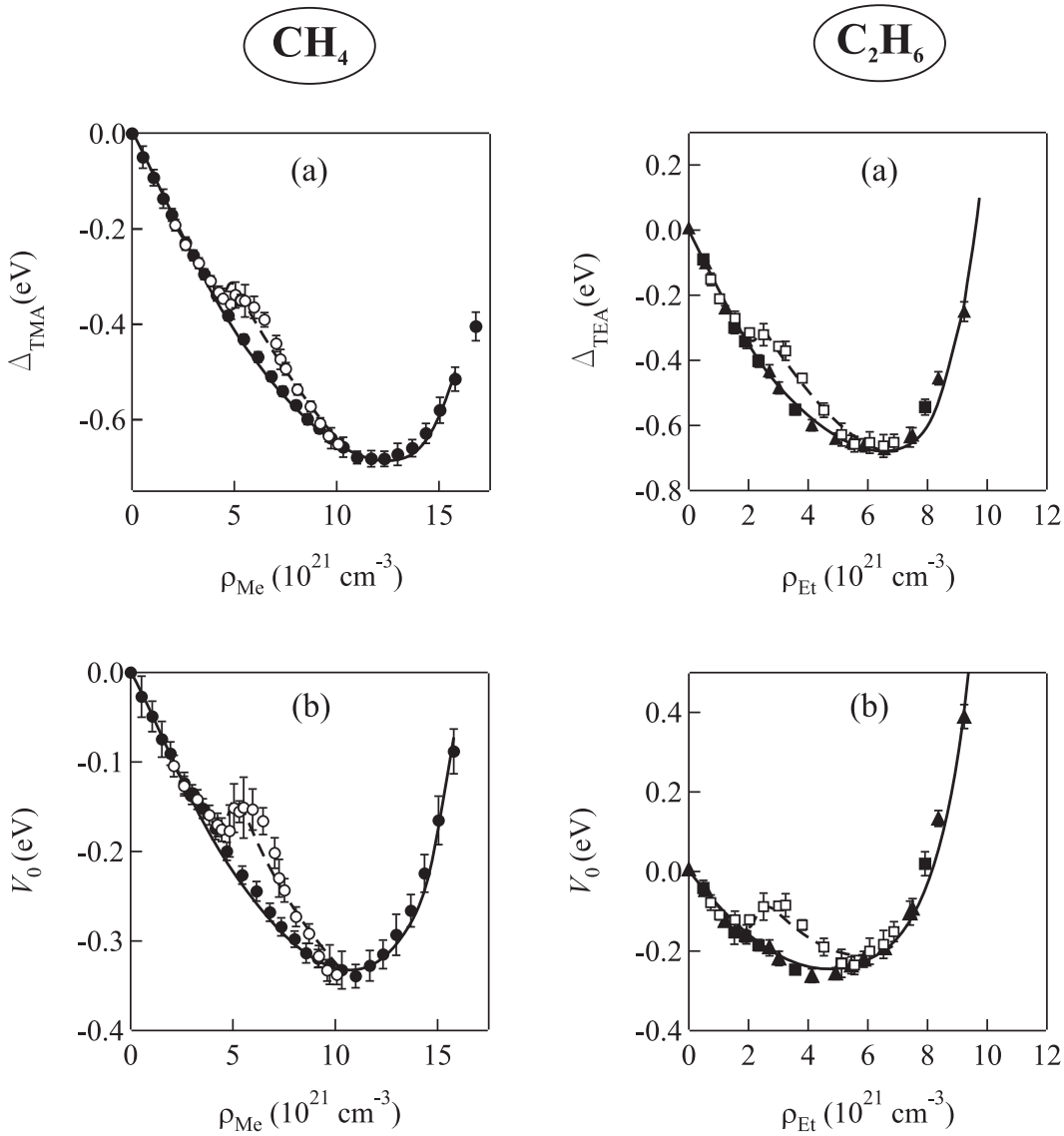

Figure 5.7: Comparison of experiment (markers) and calculation (lines) for (a) the perturber-induced dopant ionization energy $\Delta(\rho_P)$ and (b) the quasi-free electron energy $V_0(\rho_P)$ in CH_4 and C_2H_6 as a function of perturber number density ρ_P. See the legends of Figs. 5.1 and 5.2 for the definition of the markers. The solid line is calculated for various non-critical temperatures; the dashed line is for an isotherm near the perturber critical isotherm. See text for details.

Fig. 5.8 shows the average ion/perturber polarization energy $P_+(\rho_P)$ calculated from eq. (2.41), the average electron/perturber polarization energy $P_-(\rho_P)$ determined from eq. (4.15), and the zero-point kinetic energy $E_k(\rho_P)$ obtained from eq. (4.27) for methane and ethane at non-critical temperatures and on an isotherm near the critical isotherm of the perturber. (All parameters used for these calculations are given in Table 5.2.) One notices in Fig. 5.8a that the average ion/perturber polarization energy is smaller for TMA^+ in methane than for TEA^+ in ethane. When comparing the dopant/perturber intermolecular potential parameters in Table 5.2b, the collision radius σ_{PD} for the TMA/methane interaction is much larger than expected, indicating that the dopant/perturber interaction is relatively small. Since methane is a non-polar solvent while TMA has two lone-pair electrons on the nitrogen atom (suggesting a large polarity), the TMA molecules may be only partially soluble in methane based on the "like dissolves like" rule, thereby leading to the shallow $P_+(\rho_{Me})$. Because the TMA/methane interaction is weak, the well-depth for the intermolecular potential should also be small. For the calculations presented in Figs. 5.7 and 5.8, we chose a well-depth of $\varepsilon_{PD}/k_B = 125.0K$ which ensured stability while calculating the RDFs near the triple point density of methane. On the other hand, since ethane has a much larger polarizability than does methane, the dipole-induced dipole interaction between TEA and ethane is not significantly weaker than the TEA/TEA or ethane/ethane interactions. Therefore, the collision radius σ_{PD} for the TEA/ethane interaction is smaller and the well-depth ε_{PD} is larger than those for the TMA/methane interaction. These stronger dopant/perturber interactions for TEA in ethane lead to the much steeper $P_+(\rho_{Et})$.

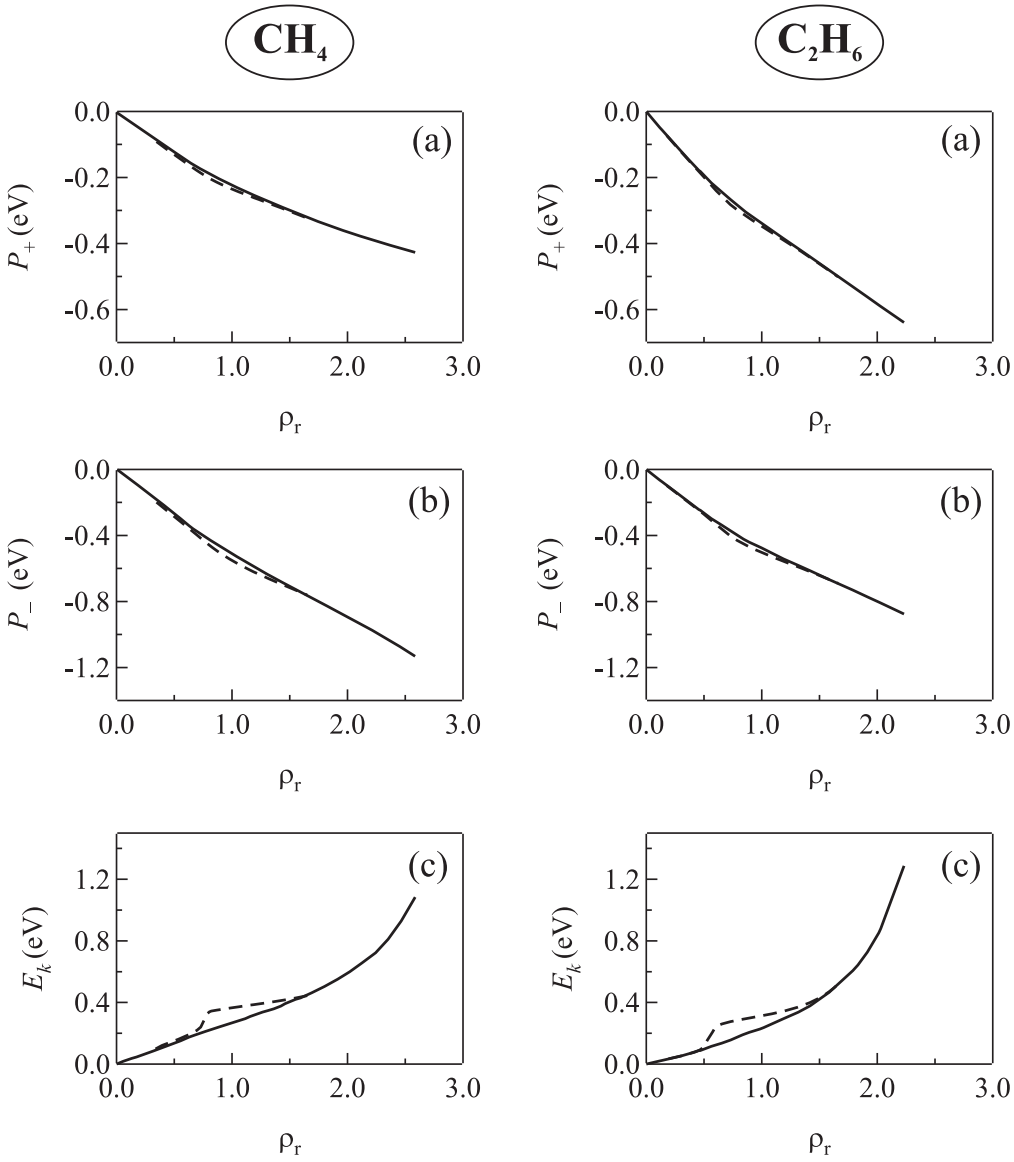

Figure 5.8: The calculated (a) average ion/perturber polarization energies $P_+(\rho_P)$ [i.e., eq. (2.41)], (b) the average electron/perturber polarization energy $P_-(\rho_P)$ [i.e., eq. (4.15)], and (c) the zero-point kinetic energy $E_k(\rho_P)$ [i.e., eq. (4.27)] plotted as a function of the reduced density ρ_r (i.e., $\rho_r = \rho_P/\rho_c$, where the critical density ρ_c is 6.11 $\times 10^{21}$ cm^{-3} for methane and 4.14 $\times 10^{21}$ cm^{-3} for ethane) in methane and ethane at non-critical temperatures (—) and on an isotherm near the critical isotherm (- - -) of the perturber. The calculation parameters are listed in Table 5.2. See text for discussion.

On the other hand, the average electron/perturber polarization energy shown in Fig. 5.8b is slightly larger in methane than in ethane. The electron/perturber polarization energy is dominated by the perturber/perturber interactions. As one would expect, the induced dipole/induced dipole interactions in methane are weaker than those in ethane. Thus, the well depth for methane is smaller than that for ethane. The overall size of the electron/perturber polarization energy is dominated by the collision radius, which gives the most probable distance between perturber molecules. A small radius indicates that the perturbers can pack closer together at higher densities. This, in turn, increases the local density (cf. Fig. 5.9, for example, as discussed below), which gives a larger shift in the electron/perturber polarization energy.

The zero-point kinetic energy $E_k(\rho_P)$ of the quasi-free electron, shown as a function of perturber number density in Fig. 5.8c, is dependent on the local density within the first solvent shell through the local Wigner-Seitz radius [i.e., eq. (4.22)]. Fig. 5.9 presents the maximum local density in the first solvent shell (i.e., $\rho_{loc} = g_{max}\rho_P$) plotted as a function of reduced perturber number density. Fig. 5.9 clearly indicates that the local density within the first solvent shell is larger for methane than for ethane, which is not surprising given the size difference of these two molecules. However, $E_k(\rho_P)$ increases more for ethane than for methane at high perturber number densities (cf. Fig. 5.8c). This increase in $E_k(\rho_P)$ is caused by the larger electron scattering length in ethane. The electron scattering length represents the minimum distance between the electron and a single perturber, while the local Wigner-Seitz radius represents the maximum distance between the electron and a single perturber.

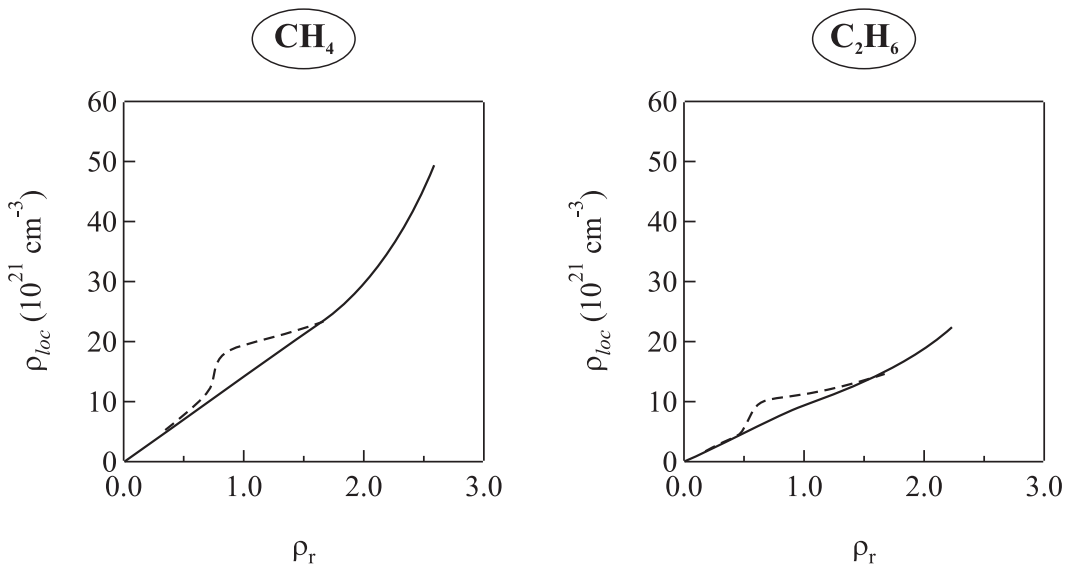

Figure 5.9: The calculated local density ρ_{loc} plotted as a function of ρ_r in (a) methane and (b) ethane at non-critical temperatures (—) and on an isotherm near the critical isotherm (- - -) of the perturber. See text for discussion.

Thus, the difference between these two numbers is the size of the "box" in which the quasi-free electron is confined during the electron/perturber interaction. At higher perturber number densities, the electron/ethane interaction box size is smaller and, therefore, the zero-point kinetic energy of the electron is larger in ethane. Fig. 5.8 also clearly shows those effects which are dominant near the critical point. The ensemble average polarization energies $P_+(\rho_P)$ and $P_-(\rho_P)$ show only a slight difference near the perturber critical point. The zero-point kinetic energy $E_k(\rho_P)$, on the other hand, has a significant critical point effect. Similar to the atomic perturber systems, this variation in $E_k(\rho_P)$ is caused by local density fluctuations in the critical point region (cf. Fig. 5.9).

Since field ionization measurements in CF_4 are problematic (cf. Fig. 5.3), we used the local Wigner-Seitz model to predict the quasi-free electron energy $V_0(\rho_P)$ for CF_4. The CF_4/CF_4 interaction was modeled using the two-Yukawa potential with

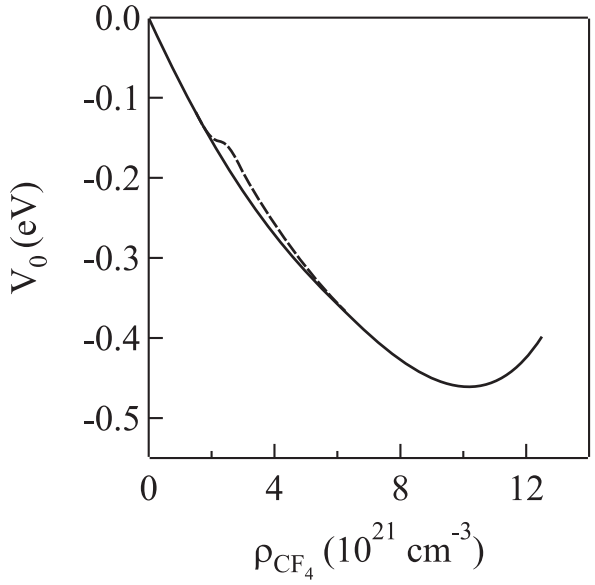

Figure 5.10: The calculated quasi-free electron energy $V_0(\rho_P)$ in CF_4 as a function of perturber number density ρ_P at various non-critical temperatures (—) and along an isotherm of $-45.0°C$ (- - -) near the CF_4 critical temperature of $-45.6°C$.

the parameters $\sigma_{PP} = 4.194$ Å, $\varepsilon_{PP} = 203.6$ K, $\kappa_0 = 8.500$ Å, $z_1 = 0.707$ Å^{-1}, and $z_2 = 3.342$ Å^{-1}. Again, these parameters were obtained by fitting to the reference equations of state (i.e., the extended Benedict-Webb-Rubin EOS [128] for $T \geq T_c$ and the Peng-Robinson EOS [129] for $T < T_c$). The electron scattering length $A = -0.95$ Å and the phase shift $\eta_0 = 0.37$ for calculating $E_k(\rho_P)$ [i.e., eq. (4.27)] were chosen in order (i) to optimize the fit to the field ionization result of CH_3I in low density CF_4 ($\rho_P < 1.5 \times 10^{21}$ cm^{-3} in Fig. 5.3a), and (ii) to ensure that $V_0(\rho_P)$ is negative for all perturber densities. (We should note that we used the CH_3I/CF_4 ground state intermolecular potential parameters that were validated in modeling the lineshapes of low-n CH_3I Rydberg states in CF_4 [130] to calculate $P_+(\rho_P)$ at low-to-medium CF_4 number densities.).

Fig. 5.10 presents the calculated $V_0(\rho_P)$ in CF_4 at various non-critical temperatures and along an isotherm near the critical isotherm. Clearly, the $V_0(\rho_P)$ critical point

effect in CF_4 is much smaller than that for methane or ethane. A similar difference was also observed in the shift of the CH_3I low-n Rydberg states in CF_4 [130] in comparison to those in methane. One obvious reason for these smaller critical effects is the fact that CF_4 has a smaller critical density (i.e., $\rho_{CF_4} = 4.3 \times 10^{21}$ cm^{-3}) in comparison to that of methane (i.e., $\rho_{CH_4} = 6.1 \times 10^{21}$ cm^{-3}). The low density turning point in the CF_4 critical isotherm, which demarks the beginning of the critical effect, is at a density of 2.0×10^{21} cm^{-3}. The lower bulk density gives a lower local density and, therefore, a larger local radius. The larger local radius near the critical point of CF_4 implies a larger electron/perturber interaction box and, therefore, a smaller zero-point kinetic energy $E_k(\rho_P)$. Since $E_k(\rho_P)$ dominates the critical point effect, the observed critical effect in $V_0(\rho_P)$ for CF_4 is also small.

Chapter 6

Conclusion

In this work, perturber effects on the dopant ionization energy and the quasi-free electron energy have been studied both experimentally and theoretically. Field ionization results in various dopant/perturber systems were presented, and the local Wigner-Seitz model was developed and tested. We first recorded a temperature dependence of the perturber induced shift $\Delta(\rho_{\mathrm{P}})$ for CH_3I in low density Ar and Kr, which contradicted the standard low density model. We then presented the field ionization of various dopants (i.e., CH_3I, C_2H_5I, N,N-dimethylanaline and trimethylamine) in atomic perturbers (i.e., Ar, Kr and Xe) from low density to the densities of the respective triple point liquids, at non-critical temperatures and on isotherms near the respective critical isotherms. The decrease in $\Delta(\rho_{\mathrm{P}})$ near the perturber critical point was observed and explained within the local Wigner-Seitz model. Field ionization measurements of trimethylamine in methane and triethylamine in ethane were then used to extend the local Wigner-Seitz model to molecular systems.

In the local Wigner-Seitz model, the perturber induced shift $\Delta(\rho_{\mathrm{P}})$ of the dopant ionization energy is the sum of the average ion/perturber polarization energy $P_{+}(\rho_{\mathrm{P}})$ and the quasi-free electron energy $V_0(\rho_{\mathrm{P}})$. The quasi-free electron energy arises from the electron/perturber interaction and consists of the electron/perturber polarization

energy $P_{-}(\rho_{\mathrm{P}})$, the electron zero-point kinetic energy $E_k(\rho_{\mathrm{P}})$ and a small thermal correction term $(3/2)k_B\,T$. We demonstrated that the temperature dependence of $\Delta(\rho_{\mathrm{P}})$ observed in low density Ar and Kr was caused solely by dopant/perturber interactions and, therefore, is not correctly accounted for in the low density Fermi-Alekseev-Sobel'man model. $\Delta(\rho_{\mathrm{P}})$ in the low density Fermi-Alekseev-Sobel'man model is given by the sum of the shift $\Delta_{sc}(\rho_{\mathrm{P}})$ resulting from scattering of the optical electron off of the perturber and the shift $\Delta_{pol}(\rho_{\mathrm{P}})$ due to the polarization of the perturber by the dopant core. Since $\Delta_{pol}(\rho_{\mathrm{P}})$ neglects the fluid structure and only accounts for the polarization of the perturbers outside a fixed radius (i.e., the Wigner-Seitz radius r_s in the original Fermi model and the Weisskopf radius r_w in the Alekseev-Sobel'man model), it is always underestimated. This underestimation of $\Delta_{pol}(\rho_{\mathrm{P}})$ is counterbalanced by the overestimation of $\Delta_{sc}(\rho_{\mathrm{P}})$ in order to fit the experimental data at low perturber densities. Therefore, the electron scattering length A obtained from the low density model [i.e., eq. (2.26)] tends to be overestimated, especially for perturbers having high critical temperatures. Our calculations indicated that as the temperature decreases, the local perturber density in the first solvent shell around the dopant increases slightly. This, in turn, leads to the temperature dependence observed in $\Delta(\rho_{\mathrm{P}})$. The temperature dependence of $\Delta(\rho_{\mathrm{P}})$ can lead to significant overestimates of the electron scattering length obtained from the low density Fermi-Alekseev-Sobel'man model. Thus, the scattering lengths from the Fermi-Alekseev-Sobel'man model should always be compared to data obtained from other experimental methods, such as electron swarm methods.

A principal experimental result presented in this work is the clear decrease in $\Delta(\rho_{\mathrm{P}})$ (smaller red shift) near the perturber critical point. We showed that although both $P_{+}(\rho_{\mathrm{P}})$ and $P_{-}(\rho_{\mathrm{P}})$ become more negative near the critical point, the increase in the zero-point kinetic energy $E_k(\rho_{\mathrm{P}})$ dominates. A short-ranged potential $V_{loc}(r)$ with a total range of $r_b = r_l - |A|$ (where $|A|$ is the electron scattering length representing the minimum distance between the optical electron and a single perturber while the local radius r_l serves as the maximum distance for an electron interacting with a single perturber in the fluid) is introduced to account for the local dynamic polarization of a perturber by the optical electron. At the critical point, the local density increases because of increased perturber/perturber correlations. The increase in local density results in a decrease in the local radius r_l, which decreases r_b (the translational boundary condition for the quasi-free electron wavefunction) and, therefore, increases the electron zero-point kinetic energy $E_k(\rho_{\mathrm{P}})$. Using the local Wigner-Seitz model, we calculated $\Delta(\rho_{\mathrm{P}})$ to within experimental error for all temperatures and perturber densities in Ar, Kr and Xe. The critical effect in Xe appears to be the largest among the attractive rare gases, which is due to its large atomic size, indicating a large electron scattering length $|A|$.

Our studies of attractive atomic systems also indicated that the dynamic perturber polarization caused a phase shift in the quasi-free electron wave function. Including this phase shift η_0 is essential for the local Wigner-Seitz model. Without the phase shift η_0, the quasi-free electron Schrödinger equation can only be solved with the boundary condition

$$\psi(|A|) = 0 \ , \quad \left(\frac{\partial \psi}{\partial r}\right)\bigg|_{r=r_l} = \ 0 \ . \tag{6.1}$$

Since r_l is fixed for a given temperature and perturber bulk density, an accurate and consistent fit to the experimental results becomes impossible. For example, to fit the experimental field ionization results for Ar without the phase shift η_0 requires an electron scattering length of -0.27 Å, which is significantly smaller than the scattering length of -0.89 Å obtained from electron swarm methods. In atomic systems (e.g., Ar, Kr and Xe), η_0 is predominately determined by the polarizability of the perturber, with larger polarizabilities yielding smaller phase shifts. Another possible explanation is that a smaller electron density in the valence shell of the perturber atom (caused by the same number of valence electrons spread over the larger surface area within a semi-classical approximation) leads to a smaller phase shift during interaction with the quasi-free electron. This implies that the quasi-free electron is sensitive to the perturber structure, which also indicates that the low-energy scattering assumption of Alekseev and Sobel'man is no longer valid, especially at high perturber number densities, where $E_k(\rho_{\text{P}})$ is large.

In molecular systems (e.g., CH_4, C_2H_6 and CF_4), the phase shift η_0 does not decrease as dramatically as it does for the atomic perturbers. However, the phase shift does decrease with increasing molecular size (and decreasing electron density in the valence shell). This smaller change in η_0 is probably caused by the non-uniform electron density in molecular perturbers, which complicates the modeling of electron/molecular fluid interactions. This complexity is handled by the adjustable η_0. Nevertheless, to fully understand the influence of molecular structure on the phase shift, additional molecular systems will need to be investigated, including polar fluids and linear systems. However, we showed that a spherically symmetric intermolecular

potential (i.e., the two-Yukawa potential) was adequate to model the molecular fluids studied here, by calculating the equation of state for each system using our parameters. In comparison to the standard Lennard-Jones 6-12 potential for methane and ethane, the two-Yukawa potential yielded shorter equilibrium distances (indicating larger perturber/perturber interactions), a larger well-depth (implying a larger temperature sensitivity) and a larger attractive tail (implying a longer correlation length). These features are required to model accurately the critical isotherm in the equation of state, and they serve to enhance the local density in the first solvent shell. This enhancement of the local density, in turn, is essential to generate the huge increase in $E_k(\rho_{\rm P})$ observed near the critical point in molecular perturbers.

In conclusion, this work has led to an increased understanding of the interaction between a quasi-free electron and a perturbing fluid in simple systems. The next step will be to expand our understanding into more complex solvents, including solvents that can trap the electron (i.e., repulsive fluids) and polar solvents. Thus, future studies will include the measurement of the quasi-free electron energy in repulsive rare gases (i.e., He and Ne), which have recently been begun by us, as well as continued investigations of the quasi-free electron energy in molecular fluids. The extension of the local Wigner-Seitz model into repulsive systems must be verified. From the knowledge obtained in the present dissertation, the average polarization energy $P_+(\rho_{\rm P})$ and $P_-(\rho_{\rm P})$ in He and Ne is projected to be small. Thus, to maintain a positive quasi-free electron energy over the entire density range will require that $E_k(\rho_{\rm P})$ overwhelm $P_+(\rho_{\rm P})$ and $P_-(\rho_{\rm P})$ even at low perturber number densities. This indicates either a large scattering length (which is ruled out by earlier research), or a large η_0. A large

η_0 would agree with our current results in atomic systems. In terms of the intermolecular potential, the Lennard-Jones potential should still be valid for the atomic gases He and Ne. However, in future studies involving polar molecules (e.g., CO), angle dependent potentials with dipole-dipole interaction terms must be introduced. This will require changing the calculation of the radial distribution functions, as well as the integrals for the polarization energies $P_+(\rho_{\mathrm{P}})$ and $P_-(\rho_{\mathrm{P}})$. Finally, understanding the relationship between η_0 and molecular structure will require work with additional perturbers having a variety of molecular structures, like linear perturbers and cyclical perturbers. These studies will require a change in the experimental system, since many of the more complex molecular structures have higher critical temperatures and pressures.

References

[1] O. Kajimoto, "Solvation in supercritical fluids: its effects on energy transfer and chemical reactions," Chem. Rev. 99, 355 (1999), and references therein.

[2] S.C. Tucker, "Solvent density inhomogeneities in supercritical fluids," Chem. Rev. 99, 391 (1999), and references therein.

[3] A. M. Köhler, *Density Effects on Rydberg States and Ionization Energies of Molecules*, Ph.D. Dissertation, Universität Hamburg, Hamburg, Germany, 1987, and references therein.

[4] A. K. Al-Omari, *Field Ionization as a Technique to Determine Electronic Properties of Fluids*, Ph.D. dissertation, University of Wisconsin Madison, Madison, WI, 1996, and references therein.

[5] C. M. Evans, *Subthreshold Photoionization in Molecular Dopant/perturber Systems*, Ph.D. dissertation, Louisiana State University, 2001, and references therein. See also C. M. Evans, J. D. Scott, G. L. Findley, Rec. Res. Dev. Chem. Phys. 3, 351 (2002).

[6] I. I. Sobel'man, L. A. Vainshtein, E. A. Yukov, *Excitation of Atoms and Broadening of Spectral Lines* (Springer-Verlag, Berlin, 1995).

[7] J. Meyer, *Elektronische Eigenschaften Dotierter Gase und Flüssigkeiten* (Electronic Properties of Dense Gases and Liquids), Ph.D. dissertation, Universität Hamburg, 1992, and references therein.

[8] T. F. Gallagher, *Rydberg Atoms* (Cambridge Univ. Press, Cambridge, 1994), and references therein.

[9] S. Basak, M. H. Cohen, "Deformation-potential theory for the mobility of excess electrons in liquid argon," Phys. Rev. B 20, 3404 (1979).

[10] A. F. Borghesani, L. Bruschi, M. Santini, G. Torzo, "Electron mobility in neon at high densities," Phys. Rev. A 37, 4828 (1988).

[11] A. F. Borghesani, M. Santini, "Excess electron mobility in high-density argon gas," P. Lamp, Phys. Rev. A 46, 7902 (1992).

[12] A. F. Borghesani, M. Santini, "Electron mobility maximum in near-critical argon gas," Int. J. Thermophys. 22, 1109 (2001).

[13] M. Nishikawa, K. Itoh, R. A. Holroyd, "Effect of pressure on the reaction of electrons with CO_2, in nonpolar solvents," J. Phys. Chem. 92, 5262 (1988).

[14] K. Itoh, R. A. Holroyd, "Electron attachment to benzene and toluene in nonpolar solvents at high pressure," J. Phys. Chem. 94, 8854 (1990).

[15] E. Fermi, "Sopra lo spostamento per pressione delle righe elevate delle serie spettrali (Concerning the shift of the high lines of spectral series due to pressure effects)," Nuovo Cimento 11, 157 (1934).

[16] E. Amaldi, E. Segrè, "Effetto della pressione sui termini elevati degli alcalini (Effect of pressure on the high terms of alkaline metals)," Nuovo Cimento 11, 145 (1934).

[17] H. Margenau, W. W. Watson, "Pressure effects on spectral lines," Rev. Mod. Phys. 8, 22 (1936).

[18] A. M. Köhler, R. Reininger, V. Saile, G. L. Findley, "Density effects on high-n molecular Rydberg states: CH_3I in argon," Phys. Rev. A 33, 771 (1986).

[19] A. M. Köhler, R. Reininger, V. Saile, G. L. Findley, "Density effects on high-n molecular Rydberg states: CH_3I in He, Ne, Ar and Kr," Phys. Rev. A 35, 79 (1987).

[20] E. Wigner, F. Seitz, "On the constitution of metallic sodium," Phys. Rev. 43, 804 (1933).

[21] E. Wigner, F. Seitz, "On the constitution of metallic sodium. II," Phys. Rev. 46, 509 (1934).

[22] V. A. Alekseev, I. I. Sobel'man, "A spectroscopic method for the investigation of elastic scattering of slow electrons," Zh. Eksp. Teor. Fiz. 49, 1274 (1965). [Sov. Phys. - JETP 22, 882 (1966)].

[23] V. Weisskopf, "Zur Theorie der Kopplungsbreite und der Stoßdämpfung (On the theory of coupling width and impact damping)," Z. Phys. 75, 287; "Zur Theorie der Kopplungsbreite (On the theory of coupling width)," Z. Phys. 77, 398 (1932).

[24] V. Weisskopf, "Die Breite der Spektrallinien in Gasen (The width of spectral lines in gases)," Phys. Z. 34, 1 (1933).

[25] A. M. Köhler, V. Saile, R. Reininger, G. L. Findley, "Sudden and adiabatic polarization effects in doped rare gases," Phys. Rev. Lett. 60, 2727 (1988); errata 61, 1327 (1988).

[26] Xianbo Shi, Luxi Li, Gina M. Moriarty, C. M. Evans, G. L. Findley, "Energy of the quasi-free electron in low density Ar and Kr: extension of the local Wigner-Seitz model," Chem. Phys. Lett. 454, 12 (2008).

[27] A. K. Al-Omari, R. Reininger, D. L. Huber, "Polarization energy distribution for impurity molecules in dense gases," J. Chem. Phys. 109, 7663 (1998).

[28] T. Z. Ny, S. Y. Ch'en, "The displacement of principal series lines of rubidium by the addition of rare gases," Phys. Rev. 51, 567 (1937).

[29] T. Z. Ny, S. Y. Ch'en, "Pressure shifts of the high terms of the absorption series of Na, Rb, and Cs produced by hydrogen and nitrogen," Phys. Rev. 54, 1045 (1938).

[30] C. Füchtbauer, W. V. Heesen, "Verbreiterung und Verschiebung von mittleren und höheren Kaliumserienlinien durch Helium von hohem Druck (Broadening and displacement of the middle and higher potassium series lines produced by helium at high pressure)," Z. Phys. 113, 323 (1939).

[31] C. Füchtbauer, G. Hansler, "Dichteabhängigkeit der Verschiebung hoher Alkaliserienlinien durch Fremdgase (Density-dependent shift of high alkali series-lines due to foreign gases)," Phys. Z. 41, 555 (1940).

[32] C. Füchtbauer, H. J. Reimers, "Störung hoher Caesiumterme durch Grenzkohlenwasserstoffe und Messungen am Dublett $1s$-$3p$ der Kaliumhauptserie (Perturbation of higher cesium terms through paraffin hydrocarbons and measurements on the $1s$-$3p$ doublet of the principal series of potassium)," Z. Phys. 97, 1 (1935).

[33] D. K. L. Tan, S. Y. Ch'en, "Pressure effects of foreign gases on the absorption lines of cesium. VII. The shift of high-member lines by various rare gases," Phys. Rev. A 2, 1124 (1970).

[34] K. H. Weber, K. Niemax, "Impact broadening and shift of Rb nS and nD levels by noble gases," Z. Phys. A. 307, 13 (1982).

[35] K. H. Weber, K. Niemax, "Impact broadening of Sr $5sns\ ^1S_0$, $5snd\ ^1D_2$ and $5snd\ ^3D_2$ levels by He and Xe," Z. Phys. A. 309, 19 (1982).

[36] I. T. Steinberger, U. Asaf, G. Ascarelli, R. Reininger, G. Reisfeld, M. Reshotko, "Extrinsic photoconduction and Rydberg states due to a methyl iodide impurity in xenon," Phys. Rev. A 42, 3135 (1990).

[37] U. Asaf, W. S. Felps, K. Rupnik, S. P. McGlynn, G. Ascarelli, "Density effects on high-n molecular Rydberg states: CH_3I and C_6H_6 in H_2 and Ar," J. Chem. Phys. 91, 5170 (1989).

[38] U. Asaf, J. Meyer, R. Reininger, I. T. Steinberger, "High Rydberg states of methyl iodide perturbed by nitrogen: a mutual cancellation of shift terms," J. Chem. Phys. 96, 7885 (1992).

[39] J. Meyer, R. Reininger, U. Asaf, I. T. Steinberger, "Autoionization spectra of CH_3I in dense gaseous methane, ethane, and propane observed by photoconduction," J. Chem. Phys. 94, 1820 (1991).

[40] U. Asaf, I. T. Steinberger, J. Meyer, R. Reininger, "Electron scattering in dense CO_2 gas: photoionization spectra of CH_3I perturbed by carbon dioxide," J. Chem. Phys. 95, 4070 (1991).

[41] J. Meyer, R. Reininger, U. Asaf, "Spectral shift of autoionizing high-n Rydberg states of iodomethane in dense argon: a photoionization study," Chem. Phys. Lett. 173, 384 (1990).

[42] C. M. Evans, G. L. Findley, "Energy of the quasifree electron in argon and krypton," Phys. Rev. A 72, 022717 (2005).

[43] C. M. Evans, G. L. Findley, "Energy of the quasi-free electron in supercritical argon near the critical point," Chem. Phys. Lett. 410, 242 (2005).

[44] C. M. Evans, G. L. Findley, "Field ionization of C_2H_5I in supercritical argon near the critical point," J. Phys. B: At. Mol. Opt. Phys. 38, L269 (2005).

[45] Luxi Li, C. M. Evans, G. L. Findley, "Energy of the quasi-Free electron in supercritical krypton near the critical point," J. Phys. Chem. A 109, 10683 (2005).

[46] Xianbo Shi, Luxi Li, C. M. Evans, G. L. Findley, "Energy of the quasi-free electron in xenon," Chem. Phys. Lett. 432, 62 (2006).

[47] Xianbo Shi, Luxi Li, C. M. Evans, G. L. Findley, "Energy of the quasi-free electron in argon, krypton and xenon," Nucl. Inst. Meth. A 582, 270 (2007).

[48] I. Messing, J. Jortner, "Adiabatic polarization energy in a simple dense fluid," Chem. Phys. 24, 183 (1977).

[49] J. Lekner, "Motion of electrons in liquid argon," Phys. Rev. 158, 130 (1967).

[50] A. K. Al-Omari, K. N. Altmann, R. Reininger, "Determination of the conduction band energy minimum in fluid argon by means of field ionization," J. Chem. Phys. 105, 1305 (1996).

[51] A. K. Al-Omari, R. Reininger, "Density dependence of the ionization of H_2S in argon," J. Electron Spectrosc. Relat. Phenom. 79, 463 (1996).

[52] A. K. Al-Omari, R. Reininger, "Density dependence of the ionization potential of CH_3I in krypton and of the quasi-free electron energy in krypton," J. Chem. Phys. 103, 4484 (1995).

[53] A. K. Al-Omari, R. Reininger, "Density dependence of the ionization potential of CH_3I in argon and of the quasi-free electron energy in argon," J. Chem. Phys. 103, 506 (1995).

[54] A. K. Al-Omari, R. Reininger, D. L. Huber, "Polarization energy distribution of a positive ion in liquid argon," Phys. Rev. Lett. 74, 820 (1995).

[55] J. G. Kirkwood, "Statistical mechanics of fluid mixtures," J. Chem. Phys. 3, 300 (1935).

[56] B. E. Springett, J. Jortner, M. H. Cohen, "Stability criterion for the localization of an excess electron in a nonpolar fluid," J. Chem. Phys. 48, 2720 (1968).

[57] B. Plenkiewicz, P. Plenkiewicz, J. -P. Jay-Gerin, "Conduction-band energy V_0 of an excess electron in liquid krypton," Phys. Rev. A. 39, 2070 (1989).

[58] B. Plenkiewicz, J. -P. Jay-Gerin, P. Plenkiewicz, G. B. Bachelet, "Conduction band energy of excess electrons in liquid argon," Europhys. Lett. 1, 455 (1986).

[59] B. Plenkiewicz, P. Plenkiewicz, J. -P. Jay-Gerin, "Density dependence of the conduction-band energy of excess electrons in liquid argon," Phys. Rev. A 40, 4113 (1989).

[60] B. Plenkiewicz, P. Plenkiewicz, J. -P. Jay-Gerin, "Calculation of the conduction-band energy of excess electrons in fluid helium," Chem. Phys. Lett. 163, 542 (1989).

[61] B. Plenkiewicz, Y. Frongillo, P. Plenkiewicz, J. -P. Jay-Gerin, "Density dependence of the conduction-band energy and of the effective mass of quasifree excess electrons in fluid neon and helium," Phys. Rev. A 43, 7061 (1991).

[62] Y. Frongillo, B. Plenkiewicz, J. -P. Jay-Gerin, "Density dependence of the conduction-band energy V_0 of excess electrons in fluid xenon," Phys. Rev. E 53, 5506 (1996).

[63] B. Plenkiewicz, Y. Frongillo, J. -M. Lopez-Castillo, J. -P. Jay-Gerin, "A simple but accurate 'core-tail' pseudopotential approach to the calculation of the conduction-band energy V_0 of quasifree excess electrons and positrons in nonpolar fluids," J. Chem. Phys. 104, 9053 (1996).

[64] B. Plenkiewicz, P. Plenkiewicz, J. -P. Jay-Gerin, A. K. Jain, "Density dependence of the ground-state energy of excess electrons in liquid methane," J. Chem. Phys. 90, 4907 (1989).

[65] Y. Frongillo, B. Plenkiewicz, J. -P. Jay-Gerin, A. Jain, "Comparison of quasifree excess electron and positron states in simple molecular fluids: methane and silane," Phys. Rev. E 50, 4754 (1994).

[66] G. B. Bachelet, D. R. Hamann, M. Schlüter, "Pseudopotentials that work: from H to Pu," Phys. Rev. B 26, 4199 (1982).

[67] V. M. Atrazhev, I. T. Iakubov, "Thermal electrons in liquids with high polarizability," J. Chem. Phys. 103, 9030 (1995).

[68] I. T. Iakubov, "Effective mass of an excess electron in fluids with high polarizability," Chem. Phys. Lett. 240, 589 (1995).

[69] I. T. Steinberger, R. Reininger, "Comment on 'Effective mass of an excess electron in fluids with high polarizability'," Chem. Phys. Lett. 258, 680 (1996).

[70] I. T. Iakubov, "Reply to Comment on 'Effective mass of an excess electron in fluids with high polarizability'," Chem. Phys. Lett. 258, 682 (1996).

[71] P. Stampfli, K. H. Bennemann, "Theoretical results for the density dependence of the electron affinity of nonpolar liquids Ar, Kr and Xe," Phys. Rev. A 44, 8210 (1991).

[72] S. H. Simon, V. Dobrosaljević, M. R. Stratt, "Semiclassical percolation approach to electronic states in simple fluids," Phys. Rev. A 42, 6278 (1990).

[73] S. H. Simon, V. Dobrosaljević, M. R. Stratt, "The mobility of electrons in simple insulating fluids as a percolation problem," J. Chem. Phys. 94, 7360 (1991).

[74] J. -M. Lopez-Castillo, Y. Frongillo, B. Plenkiewicz, J. -P. Jay-Gerin, "Path-integral molecular-dynamics calculation of the conduction-band energy minimum V_0 of excess electrons in fluid argon," J. Chem. Phys. 96, 9092 (1992).

[75] X. -P. Li, J. Q. Broughton, P. B. Allen, "Electron-inert gas pseudopotentials for use in path integral simulations," J. Chem. Phys. 85, 3444 (1986).

[76] J. -M. Lopez-Castillo, J. -P. Jay-Gerin, "Multiple-scattering theory of excess electrons in simple fluids," Phys. Rev. E 52, 4892 (1995).

[77] B. Space, D. F. Coker, Z. H. Liu, B. J. Berne, G. Martyna, "Density dependence of excess electronic ground-state energies in simple atomic fluids," J. Chem. Phys. 97, 2002 (1992).

[78] B. Boltjes, C. de Graaf, S. W. de Leeuw, "Computation of the energy V_0 of an excess electron in dense helium and argon," J. Chem. Phys. 98, 592 (1993).

[79] P. E. Siska, "One-electron model potential calculations of van der Waals forces. I. He^* ($2\ ^1S$, $2\ ^3S$) + Ne, Ar, Kr, Xe," J. Chem. Phys. 71, 3942 (1979).

[80] R. Reininger, U. Asaf, I. T. Steinberger, S. Basak, "Relationship between the energy V_0 of the quasi-free-electron and its mobility in fluid argon, krypton, and xenon," Phys. Rev. B 28, 4426 (1983).

[81] R. Reininger, U. Asaf, I. T. Steinberger, "The density dependence of the quasi-free electron state in fluid xenon and krypton," Chem. Phys. Lett. 90, 287 (1982).

[82] A. O. Allen, W. F. Schmidt, "Determination of the energy level V_0 of electrons in liquid argon over a range of densities," Z. Naturforsch. 37a, 316 (1982).

[83] W. von Zdrojewski, J. G. Rabe, W. F. Schmidt, "Photoelectric determination of V_0-values in solid rare gases," Z. Naturforsch. 35a, 672 (1980).

[84] B. Halpern, J. Lekner, S. A. Rice, R. Gomer, "Drift velocity and energy of electrons in liquid argon," Phys. Rev. 156, 351 (1967).

[85] W. Tauchert, H. Jungblut, W. F. Schmidt, "Photoelectric determination of V_0 values and electron ranges in some cryogenic liquids," Can. J. Chem. 55, 1860 (1977).

[86] J. R. Broomall, W. D. Johnson, D. G. Onn, "Density dependence of the electron surface barrier for fluid helium-3 and helium-4," Phys. Rev. B 14, 2819 (1976).

[87] J. Jortner, A. Gaathon, "Effects of phase density on ionization processes and electron localization in fluids," Can. J. Chem. 55, 1801 (1977).

[88] N. Schwetner, E. -E. Koch, J. Jortner, *Electronic Excitations in Condensed Rare Gases* (Springer-Verlag, Berlin, 1985), p.75.

[89] U. Asaf, R. Reininger, I. T. Steinberger, "The energy V_0 of the quasi-free electron in gaseous, liquid and solid methane," Chem. Phys. Lett. 100, 363 (1983).

[90] Y. Yamaguchi, T. Nakajima, M. Nishikawa, "Conduction band energy in dense ethane fluid," J. Chem. Phys. 71, 550 (1979).

[91] S. Noda, L. Kevan, K. Fueki, "Conduction state energy of excess electrons in condensed media. Liquid methane, ethane, and argon and glassy matrices," J. Phys. Chem. 79, 2866 (1975).

[92] K. Nakagawa, K. Ohtake, M. Nishikawa, "Conduction band energy in dense propane fluid," J. Electrostat. 12, 157 (1982).

[93] K. Nakagawa, K. Itoh, M. Nishikawa, "The effect of molecular structure on the density dependence of electron mobility and conduction band energy in nonpolar fluids," IEEE Trans. Elect. Insul. 23, 509 (1988).

[94] R. A. Holroyd, N. E. Cipollini, "Dependence of conduction band energy and electron mobility on fluid density," Proc. 6th Int. Conf. Radiation Research, 228, Toppan, Tokyo, 1979.

[95] R. A. Holroyd, M. Allen, "Energy of excess electrons in nonpolar liquids by photoelectric work function measurements," J. Chem. Phys. 54, 5014 (1971).

[96] R. A. Holroyd, R. L. Russell, "Solvent and temperature effects in the photoionization of tetramethyl-p-phenylenediamine," J. Phys. Chem. 78, 2128 (1974).

[97] I. T. Steinberger, in *Classical Rare Gas Liquids*, edited by W. F. Schmidt and E. Illenberger (Am. Sci. Publ., 2005), and references therein.

[98] K. N. Altmann, R. Reininger, "Density dependence of the conduction-band minimum in fluid krypton and xenon from field ionization of $(CH_3)_2S$," J. Chem. Phys. 107, 1759 (1997).

[99] J. Meyer, R. Reininger, "Electric-field ionization of high Rydberg states and vertical ionization potential of an impurity in dense fluid argon," Phys. Rev. A 47, R3491 (1993).

[100] T. R. Strobridge, "The thermodynamic properties of nitrogen from 64 to 300 K between 0.1 and 200 atmospheres," Tech. Note 129, Nat. Bur. Std. (U.S.) (1962).

[101] A. L. Gosman, R. D. McCarty, J. G. Hust, "Thermodynamic properties of argon from the triple point to 300 °K at pressures to 1000 atmospheres," Tech. Note 27, Nat. Bur. Std. (U.S.) (1969).

[102] W. B. Streett, L. A. K. Staveley, "Experimental study of the equation of state of liquid krypton," J. Chem. Phys. 55, 2495 (1971).

[103] W. B. Streett, L. S. Sagan, L. A. K. Staveley, "Experimental study of the equation of state of liquid xenon," J. Chem. Thermodyn. 5, 633 (1973).

[104] B. A. Younglove, J. F. Ely, "Thermophysical properties of fluids. II. Methane, ethane, propane, isobutane, and normal butane," J. Phys. Chem. Ref. Data 16, 577 (1987).

[105] R. Schmidt, W. Wagner, "A new form of the equation of state for pure substances and its application to oxygen," Fluid Phase Equil. 19, 175 (1985).

[106] D. G. Friend, H. Ingham, J. F. Ely, "Thermophysical properties of ethane," J. Phys. Chem. Ref. Data 20, 275 (1991).

[107] E. W. Grundke, D. Henderson, R. D. Murphy, "Evaluation of the Percus-Yevick theory for mixtures of simple liquids," Can. J. Phys. 51, 1216 (1973).

[108] J. O. Hirschfelder, C. F. Curtiss, R. B. Bird, *Molecular Theory of Gases and Liquids* (Wiley, New York, 1954).

[109] J. J. Potoff, A. Z. Panagiotopoulos, "Critical point and phase behavior of the pure fluid and a Lennard-Jones mixture," J. Chem. Phys. 109, 10914 (1998).

[110] P. T. Sikora, "Combining rules for spherically symmetric intermolecular potentials," J. Phys. B: At. Mol. Opt. Phys. 3, 1475 (1970).

[111] H. S. W. Massey, E. H. S. Burhop, *Electronic and Ionic Impact Phenomena Vol. 1* (Clarendon Press, Oxford, 1969).

[112] P. Attard, "Spherically inhomogeneous fluids. I. Percus-Yevick hard spheres: osmotic coefficients and triplet correlations," J. Chem. Phys. 91, 3072 (1989).

[113] P. Attard, "Spherically inhomogeneous fluids. II. Hard-sphere solute in a hard-sphere solvent," J. Chem. Phys. 91, 3083 (1989).

[114] M. J. Gillan, "A new method of solving the liquid structure integral equations," Molec. Phys. 38, 1781 (1979).

[115] S. Labík, A. Malijevský, P. Voňka, "A rapidly convergent method of solving the OZ equation," Molec. Phys. 56, 709 (1985).

[116] A. A. Broyles, "Radial distribution functions from the Born-Green integral equation," J. Chem. Phys. 33, 456 (1960).

[117] R. J. Baxter, "Ornstein-Zernike relation for a disordered fluid," Aust. J. Phys. 21, 563 (1968).

[118] R. J. Baxter, "Ornstein-Zernike relation and Percus-Yevick approximation for fluid mixtures," J. Chem. Phys. 52, 4559 (1970).

[119] K-C. Ng, "Hypernetted chain solutions for the classical one-component plasma up to $\Gamma = 7000$," J. Chem. Phys. 61, 2680 (1974).

[120] G. C. Maitland, M. Rigby, E. B. Smith, W. A. Wakeham, *Intermolecular Forces* (Clarendon Press, Oxford, 1981, 1987).

[121] X. -R. Chen, Y. -L. Bai, J. Zhu, X. -D. Yang, "Intermolecular interaction potentials of the methane dimer from the local density approximation," Phys. Rev. A 69, 034701 (2004).

[122] S. D. Hamann, J. A. Lambert, "The behaviour of fluids of quasi-spherical molecules," Aust. J. Chem. 7, 1 (1954).

[123] M. A. Clarke, P. R. Bishnoi, "Development of an implicit least squares optimisation scheme for the determination of Kihara potential parameters using gas hydrate equilibrium data," Fluid Phase Equilib. 211, 51 (2003).

[124] A. G. De Rocco, J. O. Halford, "Intermolecular potentials of argon, methane and ethane," J. Chem. Phys. 28, 1152 (1958).

[125] D. G. Friend, J. F. Ely, H. Ingham, "Thermophysical properties of methane," J. Phys. Chem. Ref. Data 18, 583 (1989).

[126] Y. Tang, Z. Tong, B. C. -Y. Lu, "Analytical equation of state based on the Ornstein-Zernike equation," Fluid Phase Equilib. 134, 21 (1997).

[127] D. McQuarrie, *Statistical Mechanics* (Harper & Row, New York, 1976).

[128] T. E. Morsy, "Extended Benedict-Webb-Rubin equation of state. Application to eight fluorine compounds," J. Chem. Eng. Data 15, 256 (1970).

[129] H. Orbey, S. I. Sandler, "Equation of state modeling of refrigerant mixtures," Ind. Eng. Chem. Res. 34, 2520 (1995).

[130] Luxi Li, *Atomic and Molecular Low-n Rydberg States in Supercritical Fluids*, Ph.D. dissertation, The Graduate Center of the City University of New York, New York, NY, 2009.